

## BRIGHTEST CLUSTER GALAXIES AT THE PRESENT EPOCH

TOD R. LAUER

National Optical Astronomy Observatory,\* P.O. Box 26732, Tucson, AZ 85726

MARC POSTMAN

Space Telescope Science Institute, † 3700 San Martin Drive, Baltimore, MD 21218

MICHAEL A. STRAUSS, GENEVIEVE J. GRAVES, AND NORA E. CHISARI

Department of Astrophysical Sciences, Princeton University, Princeton, NJ

*Accepted for Publication in The Astrophysical Journal*

### ABSTRACT

We have obtained photometry and spectroscopy of 433  $z \leq 0.08$  brightest cluster galaxies (BCGs) in a full-sky survey of Abell clusters to construct a BCG sample suitable for probing deviations from the local Hubble flow. The BCG Hubble diagram over  $0 < z < 0.08$  is consistent to within 2% of the Hubble relation specified by a  $\Omega_m = 0.3$ ,  $\Lambda = 0.7$  cosmology. This sample allows us to explore the structural and photometric properties of BCGs at the present epoch, their location in their hosting galaxy clusters, and the effects of the cluster environment on their structure and evolution. We revisit the  $L_m - \alpha$  relation for BCGs, which uses  $\alpha$ , the log-slope of the BCG photometric curve of growth, to predict the metric luminosity in an aperture with 14.3 kpc radius,  $L_m$ , for use as a distance indicator. Residuals in the relation are 0.27 mag rms. We measure central stellar velocity dispersions,  $\sigma$ , of the BCGs, finding the Faber-Jackson relation to flatten as the metric aperture grows to include an increasing fraction of the total BCG luminosity. A 3-parameter “metric plane” relation using  $\alpha$  and  $\sigma$  together gives the best prediction of  $L_m$ , with 0.21 mag residuals. The distribution of projected spatial offsets,  $r_x$  of BCGs from the X-ray-defined cluster center is a steep  $\gamma = -2.33$  power-law over  $1 < r_x < 10^3$  kpc. The median offset is  $\sim 10$  kpc, but  $\sim 15\%$  of the BCGs have  $r_x > 100$  kpc. The absolute cluster-dispersion normalized BCG peculiar velocity  $|\Delta V_1|/\sigma_c$  follows an exponential distribution with scale length  $0.39 \pm 0.03$ . Both  $L_m$  and  $\alpha$  increase with  $\sigma_c$ . The  $\alpha$  parameter is further moderated by both the spatial and velocity offset from the cluster center, with larger  $\alpha$  correlated with the proximity of the BCG to the cluster mean velocity or potential center. At the same time, position in the cluster has little effect on  $L_m$ . Likewise, residuals from the metric plane show no correlation with either the spatial or velocity offset from the cluster center. The luminosity difference between the BCG and second-ranked galaxy, M2, increases as the peculiar velocity of the BCG within the cluster decreases. Further, when M2 is a close luminosity “rival” of the BCG, the galaxy that is closest to either the velocity or X-ray center of the cluster is most likely to have the larger  $\alpha$ . We conclude that the inner portions of the BCGs are formed outside the cluster, but interactions in the heart of the galaxy cluster grow and extend the envelopes of the BCGs.

*Keywords:* galaxies: clusters: general — galaxies: distances and redshifts — galaxies: elliptical and lenticular, cD — galaxies: fundamental parameters — galaxies: photometry

### 1. THE MOST MASSIVE GALAXIES IN THE UNIVERSE

The brightest and most massive galaxies in the present-day Universe are the first-ranked or brightest cluster galaxies (BCG) in rich galaxy clusters. The first studies of BCGs focussed on their high and almost “standard-candle” luminosities, which allowed the Hubble-flow to be characterized out to large distances (Sandage 1972a,b; Gunn & Oke 1975). The dispersion about the mean luminosity was shown to be significantly smaller than would be the case had the BCGs simply been the brightest galaxies drawn from a standard luminosity function

(Tremaine & Richstone 1977; Loh & Strauss 2006). The narrowness of the BCG luminosity distribution does not extend to less massive galaxy groups (Geller & Postman 1983), however; and more recent work argues that only the more luminous BCGs may be special (Lin et al. 2010). These results highlight the need to understand at what mass scale the unique formation and evolution mechanisms that shape BCGs come into play.

The acronym “BCG” underscores that these galaxies are tied to the galaxy clusters that host them. If BCGs are indeed special it is likely to be because their formation and evolution is tied to physical mechanisms unique to rich galaxy clusters. Cannibalism, whereby a BCG sitting in the middle of the cluster potential tends to engulf and merge with its neighbors, has been invoked to explain the high luminosity of these systems (e.g., Ostriker & Tremaine 1975; Hausman & Ostriker 1978, but see also Richstone 1975), but it remains unclear why this leads to

\*The National Optical Astronomy Observatory is operated by AURA, Inc., under cooperative agreement with the National Science Foundation.

†Operated by the Association of Universities for Research in Astronomy, Inc., for the National Aeronautics and Space Administration.

such uniform properties, especially when we know that many clusters undergo interactions and merging. BCG growth by cannibalism does appear to take place in clusters at some level (Lauer 1988), however, dynamical arguments suggest that most of the BCG assembly takes place outside the cluster (Merritt 1985).

The properties of BCGs are distinct from those of the other galaxies in clusters, and any model for their formation has to acknowledge this. BCGs generally sit close to the X-ray centers of their hosting clusters and usually have small “peculiar” velocities relative to the cluster mean. Sastry (1968), Binggeli (1982), Lambas et al. (1988), and others showed that BCGs tend to be aligned with their parent cluster. This has been explored in detail with data from the SDSS by Niederste-Ostholt et al. (2010) and Hao et al. (2011), who found that this alignment is marked only in clusters in which the BCG is *dominant*, i.e., more than 0.65 mag brighter than the average of the second and third-ranked galaxies. Those clusters in which the BCG is not strongly dominant may be systems that recently underwent a merger, and are therefore not completely relaxed. In short, in many ways the BCG reflects the environment of the cluster that hosts it.

Our approach to understanding the origin of BCGs is to conduct an extensive examination of their present-day structure, luminosity, and cluster environments. We organize our thinking around three broad questions:

### 1.1. *What Are the Present-Day Properties of BCGs?*

The dispersion in the luminosities of the BCGs about the mean Hubble relation, measured by the first studies to use BCGs as distance indicators, was typically 0.3 to 0.4 magnitudes (Sandage 1972a,b; Gunn & Oke 1975). An important refinement of the use of BCG as distance indicators was developed by Hoessel (1980), who showed that BCG metric luminosity,  $L_m$ , was correlated with the logarithmic slope,  $\alpha$ , of the photometric curve-of-growth. The  $L_m - \alpha$  relation is a form of a luminosity-radius relation that side-steps the difficulties of characterizing the extended envelopes of BCG at large radii and faint isophotal levels. Postman & Lauer (1995, hereafter PL95) reinvestigated the use of BCG as distance indicators, using the  $L_m - \alpha$  relation for a full-sky characterization of the linearity of the local Hubble-flow (Lauer & Postman 1992) and providing a distant reference-frame to measure the relative peculiar velocity of the Local Group (Lauer & Postman 1994). Residuals about the PL95  $L_m - \alpha$  relation were only 0.25 mag (rms).

This paper presents a large full-sky sample of BCGs in Abell clusters over the redshift range  $0 < z \leq 0.08$ . The original goal for obtaining this sample was to extend the bulk-flow analysis of Lauer & Postman (1994) to greater distances. That work implied that the Abell clusters within  $z \leq 0.05$  participated in a coherent motion in excess of  $689 \pm 178 \text{ km s}^{-1}$  superimposed on the background cosmological expansion or “Hubble flow” within the volume containing the sample. This analysis will be presented in a separate work. Requirements for measuring accurate bulk flows, however, specify much of the sample definition, observational methodologies, and analysis of the BCG properties undertaken in this work. A full sky sample allows for the optimal determination of any large-scale bulk mass flow. The relatively low redshift-limit of the sample and its overall size is dictated by the

scale out to which the BCGs can be used as accurate distance indicators. The observational methodology is driven by the need to obtain highly uniform photometry over the angular and spatial extent of the sample. Much of the analysis is a reinvestigation of the use of BCGs as distance indicators, with a substantially larger sample and new observations that go well beyond the material available to PL95.

Regardless of the bulk-flow analysis, the present sample offers an excellent opportunity to assess the structural properties of BCG to understand their origin, evolution over time, and their particular uniqueness as the luminous endpoint of galaxy formation, problems that were not addressed by the smaller sample and less-complete cluster information available to Postman & Lauer (1995). Oegerle & Hoessel (1991) and Lauer et al. (2007), for example, found that the central stellar velocity dispersions,  $\sigma$ , of BCGs increase very slowly if at all with the *total* BCG luminosity (also see Bernardi et al. 2007; von der Linden et al. 2007; Liu et al. 2008). Typical BCG  $\sigma$  values are modest for their large luminosities, which may reflect the origin of BCGs in “dry” mergers (Boylan-Kolchin et al. 2006). In contrast, BCGs are unusually extended as compared to giant ellipticals, as is seen in the relation between effective radius,  $R_e$ , and total luminosity of the BCGs (Lauer et al. 2007; Bernardi et al. 2007). We will use the structure of BCGs as a probe of the effects of cluster environment on their evolution. In a companion paper (Chisari et al. 2014) we will compare the structure of BCGs to those of other highly luminous elliptical galaxies. The mutual relations between  $L$ ,  $\sigma$ , and  $R_e$  for elliptical galaxies overall are understood as various projections of the “fundamental plane” (Dressler et al. 1987; Djorgovski & Davis 1987). Understanding the relationship of BCGs to the fundamental plane will be explored in Chisari et al. (2014).

### 1.2. *Where Are the BCGs Located in Their Galaxy Clusters?*

The “textbook” picture of a galaxy cluster is that it is a swarm of galaxies anchored by a massive cD residing at rest in the exact center of the potential as marked by hot, X-ray emitting, gas. Early work on the X-ray morphology of galaxy clusters (Jones & Forman 1984) and their velocity structure (Quintana & Lawrie 1982) indeed show that the BCG is likely to be centrally located. There are certainly examples of such clusters in our sample. At the same time, there are also massive galaxy clusters, like Coma (Abell 1656), in which neither the BCG, nor second-ranked galaxy, M2, are at the center of the potential. Coma may be the recent merger of two clusters, and this is the point — the position of the BCG with respect to the center of the potential, X-ray emission, may testify to the evolutionary state of both the BCG and the cluster. More recent work (Patel et al. 2006; Hashimoto et al. 2014) shows that the BCG is often displaced from the center of the cluster potential as defined by the X-ray emission. For the present sample of clusters we have quantified the distribution of projected spatial-offsets of the BCGs, finding that it is a steep power-law over three decades in radius.

For the BCG to reside at the spatial center of the cluster, it must also be at rest there. It has long been known that there are BCGs with “significant” peculiar veloci-

ties within the cluster (Zabludoff et al. 1990; Malumuth 1992; Zabludoff et al. 1993; Oegerle & Hill 2001). PL95 described the overall distribution of BCG peculiar velocities within their sample as a Gaussian with dispersion,  $\sigma_1 = 264 \text{ km s}^{-1}$ , comparing this to the substantially larger mean cluster velocity-dispersion  $\sigma_c = 666 \text{ km s}^{-1}$ . We attempted to verify this result with our much larger present sample, finding now that the distribution of peculiar velocities is exponential, extending out to galaxies with  $\Delta V_1 > \sigma_c$ .

Both the distributions of the spatial and velocity offsets of the BCGs are particularly interesting when compared to the Martel et al. (2014) simulations of galaxy cluster formation and evolution. These simulations emphasize that the location of the BCG within a cluster bears witness to its history of formation from smaller accreted groups and clusters. The dark matter, galaxy, and X-ray-emitting gas distributions in any cluster all have different timescales and physical mechanisms for responding to the accretion or interaction with another cluster. The locations of the BCGs reflect this. Skibba et al. (2011) studied the peculiar velocities and spatial positions of a large sample of clusters and groups, showing that the location of the brightest galaxy in the systems provides a sharp test of the mechanisms that formed them.

### 1.3. How Does the Cluster Environment Relate to the Properties of the BCGs?

The relationship of the structure and luminosity of the BCG to the properties of the cluster has proven to be a multi-faceted problem. Initial work showed the BCG luminosity to be only weakly related to the richness of the clusters (Sandage 1972b; Sandage & Hardy 1973; Sandage 1975, 1976). We re-investigated this relation in PL95, and saw no relation between the metric luminosity and cluster richness.

BCG luminosity and structure, however, do appear to be related to the X-ray properties of the clusters. Schombert (1988) found that the envelope luminosity of cD galaxies, a subset of the BCGs, increases with total cluster X-ray luminosity. Edge (1991) and Edge & Stewart (1991) found a strong relationship between BCG luminosity and cluster X-ray temperature, which itself is closely related to the cluster velocity dispersion (Solinger & Tucker 1972). Hudson & Ebeling (1997) and Collins & Mann (1998) also found that BCG luminosity increases with cluster X-ray luminosity. Lastly, Brough et al. (2005) found the structure of the BCG to also correlate with cluster X-ray luminosity, with the BCG envelope becoming more extended in more luminous clusters.

In this paper we show that both the BCG luminosity, and the radial extent (as characterized by  $\alpha$ ) of their envelopes (where by “envelope” we mean simply the outer portions of the galaxies) correlate with cluster velocity dispersion. We take this a step further, however, finding that the extent of the envelope is related to both the spatial and velocity positions of the BCG *within* its hosting cluster. The luminosity and structural difference between the BCG and the second ranked galaxy, M2, also appears to depend on which galaxy has the smaller peculiar velocity within the cluster or the smaller offset from the center of the cluster potential as marked by X-ray emission. Beers & Geller (1983) found that early type galaxies with extended halos (e.g., D or cD galaxies)

lie on significant peaks in the cluster galaxy distribution regardless of whether they are the BCG. We now see how the structure of the BCG itself changes smoothly as a function of how close to the center of the cluster it resides.

### 1.4. This Paper

We begin in §2 with the geometric and redshift selection of the Abell clusters defining the present sample, detailing the imaging observations used both to select the BCG for any given cluster and to provide accurate surface photometry. Spectroscopic observations are presented, which provide BCG redshifts and central stellar velocity dispersions. A crucial part of the sample definition is the derivation of accurate mean redshifts and velocity dispersions for the galaxy clusters. The projected spatial and velocity locations of the BCGs within their clusters is presented in §3. The photometric and kinematic properties of the BCGs are presented in §4, with particular attention to parametric relations between the metric luminosity and BCG structure. This section also explores the relationship between BCG properties and cluster environment. Additional information about the BCGs is provided by the properties of the second-ranked galaxies, M2, which are presented in §5. We summarize what we have learned about the origin and evolution of BCGs in the final section of the paper.

## 2. A FULL-SKY SAMPLE OF LOCAL BCGS

### 2.1. Definition of the Sample

The present sample of BCGs comprises 433 Abell (1958) and ACO (Abell et al. 1989) galaxy clusters with mean heliocentric velocities,  $V < 24,000 \text{ km s}^{-1}$  and galactic latitude,  $|b| \geq 15^\circ$ . There is no limit on the minimum richness class of the clusters. Table 1 lists the BCG coordinates, and heliocentric velocities,  $V_1$ , as well as the cluster velocities,  $V_c$ , cluster velocity dispersions,  $\sigma_c$ , the number of galaxy velocities used to compute these,  $N_g$ , and the Schlegel et al. (1998)  $A_B$  values. The distribution on the sky in galactic coordinates is shown in Figure 1. We use a cosmological model with  $H_0 = 70 \text{ km s}^{-1} \text{ Mpc}^{-1}$ ,  $\Omega_m = 0.3$ , and  $\Lambda = 0.7$  throughout this paper.

The sample was originally designed to serve as a reference frame to measure the peculiar velocity of the Milky Way. The inferred luminosities of the BCGs serve as distance indicators, following the methodology presented in Lauer & Postman (1994, hereafter LP94). In that paper a volume-limited frame was constructed from 119 clusters with  $V < 15,000 \text{ km s}^{-1}$ , again using a  $\pm 15^\circ$  galactic “zone-of-avoidance.” The present sample largely includes the LP94 set (as will be qualified further below). For convenience, we will refer to the LP94 set of clusters as the 15K sample, while its present augmentation is the 24K sample. The 24K outer limit of the survey was selected to provide a significantly deeper reference frame than that constructed in LP94, but one that would not be too strongly affected by the limited depth of the Abell and ACO catalogues, which are heavily incomplete beyond  $z \sim 0.1$  (Postman et al. 1992).

The present sample is drawn from a considerably larger provisional sample defined by us in the early 1990’s based on a literature survey of Abell clusters with measured or

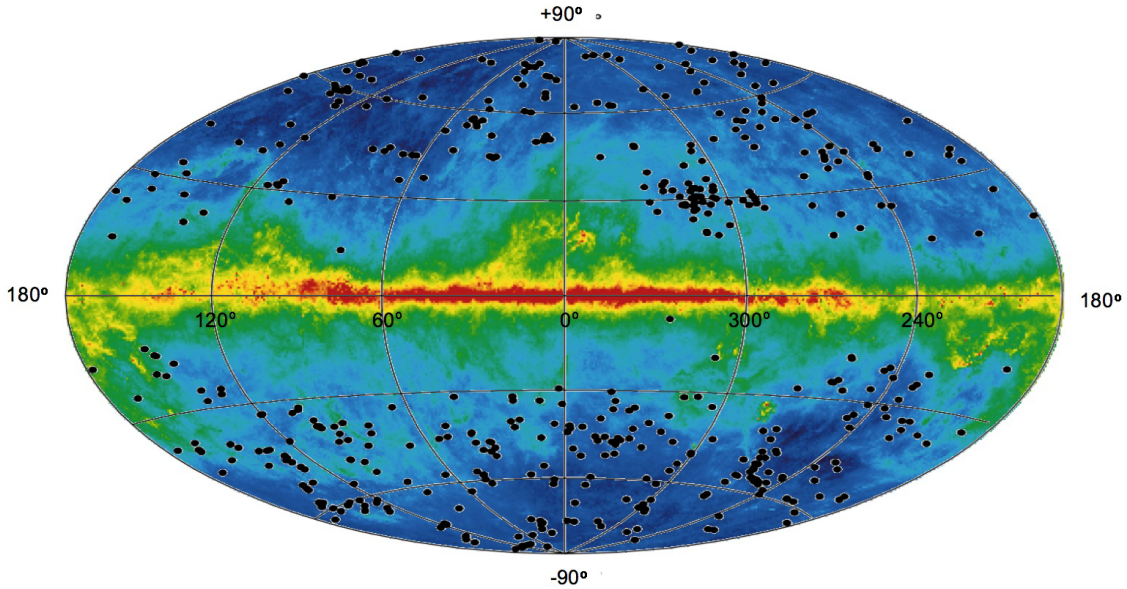


**Figure 1.** The distribution of the present sample of BCGs is shown in galactic coordinates superimposed over a predicted 94 GHz dust map derived from IRAS and COBE. The dense concentration of clusters at  $l \sim 315^\circ$ ,  $b \sim +30^\circ$  is due to the combination of the Hydra-Centaurus and Shapley superclusters. The dust map is a publicly available data product derived using the `predict_thermal` algorithm by Finkbeiner et al. (1999) and shows the predicted dust emission, in mK antenna temperature units at 94 GHz, using their 2-component model 8.

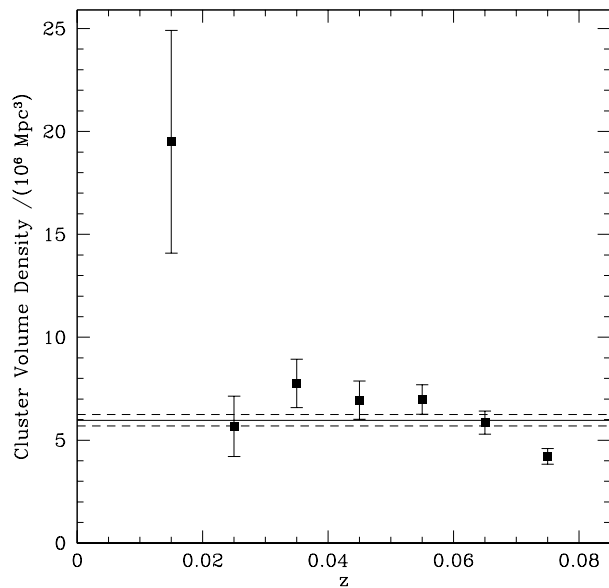


**Figure 2.** The comoving volume density of the clusters in this study, binned in  $\Delta z = 0.01$  shells as a function of redshift is shown. The error bars reflect the Poisson errors in the number of clusters in each shell. The horizontal lines give the density (and associated error) of BCGs averaged over the entire volume, but including 53 additional clusters lacking observations or that were excluded for having non-elliptical BCGs. The volume calculation accounts for the  $\pm 15^\circ$  galactic-plane “zone of avoidance” and the counts in each bin are corrected for the Abell cluster galactic latitude selection function  $P(|b|) = \text{dex}(0.3[1 - \csc|b|])$ .

estimated redshifts. Because we wanted to construct the best sampling of the local volume possible within the limitations of the Abell and ACO catalogues, we were liberal with accepting plausible candidates for the 24K sample. As we describe below, the final cluster selection is made with a combination of the latest published

redshift surveys and radial velocities that we measured ourselves.

The final set of 433 clusters are those of the larger candidate set for which we observed the BCG, and had sufficient redshift information to determine that the cluster was within the 24K redshift limit. There are 38 additional clusters that had well-determined redshifts that placed them within the 24K volume, but for which we were unable to image the BCG or sufficient candidates to be confident of the BCG selection. There are 15 more clusters with non-elliptical BCGs, which were also excluded from the sample. These clusters are listed in Table 2. These two sets include 5 clusters observed as part of the 15K sample, but that are now deleted from the present sample for a variety of reasons. With the present richer data set we now find that for two of the 15K clusters we in fact observed a small foreground group in front of a rich cluster, selected the M2 rather than the correct BCG in one cluster, and that the BCG is non-elliptical in the remaining two clusters.

The cluster space density as a function of redshift is shown in Figure 2. The cluster counts in each bin have been weighted by the established Abell cluster galactic latitude selection function:  $P(|b|) = \text{dex}(0.3[1 - \csc|b|])$  (Bahcall & Soneira 1983). The volume computation accounts for the  $\pm 15^\circ$  galactic-plane zone-of-avoidance. The average cluster comoving space density over the range  $z \leq 0.08$  is  $(5.97 \pm 0.28) \times 10^{-6} \text{ Mpc}^{-3}$ , including the 53 missed and non-elliptical BCG clusters. The space density of Abell clusters used in this study is relatively constant, with the exception of the last bin where a significant decline is seen. The positive deviation in the first bin, centered at  $z = 0.015$ , is not statistically significant ( $\sim 2.5\sigma$ ).

The completeness of the Abell catalog as a function of richness, redshift, and galactic latitude has been extensively studied. The trends are such that the com-

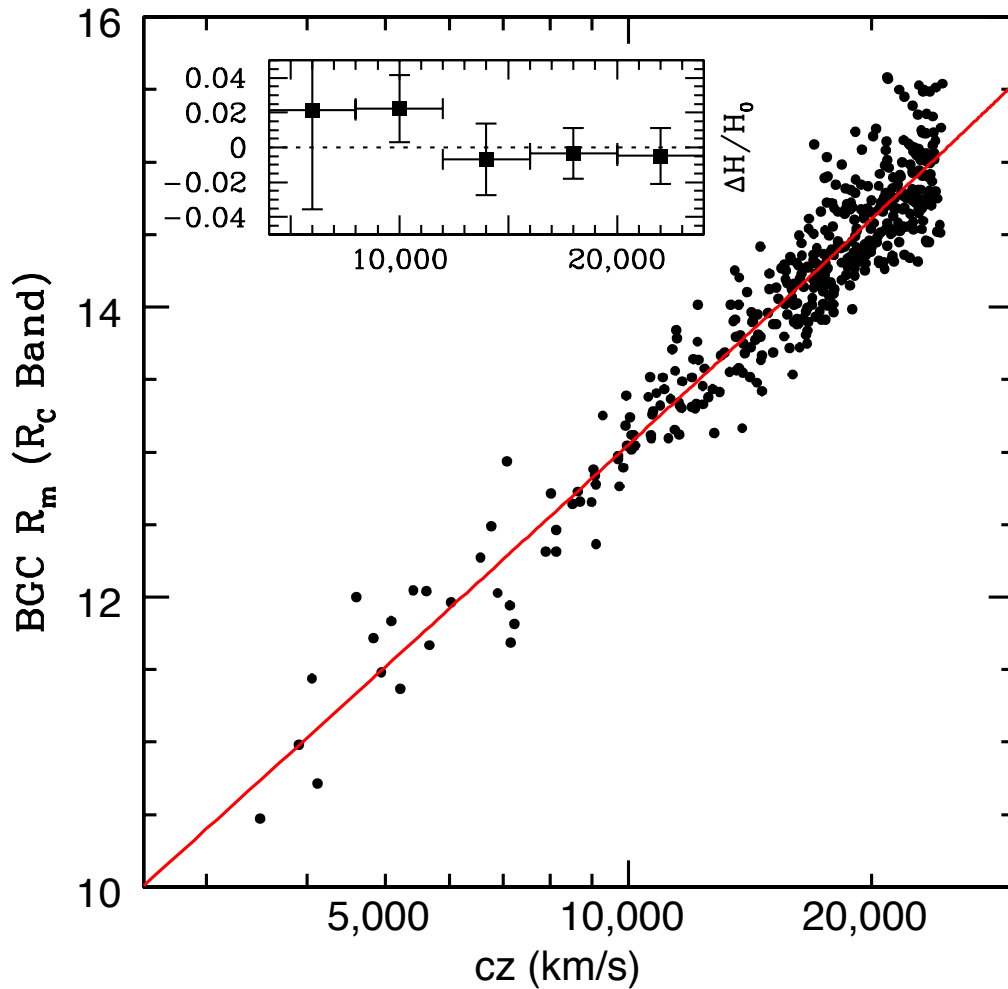


**Figure 3.** The Hubble diagram derived from the present 24K sample, showing BCG apparent metric luminosity as a function of cluster redshift (CMB frame). The red line is the mean theoretical Hubble relationship assuming  $\Omega_m = 0.3$ , and  $\Lambda = 0.7$ . The inset shows the binned residuals about relation in shells of  $4000 \text{ km s}^{-1}$  starting at  $4000 \text{ km s}^{-1}$ , expressed as  $\Delta H/H_0$ . The largest deviation in a shell is  $\Delta H/H_0 = -0.022$ , but none is significantly different from zero.

pleteness is lower at lower richness, higher redshift, and lower galactic latitude. More specifically, Postman et al. (2002) show that the detection efficiency as a function of richness class in the Abell catalog is  $\sim 55\%$  for  $RC = 0$ ,  $\sim 75\%$  for  $RC = 1$  and is essentially  $100\%$  for  $RC \geq 2$ . The richness class distribution in the current 24K sample is  $55\%$   $RC=0$ ,  $35\%$   $RC=1$ , and  $10\%$   $RC \geq 2$ . Our study here is immune to the known completeness trends so long as the properties of the BCG in the detected Abell clusters are representative of those in the clusters that were missed during the construction of the northern and southern Abell catalogs.

### 2.1.1. A BCG Hubble Diagram

As a further illustration of the sample geometry and its utility as a probe of the Hubble flow within the local volume, we show a Hubble diagram derived from our BCG sample in Figure 3. The details of the sample selection, reduction, and analysis of the photometry needed to generate this figure are the subject of much of the

rest of this paper. For now, the relevant details are that the velocities are mean cluster velocities in the cosmic microwave background (CMB) frame, and the photometry is the *apparent* metric luminosity,  $R_m$ , of the BCGs, but with extinction and k-corrections applied. The photometry has also been corrected to  $\alpha = 0.5$  using the relationship (equation 8) between metric luminosity and  $\log \alpha$ , a parameter measuring the slope of the photometric curve-of-growth at the metric radius,  $r_m$ .

The Hubble diagram shows that the number of galaxies per velocity interval, rises with distance as  $\sim D^2$ , as expected for a survey with a roughly constant cluster density with redshift. The sharp cut-off at the 24K velocity limit is also evident. The rms scatter about the nominal theoretical relation specified by  $\Omega_m = 0.3$ , and  $\Lambda = 0.7$  is  $0.271 \text{ mag}$ . We can constrain any departures from the expected Hubble flow as a function of redshift by binning the residuals about the Hubble relation. Since our sample is full sky, this effectively tests for monopole variations in the Hubble flow with

distance. Figure 3 shows the mean residuals in shells of  $4000 \text{ km s}^{-1}$  starting at  $4000 \text{ km s}^{-1}$ , expressed as  $\Delta H/H_0$ . All but the innermost shell are consistent with  $\Delta H/H_0 = 0$  at the  $< 2.0\%$  level; the innermost shell is also consistent with  $\Delta H/H_0 = 0$ , but with a poorer  $5.7\%$  error due to the small number of BCGs interior to  $8000 \text{ km s}^{-1}$ . The present result is completely consistent with the BCG Hubble diagram derived from the earlier 15K sample (Lauer & Postman 1992), but with errors nearly a factor of two smaller.

## 2.2. Selection of the BCGs

We define the BCG to be the brightest member (in the  $R_C$ -band) of the cluster within a  $14.3 \text{ kpc}$  radius<sup>1</sup> “metric aperture” centered on the galaxy (and with close or embedded companions photometrically subtracted), with the proviso that the galaxy must also be an elliptical. The use of metric BCG luminosity as a distance indicator was initially advanced by Gunn & Oke (1975), and developed further by Hoessel (1980) and PL95. As demonstrated in PL95, our particular choice of the metric aperture minimizes the scatter in the average BCG luminosity. The aperture is large enough to include a large fraction of the total luminosity of the BCG, but avoids the difficulty of measuring a total magnitude for the BCG, which requires surface photometry at very faint levels and large angular radii in a rich-cluster environment. This problem has limited the accuracy of a number of recent studies of BCGs. The photometry provided by the SDSS and 2MASS surveys, for example, strongly underestimates the total luminosity of low- $z$  BCGs (Lauer et al. 2007). The SDSS photometry suffers from over-subtraction of the sky background, while the 2MASS total magnitudes are based on a profile model that fails to include the extensive envelopes of the galaxies.

As with the definition of the cluster sample, we were liberal with observing all plausible BCG candidates for any given cluster, making the final choice only when all the observations were in hand. The initial selection of BCG candidates was done visually from digitized sky-survey plates, augmented with velocity information when available. Unless one galaxy was strongly dominant and known to be in the cluster from its redshift, we would typically select several bright elliptical galaxies for imaging and spectroscopic observations, with the final selection based on CCD aperture photometry and knowledge of the cluster redshift.

As noted in PL95, the BCGs in the 15K sample were often displaced in angle and/or velocity from the nominal cluster center, thus we attempted to select all bright elliptical galaxies within the nominal Abell radius of the cluster, rather than the brightest “central” galaxy. The Abell radius is  $1.5h^{-1} \text{ Mpc}$  or  $2.1 \text{ Mpc}$  for the present cosmological parameters.<sup>2</sup> One of the questions that will be considered in the later sections is the extent to which the BCG is in fact displaced from the cluster spatial and velocity centroids — allowing for the possibility that the

BCG may be significantly offset from either is critical to the BCG selection.

The selection of the BCG can be complex, and different surveys may disagree on which galaxy is the BCG in any given cluster. As one example, we compared our selection to those from von der Linden et al. (2007), who extracted their sample from the SDSS-based C4 cluster catalogue (Miller et al. 2005), using isophotal magnitudes for BCG luminosity. Of the 429 C4 clusters selected by von der Linden et al. (2007) that should be within our redshift limit, only 44 clusters are in our sample.<sup>3</sup> Of the 44 cluster matches, we agreed on the BCG in 33 or 75% of the clusters. In 8 of the 11 clusters remaining von der Linden et al. (2007) selected a galaxy that we classified as M2, the second-ranked galaxy, based on our photometry. As noted in the next section, this choice may depend on the size of the metric aperture, but we concluded that our M2 would be the BCG based on total flux (see below) in only 3 of the 8 cases. Lastly, for one cluster, A1142, the C4 catalogue identified two clusters, with the BCG for one corresponding to our M2 for A1142.

### 2.2.1. A Subset of Bright M2 Members

As a natural consequence of imaging all plausible BCG candidates, we also imaged a large sample of second-ranked cluster members, M2, as based on their metric luminosities. This set is presented in Table 3. We observed 179 M2 galaxies, corresponding to  $\sim 41\%$  coverage over the total sample of 433 clusters. Of course, we were most likely to observe M2 when it was a close rival to the BCG. We thus have constructed a sample of M2s that are likely to have properties similar to the BCGs. Indeed, many of the M2 galaxies in clusters with more luminous BCGs in fact are more luminous than a significant fraction of the BCGs in other clusters. The M2 sample appears to be nearly complete for galaxies within  $0.3 \text{ mag}$  of the BCG luminosity in any cluster. Because we were not complete in observing M2s that were not close rivals of the BCG, however, this sample must be used carefully.

We emphasize that because the BCG/M2 selection is based on the metric, rather than total luminosity, there are 14 M2s (identified in Table 3) that would have been selected as the BCG had a larger aperture been used. These galaxies have  $\alpha$  substantially larger than that of their corresponding BCG, such that the integrated flux out to a given radius ultimately exceeds that of the BCG when the radius is large enough. Because this ambiguity affects only a small portion of the sample, and the radial limits of the surface photometry are heterogeneous at radii well outside the metric aperture, we prefer to preserve the purely metric-aperture based BCG selection.<sup>4</sup>

## 2.3. Imaging Observations and Photometry

### 2.3.1. Observations

<sup>3</sup> There were 8 additional clusters that might have been in the common set. We were not able to obtain BCG photometry in 4 of them, and the BCGs in the remaining 4 were not elliptical galaxies.

<sup>4</sup> All of the M2s flagged as ultimately exceeding the BCG in luminosity do so at only very large radii. In one case, however, for the BCG/M2 pair in A3531, the transition occurred just outside the metric radius, so we designated the initial M2 galaxy as the true BCG.

<sup>1</sup> This is the same as the  $10 h^{-1} \text{ kpc}$  radius used in LP94 and PL95.

<sup>2</sup> This is somewhat larger than the over-density radius,  $r_{200}$ , (Carlberg et al. 1997) which has a median value of  $1.7 \text{ Mpc}$  for the present sample, and is often used as a proxy for the physical extent of a galaxy cluster.

Images of the BCGs were obtained in 13 runs between 1989 and 1995 using CCD cameras on the KPNO-4m, KPNO-2.1m, and CTIO-1.5m telescopes. The runs are listed in Table 4. The first set of runs from 1989 to 1991 were used for the observations of the 15K sample presented in PL95, but are repeated here for convenience. As compared to the first set of runs, the cameras used in the later runs generally had larger fields, allowing for more straight forward estimation of the sky level, as well as improved efficiency for observing multiple BCG candidates in a single observation.

For the PL95 observations of the 15K sample, we obtained images in both the Kron-Cousins  $R_C$  and Johnson  $B$  filters. The  $R_C$ -band imagery served as the primary material used for the photometry, with the  $B$ -band providing auxiliary information to test the validity of the extinction and k-corrections, as well as to test the BCG  $B - R_C$  color as diagnostic of the properties of the galaxies. In PL95, however, we found that the BCGs had a very narrow range in color ( $\langle B - R_C \rangle = 1.51$ ;  $\sigma_{(B-R_C)} = 0.06$  mag) that showed no correlation with other properties of the BCGs or with residuals in their photometric distance estimates. We thus elected to only obtain  $R_C$ -band images for the present sample, given the demands of observing a large number of galaxies in the limits of the observing time available.<sup>5</sup>

To allow for the use of BCGs as photometric distance indicators, we could only obtain useful images under photometric conditions. About 20% of each night was dedicated to observing Landolt (1983) standard stars. Frequent observation of standards not only allowed the photometric quality of the night to be monitored, but also allowed for frequent characterization of the airmass-extinction term, which often varied from night to night, or even over the duration of a single night. Given the very narrow range of color seen in BCGs, we were less concerned with determining the color terms of the cameras, and selected standard stars that closely matched the typical  $B - R_C$  colors of the BCGs. The median scatter in the standard star photometry over all nights was only 0.008 mag, with the two poorest nights having residuals of 0.022 and 0.035 mags.

In addition to obtaining accurate photometric calibration, we also were concerned with accurate flat-field calibration of the images, such that accurate sky levels could be measured. This was done by observing a number of “blank sky” fields during the night to correct for large-scale illumination patterns that were not removed by the standard use of dome flat-field images. We could not use the alternative of generating a sky-flat from the stack of images obtained on any given night, since the BCGs are extended and were typically centered in the CCD fields. This procedure reduced the error in the sky levels from several percent to a few tenths of a percent. As we discuss below, the final total error in the metric magnitudes as measured by cross validation is only 0.01 mag, demonstrating that any errors associated with the sky subtraction must be less than those contributed by the photometric solution.

<sup>5</sup> 2MASS K-band photometry is too shallow to provide reliable measurements over the metric aperture. See Appendix B in Lauer et al. (2007) for full details.

### 2.3.2. Image Reduction and Surface Photometry

Reduction of the CCD images obtained in the newer set of runs followed the same procedures as were described in PL95. Sky levels were determined from the intensity modes measured in the corners of the images. Surface photometry of the BCG candidates was obtained using the least-squares isophote-fitting algorithm of Lauer (1986). In brief, the algorithm describes the galaxies as a nested set of concentric elliptical isophotes, which are allowed to have arbitrary surface brightness, ellipticity, and position angle as a function of radius. The key feature of the algorithm is that it allows galaxies in the images to overlap; indeed it was developed explicitly to decompose “multiple-nucleus” BCG into individual galaxies. In multiple systems, overlapping, merging, or even luminous galaxies completely embedded in the BCG are modeled and subtracted from the envelope of the BCG prior to measurement of the metric luminosity. Again, no assumed form of the surface brightness profile was imposed. The algorithm also allows bad pixels, bright stars, compact galaxies, dust patches, and so on, to be excluded from the surface photometry solution.

Once the surface photometry for all the galaxies in an image was completed, model images were reconstructed from the surface brightness profiles and their total flux integrated in a geometric series of circular apertures centered on the galaxy. This is the final form of the photometry used for the subsequent analysis. The actual value of the luminosity with the metric aperture is obtained by using cubic splines to interpolate among the series of apertures, based on the final velocity adopted for any given cluster. This representation is highly accurate; the  $1 - \sigma$  difference between the surface photometry integrated over the metric aperture versus integrating over the galaxy image directly (carefully cleaned of contaminating sources) is only 0.003 mag.

Lastly, the photometry is corrected for galactic extinction and the filter K-correction, as was done in PL95; for the  $R_C$ -band,  $K_R = \log_{10}(1 + 0.96z)$ , and  $A_R = 0.59A_B$ . Extinction values for the present work are provided by Schlegel et al. (1998), in contrast with PL95, where extinctions from Burstein & Heiles (1982) were used. Table 1 gives the  $A_B$  values used.

### 2.3.3. Cross Validation of the Photometry

To provide additional validation of the galaxy photometry, observations of several galaxies were repeated in multiple runs, as was also done in PL95. We also re-imaged most of the 15K BCGs in the course of obtaining the 24K sample. This not only allows the accuracy of any given aperture measurement to be confirmed, but also provides a test for any systematic differences in the photometric zeropoints between the various runs. Because we were concerned with obtaining consistent photometry over the full sky, care was taken to ensure that extensive cross-validation observations between the north/south hemispheres and spring/fall observing seasons were obtained. Figure 4 shows the measured differences in the metric magnitude for galaxies observed across different runs. The data allowed 48 separate inter-run comparisons to be performed, assembled from 260 overlap galaxy observations obtained over the course of the imaging part of the survey. This provided 62% of the 78 potentially

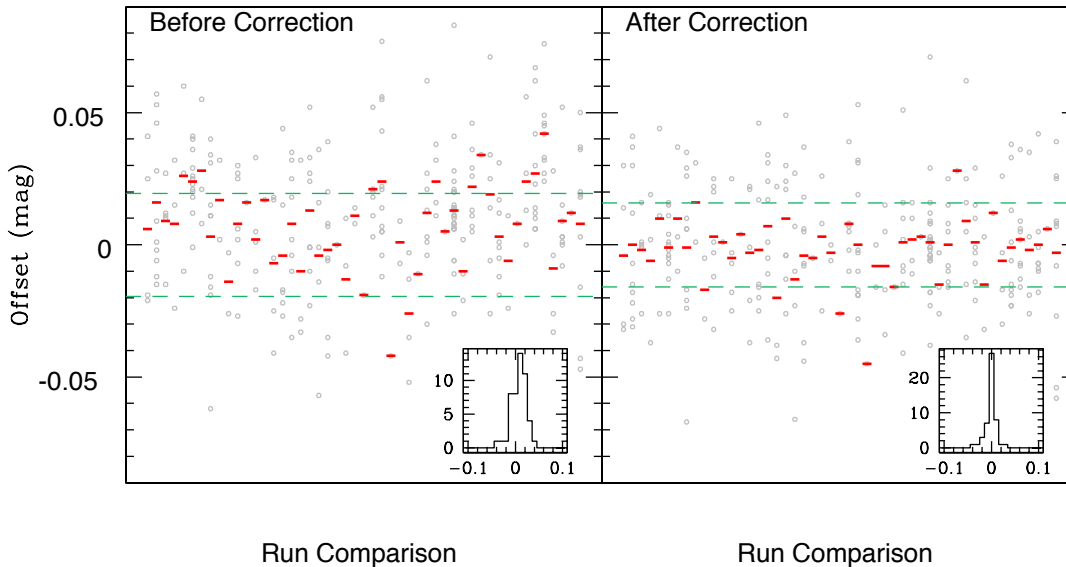


**Figure 4.** The differences between the single observations of the metric magnitude for galaxies observed in common between different observing runs. A total of 48 inter-run comparisons, derived from 260 overlap galaxy observations, are shown. The light grey data points show the individual differences. Red lines show the mean offset for each inter-run comparison. The dashed green lines show the total rms value. The plot on the left shows the results before the global offset corrections are applied to the photometry. The plot on the right shows the residual differences after the offset corrections are applied to each run. The distribution of the average metric magnitude offsets for all 48 inter-run comparisons is shown in the histograms in the lower right of each plot. As the analysis is based on *differences* between pairs of observations, the photometric error in any single observation will be  $\sqrt{2}$  smaller on average. After correction, the final *total* photometric error for any metric magnitude is 0.011 mag.

unique comparisons among the 13 runs, thus densely populating the run/run cross-correlation matrix.

The total rms for all *differences* between pairs of duplicate galaxy metric magnitudes is 0.0195 mag, which implies that the average error in any single measure is 0.0138 mag, a factor of  $\sqrt{2}$  smaller. By fitting for an average photometric offset correction for each run (done as a simultaneous least-squares fit to the entire ensemble of overlap observations), we can reduce the total difference rms to 0.0159 mag, or 0.0112 mag for any single observation. Because the average photometric correction for any single run is small, 0.0104 mag, we have chosen not to apply the corrections in the present work; however, systematic differences between runs are more important for the measurement of large scale deviations from the Hubble flow, and will be considered in our use of the present sample as a velocity reference frame.

#### 2.4. Spectroscopic Observations

We obtained long-slit spectra of all BCG candidates in the sample over the course of 14 observing runs, spanning a five year timeframe, at NOAO’s Cerro Tololo Inter-American Observatory (CTIO) and Kitt Peak National Observatory (KPNO). The CTIO observations were done primarily using the Blanco 4-m telescope, except for the first two runs, which used the 1.5-m telescope. All KPNO runs were done using the Goldcam spectrograph on the 2.1m telescope. Table 5 summarizes the instrumental parameters. The slit width was set to 2 arc-seconds. For most observations, two or three independent exposures were obtained (and coadded for further analysis), although in some cases only a single exposure was acquired. The exposure times for each individual exposure varied depending on telescope aperture and the es-

timated target redshift. As the overall objective was to use the spectra to obtain both a measurement of the redshift and the internal stellar velocity dispersion, we set integrations to achieve a minimum signal-to-noise ratio of 20 per pixel in the final co-added 1D spectrum. A total of 842 co-added spectra were obtained for 689 unique galaxies.

Over the course of the survey, we repeatedly observed 13 bright nearby galaxies as radial velocity reference standards. These observations were designed to provide a cross-check on our redshift measurement accuracy over the duration of the program. The mean absolute value of the velocity difference between the reference galaxy redshifts from different runs was  $32 \text{ km s}^{-1}$  ( $(\Delta v/v) = 0.005$ ) with an rms scatter of  $38 \text{ km s}^{-1}$ . We also observed a subset of BCGs multiple times, both from this survey and from the earlier LP94 survey to serve as cross-checks between different observing runs and telescopes. For the velocity dispersion estimates, a series of spectra were repeatedly obtained of 27 K-giant stars.

The 2D spectra were corrected for basic instrumental signatures. Bad columns were identified and interpolated over. Bias subtraction was done by first using the overscan region to determine the mean DC level, which was subtracted from the full frame. Bias structure removal was then performed using a series of zero-duration exposures acquired before the start of each night. Quartz lamp exposures were co-added and normalized to provide a flat-field correction frame. Any cosmic ray hits that extended for more than 2 pixels were manually identified and interpolated over where possible. Smaller cosmic ray hits were dealt with during co-addition of the extracted 1D spectra.

The 1D spectra were extracted and wavelength-



calibrated using IRAF’s NOAO `onedspec` package. The extraction was done using a 3rd order Legendre polynomial function to allow the aperture center to track any significant spectral curvature along the dispersion axis. The average spectrum extraction aperture width was 9 arcseconds (rms 2.5 arcsec), which is significantly larger than the typical FWHM seeing ( $\sim 1.5$  arcsec) for any given observation. The 9 arcsec width corresponds, on average, to a projected physical width of 10 kpc (rms 3.6 kpc). The background level was estimated in two 15-pixel wide regions on either side of the source spectrum with a 15 pixel gap between the center of the source spectrum and the start of the background sampling regions. Two iterations of  $3\sigma$  rejection were done during both spectrum tracing and background level determination to reduce susceptibility to cosmic rays. Occasionally, spectra for other galaxies (in addition to the BCG) fell along the slit. We extracted these spectra as well in hopes of providing additional redshift information for the clusters.

The extracted 1D spectra were wavelength-calibrated by extracting identical regions of the companion arc lamp spectra obtained either just before or just after each galaxy spectrum. Helium-Neon-Argon arc lamps were used for these observations. The IRAF `dispcor` routine was used to perform the wavelength calibration. We typically used a 3rd order polynomial wavelength solution. The wavelength calibration was checked both by looking at the fit residuals provided in the IRAF `identify` and `reidentify` routines, and by confirming that the prominent night sky emission lines appeared at their proper central wavelengths. A final co-added 1D spectrum for each object observed on a given night was then produced from the individual wavelength-calibrated 1D spectra using the IRAF `scombine` routine. Any cosmic ray artifacts that may have survived the co-addition were manually removed via interpolation using IRAF’s `splot` routine.

#### 2.4.1. Redshift Measurements

Redshifts were measured using the IRAF-based RVSAO package `xcsao`. We used eight independent high S/N spectral templates of elliptical galaxies to perform the cross-correlations. These 8 templates include spectra of M32, NGC3379, NGC4648, NGC7331, the BCG in Abell 779, and three different composite spectra of low redshift early type galaxies. Eight templates are chosen to allow an estimate to be made of any systematic errors in the cross-correlation measurement. Regions around prominent night sky lines (Hg, NaD, OI) and strong atmospheric OH absorption bands were excluded from the fitting procedure. A galaxy redshift for each object was computed by first rejecting the templates with the highest and lowest redshift value and then averaging the results for the remaining six templates. For nearly all our high S/N spectra, however, all eight templates yielded consistent redshift values. The typical dispersion between templates was  $30 \text{ km s}^{-1}$  and the mean velocity error in our redshifts is  $45 \text{ km s}^{-1}$ . The average Tonry & Davis (1979) cross-correlation R-value, which quantifies the significance of the peak in the normalized cross-correlation function between the galaxy and template spectra is 8.6, with values ranging from 6 to 15 for the BCG candidates.

About 5% of our spectra have emission lines (only 8 of these emission line systems are BCGs). We used

the IRAF routine `rvidlines` to measure the redshifts of these objects. We typically were able to identify between 8 to 10 emission features in each spectrum in which emission was present. The velocity error in a typical emission-line based redshift is  $30 \text{ km s}^{-1}$ . Table 6 lists the IDs, celestial coordinates, heliocentric redshifts and errors for galaxies, as well as the mean Tonry & Davis (1979) R values.

The mean absolute-value velocity difference for  $\sim 200$  objects with multiple observations is  $39 \text{ km s}^{-1}$  with a standard deviation of  $41 \text{ km s}^{-1}$ . The mean absolute-value velocity difference between our redshift measurements and that from SDSS DR7 (Abazajian et al. 2009) for 82 galaxies in common between the two surveys is  $33 \text{ km s}^{-1}$  with a standard deviation of  $31 \text{ km s}^{-1}$ . In both comparisons, any potential systematic shifts are comparable to or less than the scatter in the common measurements and are also comparable to or less than the individual measurement errors.

#### 2.4.2. Velocity Dispersion Measurements

We measured central stellar velocity dispersions from the extracted one-dimensional spectra using a “direct” penalized pixel-fitting method, as implemented the IDL code `pPXF`<sup>6</sup> (Cappellari & Emsellem 2004). We use the `pPXF` code in combination with single-burst stellar population synthesis models (Vazdekis et al. 2010) based on the empirical MILES stellar library (Sánchez-Blázquez et al. 2006), with a Chabrier-style initial mass function (model “Mbi1.30”)<sup>7</sup>. The templates span a range of metallicities ( $-1.71 < [Z/H] < +0.22$ ) and single-burst ages ( $1 \text{ Gyr} < \text{age} < 17.8 \text{ Gyr}$ ). As part of the fitting process, `pPXF` finds the linear combination of templates that best reproduces the galaxy spectrum. These models are convolved with the instrumental resolution for each observing run, which is modeled using a low-order polynomial fit to the width of the arclines, and typically varies as a function of wavelength. We allow `pPXF` to fit for four velocity moments ( $V$ ,  $\sigma$ , h3, and h4) and use a fourth order multiplicative polynomial to account for continuum mismatch due to imperfect spectral flux-calibration. We mask regions covering possible strong emission lines (the Balmer lines and [OIII] $\lambda$ 4959,5007), and run the fit iteratively; on the first run, we identify  $\pm 4\sigma$  outliers in the fit residuals as noise spikes, mask them out, then rerun the velocity fits.

We further experimented with a number of model parameter choices that might introduce systematic effects into the  $\sigma$  measurements. The massive BCGs in our sample have non-Solar abundance ratios (in particular, they are enhanced in Mg, CN, and C<sub>2</sub>, e.g., Graves et al. 2007; Greene et al. 2013), while the stellar population templates have Solar-scale abundance patterns. We experimented with masking the absorption line regions strongly affected by these non-Solar abundances, but this had a negligible impact on the resulting  $\sigma$  measurements. We also investigated the effects of using the `pPXF` “BIAS” keyword to push the velocity solution toward low values of h3 and h4. This also had a negligible effect on our derived  $\sigma$  values. Fitting for only two velocity moments (i.e., setting h3 = h4 = 0) in some cases produced

<sup>6</sup> <http://www-astro.physics.ox.ac.uk/~mxc/idl/>

<sup>7</sup> <http://miles.iac.es//pages/ssp-models.php>

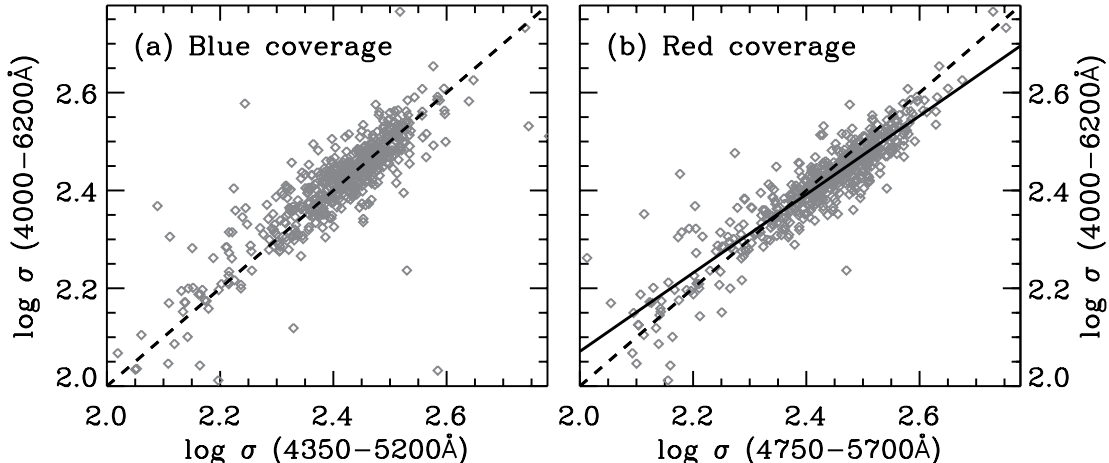


**Figure 5.** Comparing velocity dispersions measured from the “full” spectral range versus those measured from the more limited “blue” or “red” wavelength coverage. Open diamonds show individual galaxies in our sample. Dashed lines show a one-to-one relation. When only the blue wavelength range is used, the recovered velocity dispersions agree with those derived from the full spectral range (panel a). When only the red wavelength range is used, the measured  $\sigma$  values are biased high for high- $\sigma$  galaxies (panel b). We use a linear fit to the correlation to correct  $\sigma$  values measured in the red when the full spectral range is not available (solid line).

a modest increase in the derived  $\sigma$  values, as did using a higher-degree multiplicative polynomial for the continuum adjustment. There was little effect for galaxies with  $\sigma \sim 150 \text{ km s}^{-1}$ , but increases of  $\sim 20 \text{ km s}^{-1}$  for galaxies with  $\sigma \sim 350 \text{ km s}^{-1}$  were seen. We elected to use the fourth order multiplicative polynomial and unbiased four moment velocity fits for our final measurements.

By far the largest systematic effect was the choice of rest-frame wavelength interval used in the velocity fits, with  $\sigma$  values biased by up to  $\sim 40 \text{ km s}^{-1}$  when comparing different wavelength intervals. Our observations were not acquired with uniform wavelength coverage (see Table 5). Accordingly, we define three rest-frame wavelength ranges to use in our analysis. The “full” range of 4000–6200Å was available for nine of our 14 observing runs. We also defined a more limited “blue” range of 4350–5200Å for runs CT92F, CT93S, and KP92S, and a “red” range of 4750–5700Å for runs CT94F and CT94S. For the nine runs with full wavelength coverage, we measured  $\sigma$  from the “blue”, “red”, and “full” wavelength separately, in order to calibrate the effect of differing wavelength coverage as described below.

Due to imperfect data archiving, we were only able to retrieve pixel-by-pixel error arrays for a subset of the observing runs. The pPXF code uses error spectra both to penalize low-S/N or bad pixels in the fitting process and to estimate errors in the derived parameters, such as  $\sigma$ . We were able to use the iterative outlier rejection described above to mask bad pixels, with all other pixels being assigned equal weight. In order to estimate the uncertainties in measured values of  $\sigma$ , we again resorted to iterative use of the pPXF code. In the first run, all pixels were simply assigned equal (and arbitrary) errors. pPXF outputs the residuals between the best-fitting template combination and the observed spectrum, which have Gaussian scatter about zero. We used the width of the scatter as an estimate of the typical flux error per pixel, then reran pPXF using this value as the input error for all pixels to propagate through the resulting uncertainties in  $\sigma$ . Where the true error spectra

were available, we could compare these estimated errors in  $\sigma$  with the true errors; the difference in error estimates was Gaussian with a mean offset of  $0.63 \text{ km s}^{-1}$  and width of  $0.75 \text{ km s}^{-1}$ . This means that where we could compare them, the bootstrapped error estimates agreed with the true statistical error estimates to within  $1\text{--}2 \text{ km s}^{-1}$ . This made us confident that bootstrapped errors could be used reliably for observations whose error spectra had been lost. Overall, the typical uncertainty in our  $\sigma$  measurements is  $\sim 14 \text{ km s}^{-1}$ , but varies substantially between observations, depending on the spectral S/N and wavelength coverage.

For runs with full wavelength coverage, we compared the  $\sigma$  measurements from the full 4000–6200Å range to those derived from the more limited blue (4350–5200Å) or red (4750–5700Å) wavelength ranges in the same spectra, as shown in Figure 5. This calibration demonstrates that when only the blue coverage is available the resulting  $\sigma$  measurements are unbiased. The mean offset between the blue and full coverage  $\sigma$  values is  $-3.2 \text{ km s}^{-1}$ , with rms scatter of  $19.6 \text{ km s}^{-1}$  and no clear trend with  $\sigma$ . In contrast, measurements made with only the red coverage show substantial bias; the mean offset is  $+9.3 \text{ km s}^{-1}$  but increases to  $\sim 30 \text{ km s}^{-1}$  for the highest  $\sigma$  galaxies, with similar scatter of  $20.7 \text{ km s}^{-1}$ . To put all of our targets onto the same effective system, we fit a line that defines the “correction” from the red coverage onto the full coverage values. This correction is applied to the  $\sigma$  measurements from the CT94F and CT94S runs, which only have the red wavelength coverage. No correction is applied to the runs with blue coverage.

The spectroscopic observations include many repeat measurements of individual targets, usually in different runs. These can be used to test the internal consistency of our  $\sigma$  measurements. Using only  $\sigma$  measurements made from the full spectral coverage, we find that differences between repeat measurements of galaxies are Gaussian distributed with a standard deviation of  $16.5 \text{ km s}^{-1}$ . This is comparable to the expected typical statistical error of  $14 \text{ km s}^{-1}$ , suggesting that the  $\sigma$  measure-

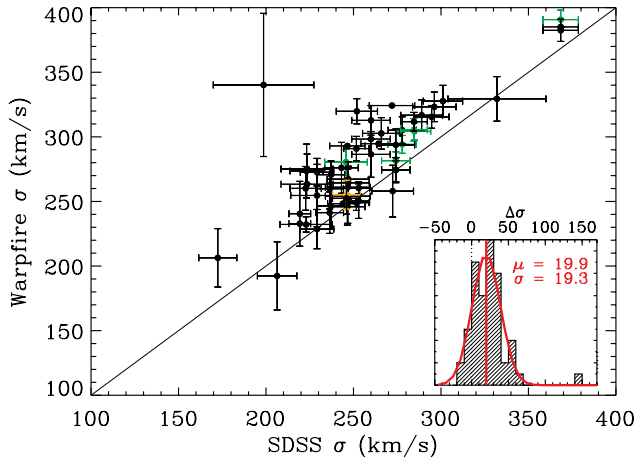


**Figure 6.** A comparison of our  $\sigma$  measurements versus those from the SDSS spectroscopic survey for galaxies in common. Black, green, and orange data points are from the KP96S, KP93S, and KP92F runs, respectively. The solid line shows the one-to-one relation. The inset panel shows a histogram of the offsets between the present and the SDSS measurements. These are Gaussian distributed (red curve) with a mean offset of  $19.9 \text{ km s}^{-1}$  and scatter of  $19.3 \text{ km s}^{-1}$ . The scatter is comparable to what is expected from the combined present and SDSS observational errors. We do not correct our  $\sigma$  measurements onto the SDSS system, but merely note that they are offset to higher values.

ments are stable across the various runs. This is not a trivial statement, given that the observations use two different telescopes, different instruments and instrumental configurations, and span multiple years including instrument upgrades. Comparing repeat observations on a run-by-run basis, the runs showing the largest mean offsets from the rest are KP92S ( $-18.6 \text{ km s}^{-1}$  for 16 galaxies), CT93S ( $17.3 \text{ km s}^{-1}$  for 4 galaxies), and KP94F ( $-12.3 \text{ km s}^{-1}$  for 12 galaxies). Notice that none of these deviant runs are the “corrected” runs with only red wavelength coverage. All other runs show offsets that are  $< 10 \text{ km s}^{-1}$  from the aggregate.

Where multiple observations are available, rather than averaging the individual measurements, we assign a “best” measurement for each galaxy. For the vast majority of the sources, the various observations agree within the estimated  $3\sigma$  errors; for these sources, the best measurement is the one with the smallest formal error in  $\sigma$  (i.e., that measured from the highest-S/N spectrum). For the six galaxies where repeat measurements show catastrophic disagreement ( $> 3\sigma$ ), we choose the best observation based on the following criteria: full wavelength coverage is preferred over limited red or blue coverage, spectra with noticeable flux calibration or sky subtraction issues are disfavored, higher S/N is preferred over low S/N, and better wavelength coverage is preferred over higher S/N. These measurements and calibrations result in a sample of 689  $\sigma$  “best” measurements among our galaxies.

Finally, 78 of our galaxies are in the SDSS spectroscopic survey, making it possible to compare our  $\sigma$  measurements to those from the SDSS spectroscopic pipeline (Bolton et al. 2012; see Adelman-McCarthy et al. 2008 for a comparison of different velocity dispersion algorithms in SDSS). This comparison is shown in Figure 6. The overlapping galaxy sample is mostly from the KP96S run (black points), with a few from KP93S (green

points) and one from KP92F (orange point). The solid line shows the one-to-one relation. The inset panel shows a histogram of the differences between our  $\sigma$  and the SDSS  $\sigma$  measurements. These have a Gaussian distribution with a mean offset of  $19.9 \text{ km s}^{-1}$  and width of  $19.3 \text{ km s}^{-1}$ . The scatter compares favorably with the estimated statistical errors in the measurement ( $\sim 17 \text{ km s}^{-1}$  for the typical errors from our observations and those from the SDSS combined in quadrature) and the internal consistency of our repeat measurements ( $16.5 \text{ km s}^{-1}$ ). However, there is a significant systematic offset of  $\sim 20 \text{ km s}^{-1}$ . The larger angular apertures ( $\sim 9''$ ) of the spectral extractions used in this work relative to the  $3''$  fiber apertures used in SDSS may explain some of the systematic shift if the trend of increasing stellar velocity dispersion with increasing radius, like that seen in the BCG in Abell 383 (Newman et al. 2011), is typical. We do not attempt to “correct” our values onto the SDSS system, but note that work combining  $\sigma$  measurements from different sources and spectral reduction pipelines must take such systematic variations into account. Dispersion values for the BCGs and M2 galaxies are listed in Tables 7 and 8, respectively.

### 2.5. Derivation of the Cluster Redshifts

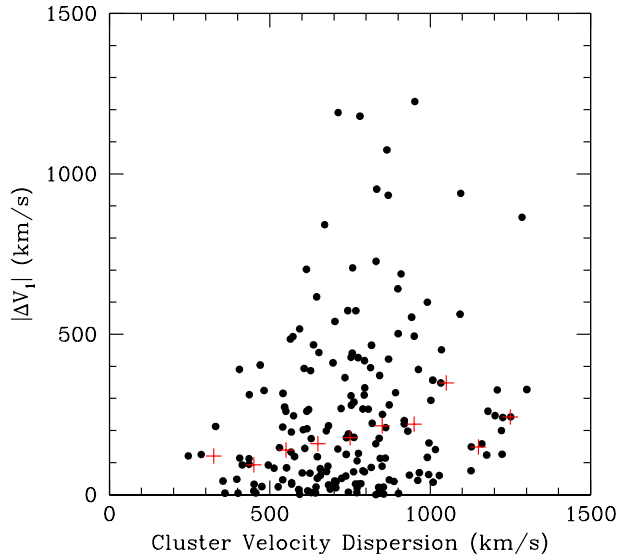
Cluster redshifts were derived based on galaxy velocities drawn from the database maintained by the NASA Extragalactic Database (NED), augmented by velocities measured for the BCG candidates by us, and SDSS Data Release 7 spectroscopy (Abazajian et al. 2009) where available. The “biweight” estimator of Beers et al. (1990) was used to calculate the mean cluster redshifts,  $V_c$ , and velocity dispersions,  $\sigma_c$ . The initial calculations used galaxies within  $\pm 3000 \text{ km s}^{-1}$  of the nominal BCG or estimated cluster redshifts, and the cluster Abell radius. While the biweight statistic is designed to be robust in the presence of background or foreground contamination, we still considered it prudent to remove obvious background contamination or other complexities, such as overlap with nearby clusters or groups. This was done by *ad hoc* inspection of the velocity maps and histograms for each cluster. A second robust statistic introduced by Beers et al. (1990) was used to estimate the cluster velocity dispersion for clusters with four or more velocities.

Table 1 lists the final number,  $N_g$ , of galaxy velocities used to compute the mean velocity and dispersion. This parameter is used as a general marker for the quality of both parameters. For some evaluations of the peculiar velocities of the BCGs within their clusters, we will restrict the analysis to clusters with  $N_g \geq 50$ , to minimize the effects of the error in the mean velocity. For analyses requiring accurate  $\sigma_c$ , we require the clusters to have  $N_g \geq 25$ .

## 3. THE LOCATION OF BCGS IN THEIR GALAXY CLUSTERS

### 3.1. The Peculiar Velocities of BCGs

The stereotypical image of a galaxy cluster has the BCG centrally located, both in projected angular coordinates and radial velocity relative to other cluster members. Studies of clusters with rich enough velocity sampling such that an accurate mean cluster redshift can be estimated, however, show that the BCG may often



**Figure 7.** The distribution of  $|\Delta V_1|$ , the absolute value of the peculiar velocity of the BCG within the cluster as a function of cluster velocity dispersion, for the 178 clusters with 50 or more galaxies with measured redshifts. The red crosses show the *median* peculiar velocity for each interval of  $100 \text{ km s}^{-1}$  in  $\sigma_c$  (except for the first bin, which runs from  $275$  to  $400 \text{ km s}^{-1}$ ).

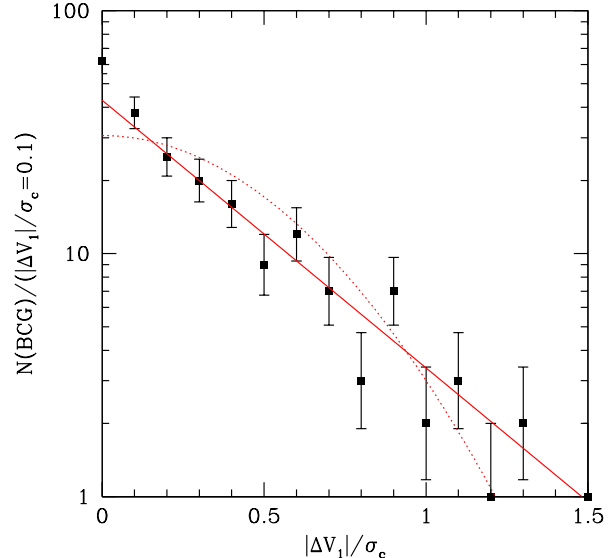
have a significant “peculiar velocity” with respect to their hosting cluster (Zabludoff et al. 1990; Malumuth 1992; Zabludoff et al. 1993; Oegerle & Hill 2001). PL95 obtained the distribution of BCG  $\Delta V_1 \equiv (V_1 - V_c)/(1+z)$  for 42 clusters with 20 or more member velocities, finding that the  $\Delta V_1$  followed a Gaussian distribution with  $\sigma_{\Delta V_1} = 264 \text{ km s}^{-1}$ , once the error in cluster mean redshift was accounted for. This value is  $\sim 0.4$  of the typical 1-D cluster velocity dispersion,  $\sigma_c = 666 \text{ km s}^{-1}$ , of the same subset of clusters. To test the hypothesis that the BCG peculiar velocities may be related to their masses, merger histories, and ages, we have derived the BCG peculiar velocity distribution function and investigated the relationship of this parameter to other BCG properties. The distribution function is considered in this section, while the relationship of BCG peculiar velocities to other BCG properties will be considered later in the paper.

Figure 7 shows the absolute values of  $\Delta V_1$  as function of cluster velocity dispersion for the 178 clusters in the present sample that have 50 or more member velocities. With this level of velocity information the error in the mean cluster velocity is  $\sim 100 \text{ km s}^{-1}$  or less, allowing relatively small  $\Delta V_1$  to be detected. As can be seen, most BCGs have  $\Delta V_1$  well in excess of this error threshold. The median peculiar velocity increases with  $\sigma_c$ . A power-law fit shows

$$|\Delta V_1| = 152 \pm 15 \left( \frac{\sigma_c}{600 \text{ km s}^{-1}} \right)^{0.66 \pm 0.26} \text{ km s}^{-1}. \quad (1)$$

Coziol et al. (2009) studied the distribution of BCG peculiar velocities in a large sample of Abell clusters and also found  $|\Delta V_1|$  to increase with  $\sigma_c$ , although they did not quantify the trend.

Figure 8 shows the binned distribution of  $\Delta V_1$  normalized by the cluster velocity dispersion. Normalizing by  $\sigma_c$  largely removes any dependence of the am-



**Figure 8.** The figure shows the binned distribution of  $|\Delta V_1|/\sigma_c$ , the absolute value of the radial velocity difference between the BCG and mean cluster velocity, normalized by the cluster velocity dispersion, for the 178 clusters with 50 or more galaxies with measured redshifts. The bins are  $0.1$  units wide. The solid line is an exponential with scale-length  $0.39$  in  $|\Delta V_1|/\sigma_c$ . The dotted line is the best-fit Gaussian distribution; it is clearly a poorer fit.

plitude of the peculiar velocity on the properties of the cluster itself. Since we are restricting this analysis to clusters with 50 redshifts or more, the errors on  $\Delta V_1/\sigma_c$  will be  $< 1/\sqrt{50} \approx 0.14$ . In normalized units, the mean  $\Delta V_1/\sigma_c = 0.04 \pm 0.04$ , with an rms dispersion of  $0.49$  — note that this number measures a different statistical property of the distribution than does the median peculiar velocity plotted in Figure 7. The two BCGs with the largest  $\Delta V_1/\sigma_c$  values are those in A2399 and A3764, which have  $|\Delta V_1|$  of  $1191$  and  $1180 \text{ km s}^{-1}$ , respectively, or normalized values of  $1.67$  and  $1.51$ .

The distribution of  $|\Delta V_1|/\sigma_c$  is exponential in form. Since the line-of-sight velocity distributions of galaxies in clusters are well known to be Gaussian (Yahil & Vidal 1977), a random draw of any non-BCG cluster member would, of course, echo this expectation. An exponential velocity distribution specific to the BCGs is thus surprising. The best-fitting exponential distribution is

$$\ln(N) = -2.54 \pm 0.18 |\Delta V_1|/\sigma_c + 3.76 \pm 0.20, \quad (2)$$

where  $N$  is the number of clusters per bin of width  $0.1$  in  $|\Delta V_1|/\sigma_c$ . The implied exponential scale length (the reciprocal of the slope given above) is thus  $0.39 \pm 0.03$  in  $|\Delta V_1|/\sigma_c$ ; this form and scale implies that the median  $|\Delta V_1|/\sigma_c$  is  $0.26$ . Note that for small  $|\Delta V_1|/\sigma_c$ , the observed distribution represents the convolution of an unknown intrinsic peculiar-velocity distribution with the error distributions of the BCG and cluster redshifts, plus the errors in the cluster dispersions. However, the observed distribution appears to be smooth and simple in form, thus the intrinsic distribution is likely to transition smoothly from BCGs with  $|\Delta V_1|/\sigma_c \approx 0$  to those with large  $|\Delta V_1|/\sigma_c$ , where the peculiar velocity of any given BCG is clearly significant.

The present distribution appears to be similar to that

measured by Coziol et al. (2009), although they did not characterize it with any functional form. We tested the likelihood that the distribution was non-Gaussian using an Anderson-Darling test (Stephens 1974), finding that a Gaussian distribution is strongly rejected. For the observed rms distribution of  $\Delta V_1/\sigma_c$  of 0.46, the Gaussian is rejected at the  $8 \times 10^{-6}$  significance level. Deletion of the two galaxies that have the largest relative peculiar velocities decreases the rms value of the distribution to 0.44, and the AD-test allows a Gaussian at  $6 \times 10^{-5}$  significance.

It has long been known that the difference in peculiar velocities of *pairs* of galaxies is exponentially distributed on small scales, both in observations of redshift-space distortions of the two-point correlation function and in simulations (Fisher et al. 1994; Marzke et al. 1995). This effect has been explained in terms of the number, rather than mass, weighting of galaxies in pair statistics (Diaferio & Geller 1996; Juszkiewicz et al. 1998). We are unaware of an equivalent study of BCG peculiar velocities in clusters. Reid et al. (2014), in their analysis of redshift-space distortions of SDSS/BOSS galaxies, identified massive halos at  $z \approx 0.55$  in a  $\Lambda$ CDM N-body simulation containing  $2048^3$  particles in a box  $677.7 h^{-1}$  Mpc on a side. They measured the difference in peculiar velocity between the most dense spherical region of radius 0.2 times the virial radius, and the cluster overall. Reid (private communication) finds that the distribution of this difference is accurately exponential in a variety of halo mass bins corresponding to rich clusters. While it is unclear whether the Reid et al. identification of the highest-density region in each halo is a good proxy for the BCG, this result is intriguing, and it would be interesting to explore more detailed cluster simulations in which individual subhalos can be identified.

The exponential distribution may reflect a dispersion in the ages of the clusters, the timing of when the BCG was captured by the cluster, or may simply be due to the superposition of Gaussian distributions of different velocity dispersions, weighted by the BCG number distribution (Diaferio & Geller 1996). BCGs in the tail of the exponential distribution may be those in which the BCG arrived to the cluster in the merger of a group or subcluster relatively recently, and not yet completely relaxed. These ideas could also be explored in simulations, or by looking for correlations between BCG peculiar velocity and signatures of merging in their host clusters.

### 3.2. The Projected Spatial Location of BCGs With Respect to the X-ray Centers

The X-ray emission from the intracluster medium provides insight into processes that govern the formation and evolution of the BCGs. Numerous investigations (Edge 1991; Edge & Stewart 1991; Hudson & Ebeling 1997; Collins & Mann 1998; Stott et al. 2012) find significant positive correlations between the total luminosity of the BCG and the X-ray luminosity and X-ray temperature. Schombert (1988) finds that the envelope luminosity of cD galaxies, a subset of the BCGs, increases with total cluster X-ray luminosity. Stott et al. (2012) find that the steepness of the  $L_X - T_X$  relation in galaxy clusters correlates with the stellar masses and X-ray offsets of their BCGs. Clusters in which the offset between the BCG position and the peak of the X-ray

surface brightness distribution is small tend to be the most regular, most massive systems (Allen 1998; Smith et al. 2005; Hudson et al. 2010). Haarsma et al. (2010) find that  $\sim 90\%$  of local ( $z < 0.2$ ) clusters host a BCG within  $\sim 30$  kpc of the X-ray peak, although their sample is small, and unlike us, they include a criterion of proximity to the X-ray peak for selecting the BCG from among candidates of “similar” brightness. Brough et al. (2005) find that the structure of the BCG correlates with cluster X-ray luminosity, with the BCG envelope becoming more extended in more luminous clusters.

Our sample is well suited to characterize the precise form of the distribution of the spatial offset,  $r_x$ , of the BCG from the peak of the intra-cluster medium (ICM) X-ray emission, and to assess whether the spatial offset correlates with the velocity offset of the BCG relative to the mean cluster velocity.<sup>8</sup> In addition, the availability of robust BCG profile shape measurements allows us to determine if the BCG stellar light profile is influenced by the spatial offset.

We cross-correlated our BCG catalog with the ROSAT-based X-ray Brightest Abell-type Cluster Survey (XBACS; Ebeling et al. 1996). XBACS is a flux-limited catalog derived from the ROSAT All-Sky Survey (RASS; Voges et al. 1999). Of the 283 Abell cluster sources listed in the VizieR version of the XBACS sample, 111 are in common with our current survey. An additional 70 clusters in our current sample have X-ray peak positions from the analysis of the RASS done by Ledlow et al. (2003), which extended to an X-ray flux limit that is  $\sim 7$  times lower than that used to derive the XBACS. Chandra X-ray Observatory data were obtained as well for 48 of the ROSAT clusters from the Archive of Chandra Cluster Entropy Profile Tables (ACCEPT; Cavagnolo et al. 2009), which we use in preference to the ROSAT peak positions given the superb Chandra angular resolution. We also searched the literature for XMM data but only 13 of the clusters in our sample have XMM data, too few to provide independent cross-checks on the ROSAT and Chandra samples. We thus focus our X-ray analyses on the above subsample of 174 clusters in our survey, using ROSAT data for 127 clusters and Chandra data for 47 clusters. We note that while Chandra is not a survey mission, the Abell clusters in our survey that have Chandra X-ray temperatures and luminosities that span the same range as the ROSAT temperatures and luminosities. No significant biases are introduced by including the Chandra data in our study of BCG dependence on the X-ray properties of their host clusters.

ROSAT and Chandra have very different on-axis point spread functions: FWHM of  $\sim 0.5$  arcseconds for Chandra vs.  $\sim 1$  arcminute for ROSAT. We used a sample of 101 Abell clusters (not limited by the redshift limits of our current survey) with observations from both observatories to measure the typical difference,  $\theta_x$ , between the ROSAT peak position and the Chandra peak position. The distribution of  $\theta_x$  is shown in Figure 9. The median and mean differences between the ROSAT X-ray position and the Chandra X-ray position are 43 arcsec-

<sup>8</sup> Many investigators prefer to normalize  $r_x$  by a cluster overdensity scale, such as  $r_{200}$  or  $r_{500}$ . Since these latter scales are proportional to  $\sigma_c$ , which only varies by  $\sim 2\times$  over the sample, this would make little difference for the  $r_x$  distribution, which extends over three orders of magnitude.

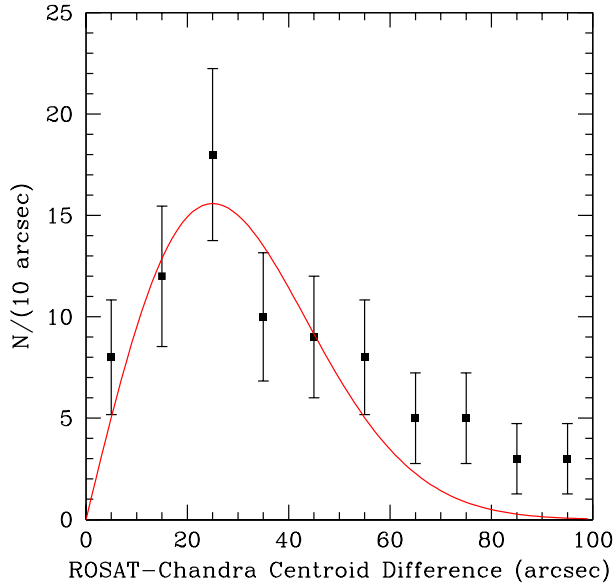


**Figure 9.** Histograms of the angular differences between Chandra and ROSAT centers for 101 Abell clusters with observations from both observatories. The red line gives a best-fit Rayleigh distribution (equation 3) based on the assumption of a circularly symmetric Gaussian model for the distribution of peak-location differences.

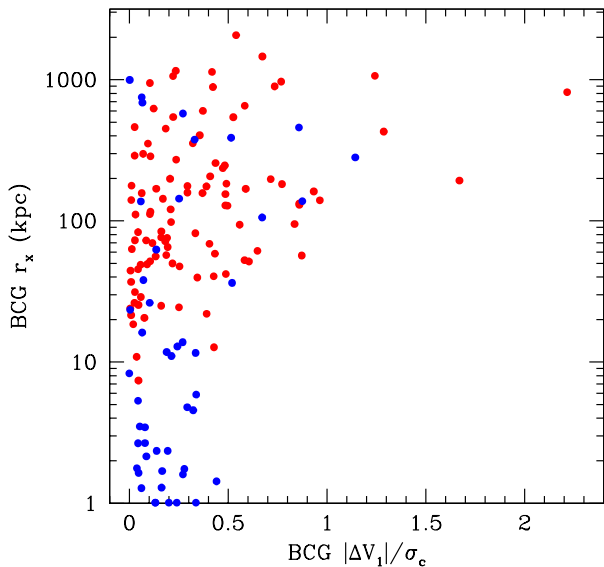


**Figure 10.** The radial offsets of the BCGs from the cluster X-ray center is plotted as a function of the absolute normalized peculiar velocity of the BCGs within the cluster. Clusters observed with Chandra are blue; those observed with ROSAT are red. Small radial separations ( $r_x < 40$  kpc) always correspond to small peculiar velocities ( $|\Delta V_1|/\sigma_c < 0.5$ ), while large peculiar velocities ( $|\Delta V_1|/\sigma_c > 1$ ) always correspond to large spatial offsets ( $r_x > 200$  kpc).

onds and 69 arcseconds, respectively. The median and mean difference between the ROSAT and the Chandra peak X-ray positions in projected physical distance units derived from cluster redshift information are 68 kpc and 121 kpc, respectively.

We characterize the distribution of differences between the location of the Chandra and ROSAT X-ray peaks

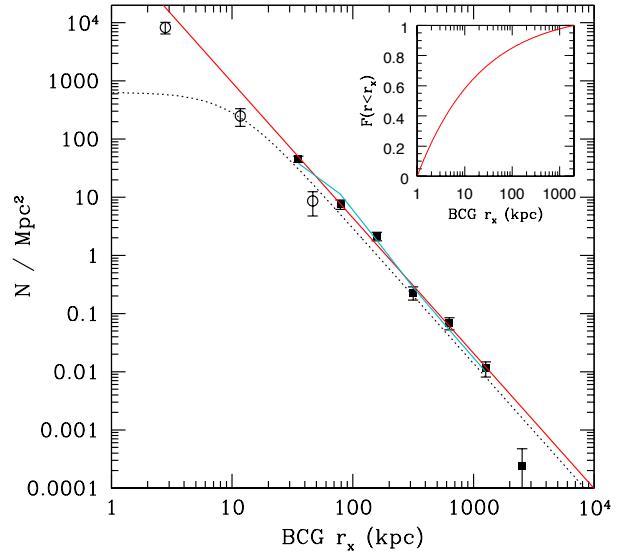


**Figure 11.** The surface density distribution of BCGs with respect to the cluster X-ray center. The normalization is set to provide a unit integral over the distribution (every cluster has one BCG). Solid points give the density of the full set of BCGs with measured X-ray offsets. The innermost bin extends from the center to 50 kpc; subsequent bins have outer limits geometrically increasing by a factor of two. Open points are the subset of BCGs that have cluster centers provided by Chandra, and thus are not resolution-limited on this scale. The inner bin from this set extends from the origin to 4 kpc, with the next two bins increasing geometrically by a factor of four. The red line is a power-law of index  $\gamma = -2.33$  fitted only to the full-set bins. The dotted line is a  $\gamma = -2.33$  power-law with a 10 kpc core (equation 5). The blue line is this form as “observed,” blurring it with a Gaussian with dispersion  $\sigma_x$  for the fraction of the clusters observed by ROSAT. The inset gives the cumulative integral of the pure power-law running from 1 kpc to 2 Mpc.

on the assumption that the distribution can be modeled as a circularly symmetric Gaussian. This will be almost entirely due to the large ROSAT PSF, but it may be more compact than that, given that the appropriate source of variance is the error in the ROSAT centers, rather than the width of the ROSAT PSF itself. The distribution of the total angular differences between the X-ray peaks will be a Rayleigh distribution,

$$p(\theta_x) = \sigma_x^{-2} \exp\left[\frac{-\theta_x^2}{2\sigma_x^2}\right] \theta_x d\theta_x, \quad (3)$$

where  $\sigma_x$  is the dispersion of the Gaussian, as well as the peak location of the above distribution. We fitted this form to  $\theta_x$  in 10-arcsecond bins, limited to the six bins around the peak of the distribution shown in Figure 9 to avoid the effects of extreme outliers. We measure  $\sigma_x = 25 \pm 3$  arcsec, or an implied FWHM of 60 arcsec for the underlying position-error Gaussian. The adopted distribution given by equation (3) for this  $\sigma_x$  is also plotted in Figure 9.

Figure 10 shows the offset between the BCG position and ROSAT position as a function of the velocity offset between the BCG and the cluster for the 174 clusters in our sample with ROSAT data. The somewhat triangular shape of the distribution of points shows that there is an overall correlation between the BCG spatial and velocity offsets. In particular,  $|\Delta V_1|/\sigma_c > 1$  occurs only for clus-

ters with  $r_x > 200$  kpc, while all  $r_x < 40$  kpc clusters have  $|\Delta V_1|/\sigma_c < 0.5$ . Stated qualitatively, BCG that are close to the X-ray center in projection always have relatively small velocities. Of course, with a large enough sample, there should be BCGs with high velocities seen in projection against the center; however,  $r_x < 40$  kpc corresponds to a very small portion of the projected area of the galaxy clusters.

Figure 11 shows the radial distribution of  $r_x$  for the subset of BCGs with cluster X-ray centers as a plot of BCG surface density as a function of radius. The normalization is set so that the cumulative integral over the surface density for each cluster is unity (each cluster has a single BCG). Generating this figure requires understanding the effects of the angular resolution on the X-ray peak locations obtained with ROSAT as well as how to incorporate the high-resolution Chandra data into the sample. As it happens, however, this is only a minor issue as the ROSAT data are used mainly at larger radii and the Chandra data are used exclusively at small radii.

The solid points in Figure 11 represent the entire X-ray sample, using both Chandra and ROSAT together, as radial bins of  $r_x$ . The innermost bin extends from the origin to 50 kpc, thus enclosing most of the ROSAT PSF. Subsequent bins are rings starting at 50 kpc, with inner and outer limits increasing geometrically by a factor of two. The data follow a simple power-law, which as we discuss below, appears to be the best form for the overall BCG spatial distribution. A log-log line fitted to the points gives the surface density as

$$\log_{10} \rho(r_x) = (-2.33 \pm 0.08) \log_{10} \left[ \frac{r_x}{1 \text{ kpc}} \right] + 5.30 \pm 0.19 \log_{10} [\text{N Mpc}^{-2}], \quad (4)$$

which is shown in the figure as the red line.

We used Monte Carlo simulations to understand the effects of the limiting ROSAT resolution on the apparent density profile, and to verify that the profile incorporating ROSAT data was consistent with the center of the distribution inferred from Chandra alone. For an assumed surface-density profile, we drew  $10^4$  “BCGs” for each cluster in the X-ray subset. For clusters observed by only by ROSAT, we scaled the angular position-error Gaussian to the appropriate physical resolution, given the redshift of the cluster, and drew a point at random from the circularly symmetric Gaussian centered at a radius drawn from the density distribution. For Chandra, we simply drew galaxies directly from the assumed profile. The form we tested included an inner quadratic-core to suppress the singular number integral as  $r_x \rightarrow 0$ , implied by the  $\gamma < -2$  power-law,

$$\rho(r_x) = \rho_0 \left( 1 + \left( \frac{r_x}{a} \right)^2 \right)^{\gamma/2}, \quad (5)$$

where  $a$  specifies the core scale, and  $\rho_0$  the central surface density.

We did not attempt to derive  $a$  formally, but simply compared the quality of the fits obtained by varying  $a$  geometrically in the sequence of  $a = 5, 10, 20$ , and 40 kpc. We fixed  $\gamma = -2.33$ , given its excellent description of the outer profile, where the ROSAT PSF would have little effect. As it happens, even with the large 50 kpc

outer limit of the inner-most bin using the full X-ray sample, we required  $a \leq 10$  kpc to obtain a satisfactory fit to the central point. The “observed” profile for  $a = 10$  kpc incorporating the blurring of the ROSAT offsets is shown in Figure 11 as the solid blue line, while the intrinsic unblurred-profile is shown as the dotted line. The effects of the ROSAT resolution is evident on the simulated profile, but with  $a = 10$  kpc, the form given by equation (5) just matches the central point. It is also noteworthy that the profile incorporating ROSAT data is indeed compatible the profile inferred from Chandra data alone.

The subset of Chandra observations underscores the conclusion that any core in the BCG  $r_x$  distribution must be extremely small. Figure 11 shows the implied surface density from the Chandra clusters alone. Again the Chandra points were incorporated into the bins representing the full sample, but here we can use considerably finer radial bins, given the superb Chandra angular resolution. The inner Chandra bin extends from the origin to 4 kpc, with the next two bins covering 4-16 and 16-64 kpc. The inner-most Chandra bin is fully an order of magnitude above the density implied by the  $a = 10$  kpc profile. The pure power-law fit given in equation (4) did not incorporate the central Chandra-only points, but its inward extrapolation clearly falls only slightly above them. In short, the BCG  $r_x$  distribution shows no sign of any core or decrease in slope as  $r_x \rightarrow 0$ .

### 3.2.1. Some BCGs Have Large X-ray Offsets

A radial integral over equation (4) gives the cumulative distribution of the BCGs away from the cluster X-ray center, which is shown as an insert in Figure 11. The integral starts at 1 kpc to avoid the central divergence, and continues out to include a few clusters with  $r_x > 1$  Mpc. The steep power-law form in equation (4) unifies two superficially different pictures of where BCGs are located in their hosting clusters. The median  $r_x$  implied by this distribution is only  $\sim 10$  kpc, and is consistent with the common impression that most BCGs reside close to the center of the X-ray gas, and presumably to the center of the cluster potentials. At the same time, the distribution also includes BCGs with large displacements from the X-ray defined center; 15% of the BCGs in the present sample have  $r_x > 100$  kpc, with the largest offsets reaching  $\sim 1$  Mpc. Because the finding that some BCGs may be greatly displaced from the center of the cluster potential is strongly at odds with the paradigm that BCGs should be centrally located (at least in relaxed clusters), we review the evidence for BCGs with large  $r_x$  and their import for understanding the formation of BCGs and clusters.

As noted in the Introduction, the first large survey of the X-ray morphology of galaxy clusters (Jones & Forman 1984) showed that the majority of systems have well-defined X-ray cores largely coincident with the position of a bright galaxy, typically the BCG. However, the same study also showed that if the cluster sample was sorted by X-ray core radius, the ensemble showed a smooth progression to clusters with large X-ray cores not coincident with any particular galaxy. To underscore this point we note two well-studied rich clusters that have long been known to have BCGs markedly displaced from the peak of the X-ray emission. A1367, part

of the present sample, is among the first examples found of a cluster with regular X-ray morphology, but with a large offset between the BCG (NGC 3842 in this case) and X-ray center (Bechtold et al. 1983); Table 7 gives  $r_x = 354$  kpc for this cluster. The Coma cluster (A1656) is the classic example of a rich galaxy cluster, yet it also is a system with a large BCG/X-ray offset, having  $r_x = 256$  kpc. White et al. (1993) analyzed a deep ROSAT image of Coma, and in conjunction with the positions and X-ray morphology of its two bright central elliptical galaxies, NGC 4889 (the BCG) and NGC 4874 (M2), concluded that Coma was produced in a still ongoing merger of two massive clusters.

Martel et al. (2014) emphasize that the BCG offset from the cluster center of mass (which may be different from the location of the peak X-ray emission), as well as the velocity offset discussed in the previous section, is a signature of the assembly of galaxy clusters by hierarchical merging. The BCG itself may be introduced into the cluster as part of an infalling group. A key point is that the galaxies, X-ray gas, and the dark matter halo of the cluster all have strongly different mechanisms and time scales for relaxing after cluster mergers. While we might expect the X-ray morphology of the cluster to be disturbed by strong or recent mergers with smaller clusters or groups, it is likely that the regularity of the X-ray gas distribution is re-established before any new BCG introduced by the merger is dynamically “captured” by the central potential. The regularity of the X-ray morphology plus the amplitude of  $|\Delta V_1/\sigma_c|$  and  $r_x$  in fact may provide means to constrain the recent merger history of clusters.

Previous studies of the location of BCGs with respect to the peak of the X-ray emission have produced diverse results. Patel et al. (2006) measured  $r_x$  for a sample of 49 clusters and found  $r_x > 100$  kpc in 16 systems, or 33% of the sample, a fraction considerably larger than the 15% that we found. The positional accuracy of their centers is low, so a large fraction of the measured offsets with  $r_x \sim 100$  kpc may really be significantly smaller; however their  $r_x$  distribution has a long tail extending to three clusters with  $r_x > 500$  kpc. In contrast, Haarsma et al. (2010) find  $r_x > 100$  kpc for just one cluster out of their small sample of 33, although, as we noted above, they also included proximity to the X-ray peak as a criterion for selecting their BCGs in the first place. It does appear that there is an important distinction between searching broadly within the cluster for the BCG versus selecting the brightest galaxy within the core of the X-ray emission. Hashimoto et al. (2014) explicitly limited their search for the BCG to within 500 kpc of the X-ray peak, but found offsets out to this limit.

While we have used extensive imaging and velocity observations to cast a wide net for the BCG in any cluster, we have relied on the literature to provide the matching X-ray centers. In order to understand the reliability of the largest BCG/X-ray offsets seen in our sample, we obtained archival Chandra or ROSAT images for the subset of clusters with  $r_x > 500$  kpc. Of the clusters with X-ray centers available, we initially identified 29 clusters with  $r_x > 500$  kpc. Of these, we accepted 22 clusters as credible systems with  $r_x$  of this amplitude. Our criterion was that the X-ray center had to fall within the extended X-ray source closest to the BCG that was associated with

galaxies consistent with the cluster redshift.

Of the seven clusters rejected, three were cases in which the X-ray emission was from either a foreground or background system seen in projection close to the nominal cluster, which itself had no detectable X-ray emission. Since we thus had no valid X-ray center, these clusters were dropped from the set with X-ray data. In four clusters, the clusters were either binary, with the BCG clearly associated with a different X-ray component than we had assumed, or the X-ray emission from a projected cluster at different redshift had been selected over the X-ray emission from the nominal cluster. In these cases we remeasured the  $r_x$  with respect to the revised centers. In one cluster, A0548,  $r_x$  decreased, but still remained  $> 500$  kpc. In the end we conclude that 22/174 or 12% of the sample has  $r_x > 500$  kpc. We show X-ray maps for four examples of clusters with  $r_x \sim 1$  Mpc in Figure 12. The clusters have well-defined central X-ray emission, but their BCGs are well outside of it.

In addition to these observational tests, we are encouraged by the cluster formation simulations of Martel et al. (2014), which produce ensembles of clusters that exhibit both the large  $|\Delta V_1/\sigma_c|$  and  $r_x$  seen in the present sample. Martel et al. argue that their simulations support cluster formation by the “merging group scenario.” As various groups merge with the cluster over the age of the Universe, the identity of the BCG may change several times. Newly arrived BCGs can be marked by high  $|\Delta V_1/\sigma_c|$  and large offsets from the center of their clusters, which we characterize with  $r_x$ .

The history of many of the more massive clusters simulated by Martel et al. (2014) show significantly long periods during which the BCG lies at a projected distance of more than 500 kpc or even 1 Mpc from the cluster center. The typical value of  $|\Delta V_1/\sigma_c|$  is found to range over 0.15 to 0.31 for Abell-like clusters, in excellent agreement with the median value of 0.26 found for our sample in the previous section. The maximum value of  $|\Delta V_1/\sigma_c|$  seen in the simulations may briefly exceed 1.5 in the early stages of a merger, again in good agreement with the observational limits on the BCG peculiar velocities. We argue later in this paper that additional lines of evidence support the merging-group scenario.

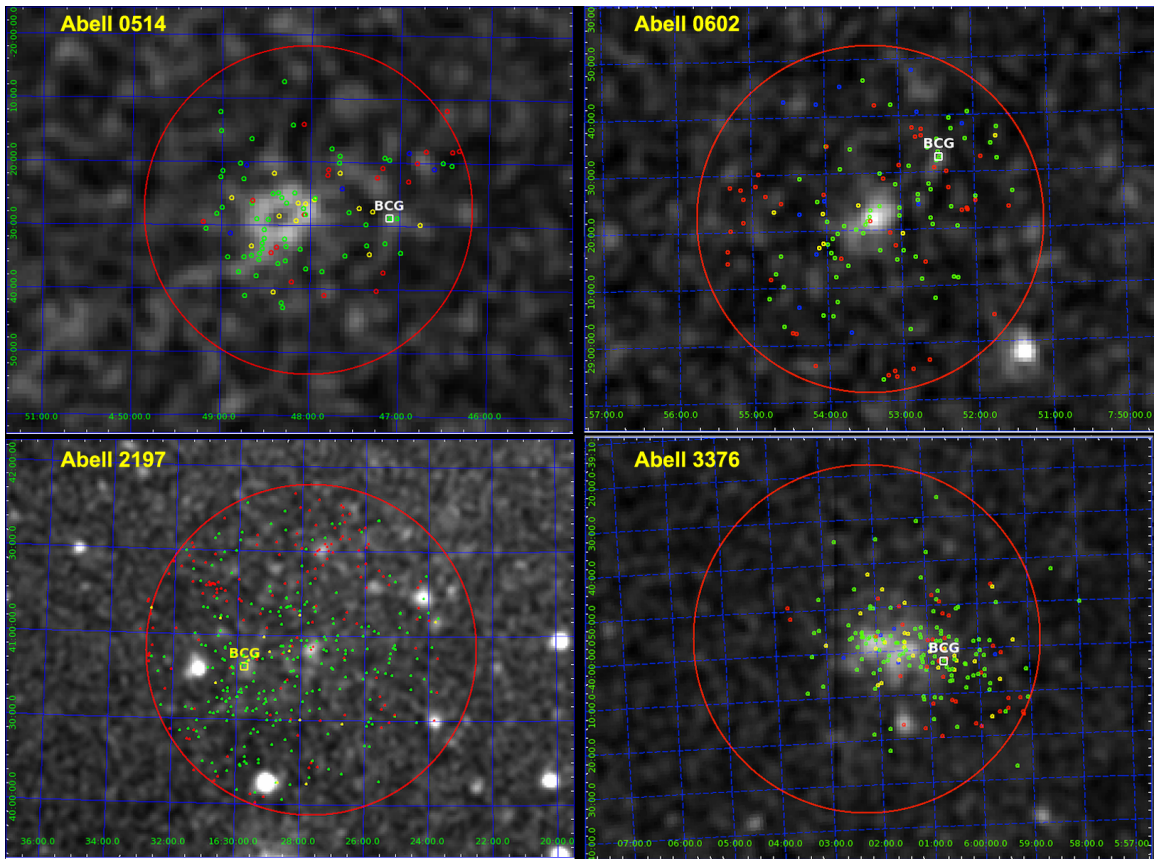
#### 4. THE PHOTOMETRIC AND KINEMATIC PROPERTIES OF BCGS

The average luminosities of BCGs have long been known to have relatively little dispersion, allowing these galaxies to be used as “standard candles” (Humason et al. 1956; Sandage 1972a,b). In this section we will explore the luminosity distribution function of BCGs and its relationship to other physical properties of the galaxies, such as their concentration and central stellar velocity dispersion. The BCG metric luminosities and structural parameters are tabulated in Table 7. The CMB frame has been assumed for calculation of all parameters.

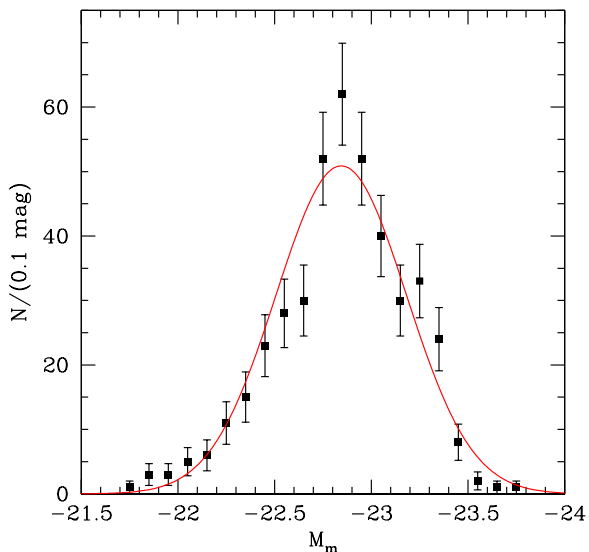
##### 4.1. The Metric Luminosity of BCGs

Figure 13 shows the distribution of  $M_m$  for the present sample, where we have applied the extinction and k-corrections outlined in §2.3.2 to the observed  $R_C$  surface photometry. The distribution is well fitted by a Gaussian with mean  $-22.844 \pm 0.016$ , and standard deviation of  $\sigma_L = 0.337$  mag. This is good agreement with





**Figure 12.** ROSAT All-Sky Survey images (smoothed with a gaussian) are shown for four clusters with  $r_x \sim 1$  Mpc. For A0514  $r_x = 1060$  kpc, A0602  $r_x = 1134$  kpc, A2197  $r_x = 886$  kpc, and A3376  $r_x = 995$  kpc. The large circle marks the Abell radius centered on the peak of the X-ray emission. The location of the BCG is indicated. Points mark galaxies with measured velocities, with green for galaxies within  $1000 \text{ km s}^{-1}$  of the mean cluster velocity, yellow for galaxies within  $1000$  to  $1500 \text{ km s}^{-1}$  of the mean, red for galaxies with velocities  $> 1500 \text{ km s}^{-1}$  above the mean, and blue for galaxies with velocities  $> 1500 \text{ km s}^{-1}$  below the mean. In all four clusters the BCG clearly falls within the velocity and spatial distributions of cluster galaxies, but are markedly displaced from peak of the associated X-ray emission.



**Figure 13.** The binned distribution of metric luminosity,  $M_m$ , for the present BCG sample. The bins are  $0.1$  mags wide and the errors are from Poisson statistics. The red line shows the best-fit Gaussian, which has mean  $M_m = -22.844 \pm 0.016$  and  $\sigma_L = 0.337$  mag ( $R_C$  band).

$\sigma_L = 0.327$  mag measured from the 15K sample in PL95.

We have excluded three extremely faint BCGs of the total sample of 433 BCGs from the Gaussian fit and most of the analysis that follows. The lowest luminosity bin plotted in Figure 13 is  $-21.7 > M_m > -21.8$ , which contains a single BCG.<sup>9</sup> The three BCGs in question, those in A3188, A3599, and A3685, all have  $M_m > -21.46$ , which is yet fainter by  $\sim \sigma_L$ ; all are fainter than the mean  $M_m$  by  $> 4\sigma_L$ . A3599 and A3685 have very few cluster members with velocities and may not be real systems.

#### 4.2. The $L_m - \alpha$ Relationship

Hoessel (1980) observed a sample of BCGs to refine their use as “standard candles” in cosmological probes, finding that  $L_m$  correlated with the physical concentration of the galaxies. Elliptical galaxies have long been known to have a relationship between *total* luminosity and effective radius, which is reflected in the relationship between the metric luminosity and radial scale as well. Hoessel (1980) expressed the physical concentration of the BCGs in terms of  $\alpha$ , the logarithmic slope of the variation of  $L_m$  with the physical radius of the aperture,  $r$ , evaluated at the metric radius:

$$\alpha \equiv d \log L_m / d \log r \Big|_{r_m}. \quad (6)$$

<sup>9</sup> When we explicitly refer to  $L_m$  in magnitude units we will use the variable  $M_m$ , or absolute metric magnitude.

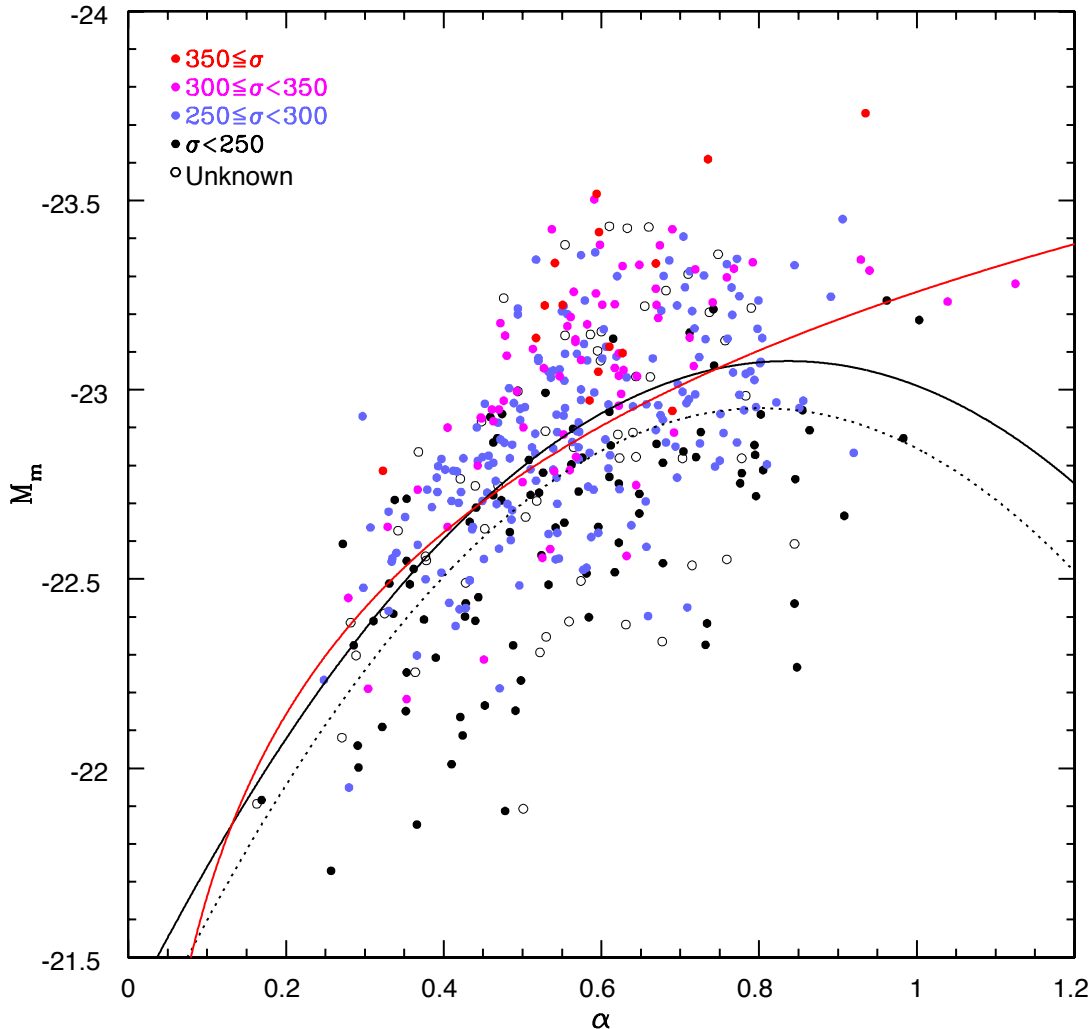


**Figure 14.** The relationship between metric luminosity,  $M_m$ , and  $\alpha$  is plotted for BCGs. The solid black line is the mean quadratic  $L_m - \alpha$  relation for the present sample, given by equation (7), while the red line fits the present sample with a linear function of  $\log \alpha$  (equation 8). The dotted line shows the quadratic  $L_m - \alpha$  relation of PL95 rescaled to  $H_0 = 70 \text{ km s}^{-1} \text{ Mpc}^{-1}$ . Symbols are color-coded by central stellar velocity dispersion,  $\sigma$ . Note that at any  $\alpha$ , objects with higher  $M_m$  typically have higher  $\sigma$ .

In addition to serving as a measure for the concentration of the BCGs,  $\alpha$  also relates the error in  $L_m$  to a corresponding distance error,  $\sigma_D = \sigma_L / (2 - \alpha)$  for using BCGs as standard candles. When  $\alpha = 0$ , all the galaxy light is contained within the aperture, and  $L_m$  is the total luminosity, while when  $\alpha = 2$ , the surface brightness distribution is constant with radius, and the metric luminosity provides no information on distance.

The  $L_m - \alpha$  relationship observed by Hoessel (1980) showed that  $\alpha$  initially increases steeply with  $L_m$ , then plateaus for the more luminous BCGs. LP94 and PL95 confirmed this behavior, and quantified it by fitting a quadratic relationship between  $L_m$  and  $\alpha$ , which they used as a distance indicator. For this application,  $\alpha$  is used to predict  $L_m$ , which in turn is used as a “standard candle” to infer the distance to the BCGs — in this case,  $L_m$  must be the dependent, rather than independent variable. The  $L_m - \alpha$  relationship for the present sample is plotted in Figure 14. A quadratic form fitted

to all BCG but the three with  $M_m > -21.5$  gives

$$M_m = -21.35 \pm 0.13 - (4.12 \pm 0.43)\alpha + (2.46 \pm 0.36)\alpha^2. \quad (7)$$

We note that we weight all points equally in this fit, and those that follow, unless we indicate otherwise. This is because the observed scatter around the relation of Eq. 7 is over an order of magnitude larger than the formal observational errors. The residuals about the relation are 0.267 mag rms in  $M_m$  in the CMB frame, essentially identical to the CMB-frame residuals of 0.261 mag for the 15K sample of LP94. In passing, we note that the quadratic form gives significantly smaller residuals in  $L_m$  than does a simple linear relation in  $\alpha$ , as we first showed in PL95. The bulk flow of the Abell cluster sample with respect to the CMB was derived by LP94 by finding the average BCG peculiar velocity field that minimized residuals in the  $L_m - \alpha$  relationship.

The quadratic form of the  $L_m - \alpha$  relationship derived

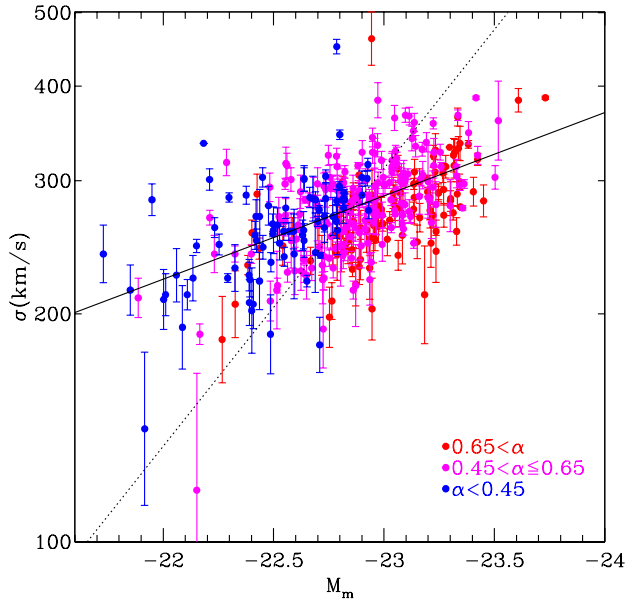


**Figure 15.** Central stellar velocity dispersion,  $\sigma$ , is plotted as a function of metric luminosity,  $L_m$ . The solid line is the mean relationship between the two parameters when  $L_m$  is the independent variable (equation 9). The dotted line is the relationship fitted when  $\sigma$  is the independent variable (equation 10). The points are color-coded by  $\alpha$ . Note that at any  $\sigma$ ,  $\alpha$  tends to increase with  $L_m$ .

by PL95 is also shown in Figure 14. The earlier relation falls  $\sim 0.1$  mag below the present relationship. The majority of this offset (0.06 mag) is likely to be due to our present use of Schlegel et al. (1998) extinctions rather than the Burstein & Heiles (1982) values used by PL95; the average  $A_B$  values from SFD are 0.10 mag greater than those of B&H for the 15K sample.

The quadratic form has the unattractive feature, however, of reaching maximum  $L_m$  at  $\alpha \sim 0.8$ , and then predicting fainter  $L_m$  as  $\alpha$  increases beyond this point where there are few BCGs to elucidate its behavior. This motivated us to introduce a new form, fitting  $L_m$  to a linear function of  $\log \alpha$ . This new form closely parallels the quadratic form over most of the domain, but is monotonic, and may better represent the handful of BCGs with  $\alpha > 0.9$ . This form has the additional advantage of requiring only two, rather than three parameters. For the present sample with  $M_m < -21.5$ , we measure

$$M_m = -23.26 \pm 0.03 - (1.597 \pm 0.104) \log_{10} \alpha. \quad (8)$$

The residuals in  $M_m$  are 0.271 mag rms in the CMB frame, only 0.004 mag larger than those for the form given in equation (7). This form is also plotted in Figure 14 and only strongly differs from the quadratic form for  $\alpha > 1$ , where we have very few galaxies.

#### 4.3. The $L_m - \sigma$ Relationship

Figure 15 plots the relationship between  $M_m$  and  $\sigma$ . While the measurement errors in  $\sigma$  are subdominant to the intrinsic scatter in this relationship, they are not completely negligible, and we have incorporated them into our fitting procedure, following the methodology described in Hogg et al. (2010) and Kelly (2011).

If  $M_m$  is treated as the independent variable, the relationship derived from a simple least-squares fit for the

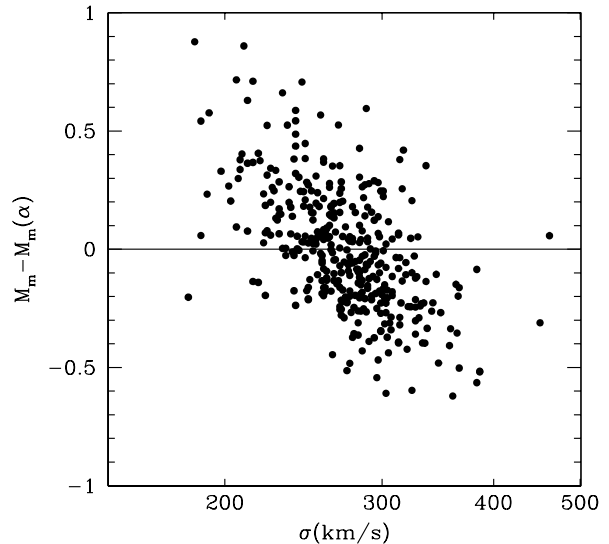


**Figure 16.** Residuals in  $M_m$  from the mean relationship between  $M_m$  and  $\alpha$  given by equation (8) and shown in Figure 14 are plotted as a function of central stellar velocity dispersion,  $\sigma$ . A clear correlation is evident in the sense that positive residuals (BCGs with fainter than the mean  $M_m$  for a given  $\alpha$ ) correspond to low  $\sigma$  and negative residuals correspond to higher values of  $\sigma$ .

369 galaxies with  $M_m < -21.5$  and measured  $\sigma$  is:

$$\log_{10} \left( \frac{\sigma}{300 \text{ km s}^{-1}} \right) = - (0.275 \pm 0.023) \left( \frac{M_m}{2.5} \right) - 2.55 \pm 0.21, \quad (9)$$

with  $0.052 \pm 0.02$  scatter in  $\log \sigma$ , corresponding to  $\pm 12\%$  in  $\sigma$ . Conversely, if  $\sigma$  is the independent variable, then

$$M_m = -22.956 \pm 0.015 - 2.5(1.09 \pm 0.08) \times \log_{10} \left( \frac{\sigma}{300 \text{ km s}^{-1}} \right), \quad (10)$$

with an intrinsic scatter of  $0.278 \pm 0.011$  in  $M_m$ , implying that  $\sigma$  is just as good as  $\alpha$  is for predicting  $M_m$ .

The slope in equation (9) is essentially the same as the classic Faber & Jackson (1976) result of  $\sigma \propto L^{1/4}$  for normal elliptical galaxies. This suggests that the central portions of the BCGs enclosed within  $r_m$  may have a “normal” relationship between  $\sigma$  and  $L$ , in contrast to that between *total* BCG  $L$  and  $\sigma$ . As noted in the Introduction, Oegerle & Hoessel (1991) and Lauer et al. (2007) found that  $\sigma$  is only weakly correlated with BCG *total* luminosity. This behavior may reflect the putative formation of BCGs by dry mergers of less luminous elliptical galaxies. Simulations of this process shows that  $\sigma$  remains essentially constant over dry mergers, with the effective radius,  $R_e$ , growing rapidly with  $L$  (Boylan-Kolchin et al. 2006). This associated steepening of the  $R_e - L$  relation has also been seen in BCGs (Lauer et al. 2007).

We also fitted the Faber-Jackson relationship with  $M_m$  measured at  $2\times$  and  $4\times$  the nominal metric radius to test the hypothesis that the relation between BCG  $L$  and  $\sigma$  becomes shallower as  $r_m$  increases to include a larger fraction of total galaxy luminosity. When the metric ra-

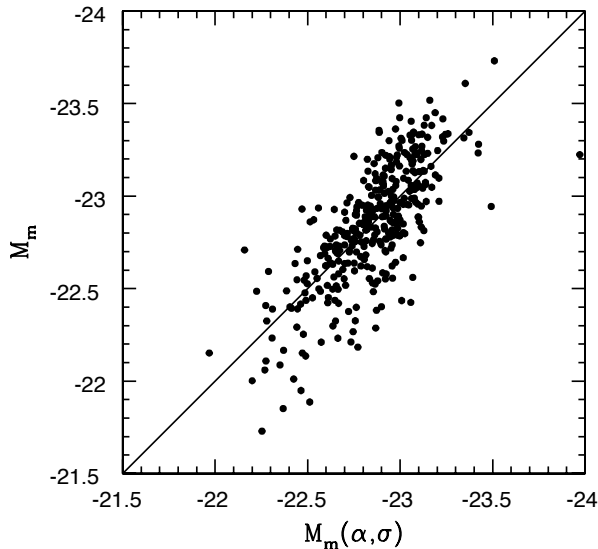


**Figure 17.** Metric luminosity is plotted as a function of  $M_m$  estimated from  $\alpha$  and  $\sigma$  through the multi-parameter relationship between the three parameters given by equation (13).

dus is doubled, we find

$$\log_{10} \left( \frac{\sigma}{300 \text{ km s}^{-1}} \right) = -(0.205 \pm 0.022) M_m(2r_m)/2.5 - 1.94 \pm 0.20, \quad (11)$$

for the 352 BCGs that have both valid  $\sigma$  and photometry at  $2r_m$ , with an intrinsic scatter of  $0.054 \pm 0.02$  in  $\log \sigma$ . For  $M_m$  measured at  $4r_m$  the sample decreases to 200 BCGs, and we measure

$$\log_{10} \left( \frac{\sigma}{300 \text{ km s}^{-1}} \right) = -(0.147 \pm 0.027) M_m(4r_m)/2.5 - 1.44 \pm 0.26, \quad (12)$$

with an intrinsic scatter of  $0.053 \pm 0.03$  in  $\log \sigma$ . In short, the slope decreases from  $\sim 1/4$  to  $\sim 1/5$  and then  $\sim 1/6$  as  $r_m$  is doubled twice. As even at  $4r_m$  the integrated luminosity of the BCGs is still increasing, the relationship for  $\sigma$  and total luminosity would be yet shallower.

#### 4.4. The $L_m - \alpha - \sigma$ “Metric Plane”

With the large 24K sample and improved knowledge of galaxy and cluster parameters over what was available to PL95, we can now better investigate sources of residual scatter in the  $L_m - \alpha$  or  $L_m - \sigma$  relationships. In fact, given the fundamental plane relationships between total  $L$ ,  $\sigma$ , and  $R_e$  (Dressler et al. 1987; Djorgovski & Davis 1987) for ordinary elliptical galaxies, it is not surprising to find that a multi-parameter “metric plane” relationship between  $L_m$ ,  $\sigma$ , and  $\alpha$ , has smaller scatter than those between any two of these parameters.

The points in the  $L_m - \alpha$  relationship shown in Figure 14 are color-coded by  $\sigma$ , showing a strong gradient such that at any  $\alpha$ , higher  $L_m$  is correlated with higher  $\sigma$ . Likewise, the color-coding of the points by  $\alpha$  in the  $L_m - \sigma$  plot in Figure 15 show that at any  $\sigma$ , higher  $L_m$  is correlated with higher  $\alpha$ . This behavior is shown more explicitly in Figure 16, which plots the  $M_m$  residuals from the mean  $L_m - \alpha$  relationship given by equation

(8), as a function of  $\sigma$ . A strong correlation is clearly evident.

Use of  $\alpha$  and  $\sigma$  together to predict  $M_m$  for the 368 galaxies with  $M_m < -21.5$  and measured  $\sigma$  gives the relationship,

$$M_m = -23.31 \pm 0.03 - (1.43 \pm 0.09) \log_{10} \alpha - (2.20 \pm 0.17) \log_{10} \left( \frac{\sigma}{300 \text{ km s}^{-1}} \right). \quad (13)$$

The intrinsic scatter is  $0.214 \pm 0.010$  in  $M_m$ , a marked improvement over the  $L_m - \alpha$  and  $L_m - \sigma$  relationships. Figure 17 plots observed  $M_m$  as a function of  $M_m(\alpha, \sigma)$  estimated from this relationship. This metric plane is not identical to a fundamental plane relation, but with  $L_m$  and  $\alpha$  serving as proxies for  $L$  and  $R_e$ , it encodes similar structural information. A detailed comparison between the metric plane and a true fundamental plane relation for the present sample is the subject of our second paper (Chisari et al. 2014).

#### 4.5. The Relationship Between BCGs and Their Clusters

##### 4.5.1. BCGs and the Bulk Properties of Clusters

As noted in the Introduction, the structure and luminosity of BCGs may be tied to the properties of the clusters as traced by the temperature and luminosity of the associated X-ray emitting gas. The present 24K sample suggests that BCG luminosity is also correlated with cluster velocity dispersion, which can serve as a proxy for cluster X-ray luminosity,  $L_X$ , given the relationship between the two cluster parameters (Solinger & Tucker 1972; Quintana & Melnick 1982; Wu et al. 1999; Mahdavi & Geller 2001).

Figure 18 plots cluster velocity dispersion as a function of both  $M_m$  and  $\alpha$  for the 259 clusters having 25 or more galaxy redshifts, the minimum number needed for accurate measurement of the velocity dispersion. While there is considerable scatter in the velocity dispersion at any  $M_m$  or  $\alpha$ , there is a clear correlation such that the median dispersion increases by nearly a factor of two over the range of both parameters. The relation between  $\alpha$  and  $\sigma_c$  in particular echoes the relation between the shallowness of the BCG surface brightness profile and cluster X-ray luminosity seen by Schombert (1988) and Brough et al. (2005).

Both correlations seen in Figure 18 raise the question of whether or not  $\sigma_c$  offers any independent information that can reduce some of the scatter in the  $L_m - \alpha$  relationship. Hudson & Ebeling (1997) argued that there is an  $L_m - \alpha - L_X$  relationship, which offers better prediction of  $L_m$  than using  $\alpha$  alone and in doing so reduces the significance of the LP94 bulk-flow amplitude. If we take  $\sigma_c$  as a proxy for  $L_X$ , we should thus expect to see a  $L_m - \alpha - \sigma_c$  relationship if the Hudson & Ebeling (1997) is highly significant.

Figure 19 plots the residuals of the  $L_m - \alpha$  relationship, given by equation (8), as a function of cluster velocity dispersion. The residuals of the  $L_m - \alpha$  relationship do show a barely significant correlation with cluster velocity dispersion in the sense that brighter residuals in  $L_m$  are still associated with clusters with higher velocity dispersion. The measured slope is  $-0.23 \pm 0.10$  mag per dex in dispersion, such that the mean  $M_m$  residuals decrease

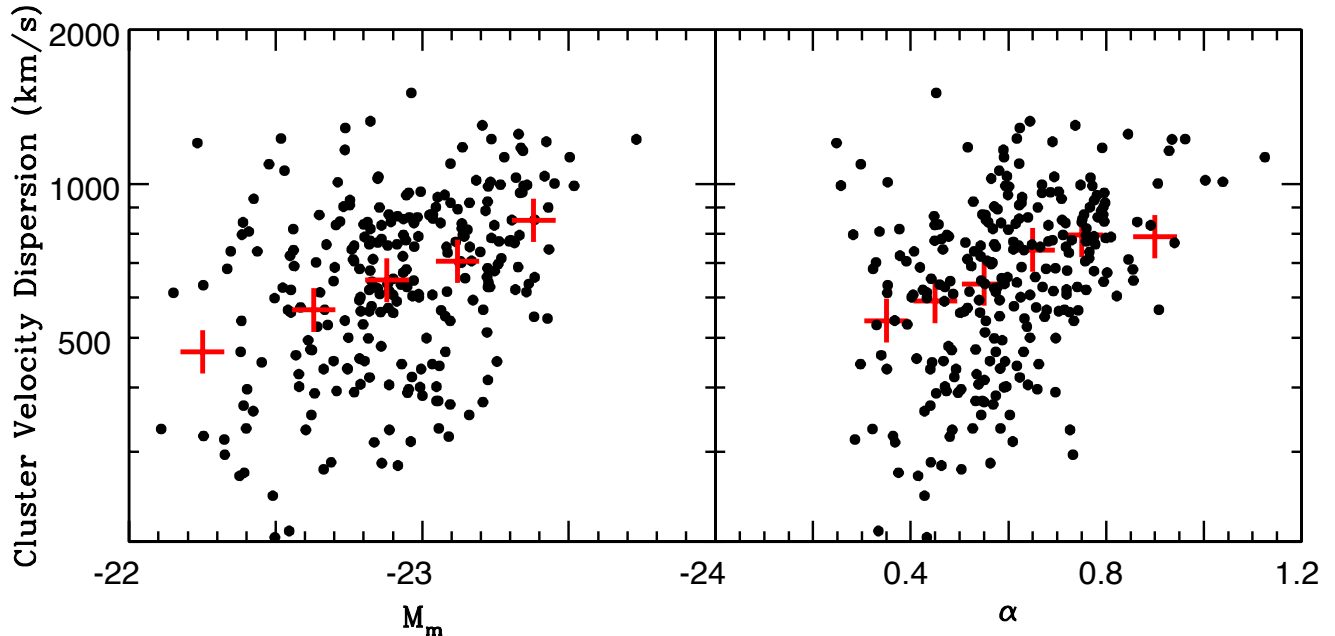


**Figure 18.** Cluster velocity dispersion is plotted as a function of BCG  $M_m$  (left panel) and  $\alpha$  (right panel) for the 259 clusters with 25 or more galaxy redshifts. The red crosses give the median velocity dispersion for each 0.25 mag in  $M_m$  or 0.2 bin in  $\alpha$ . Both parameters increase with velocity dispersion.

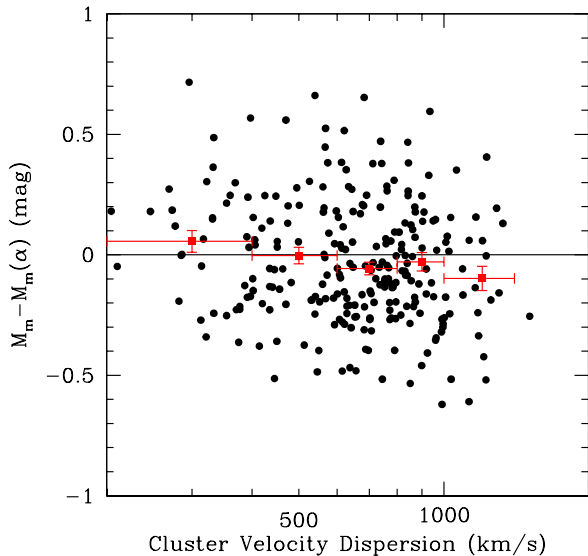


**Figure 19.** Luminosity residuals from the  $L_m - \alpha$  relationship (equation 8) are plotted as a function of cluster velocity dispersion for the 259 clusters with 25 or more galaxy redshifts. The red points give the mean residual in bins of width  $200 \text{ km s}^{-1}$  (except for the highest bin, which was widened to include more points). The mean of the  $M_m$  residuals decreases by  $\sim 0.15$  mag over the range of the cluster velocity dispersions.

by  $\sim 0.15$  mag over the sample range of cluster velocity dispersion.

The  $L_m - \alpha - \sigma$  relation (equation 13), however, “soaks up” this residual dependence on cluster velocity dispersion. When  $\alpha$  and  $\sigma$  are used to predict  $L_m$ , the remaining dependence on cluster velocity dispersion decreases

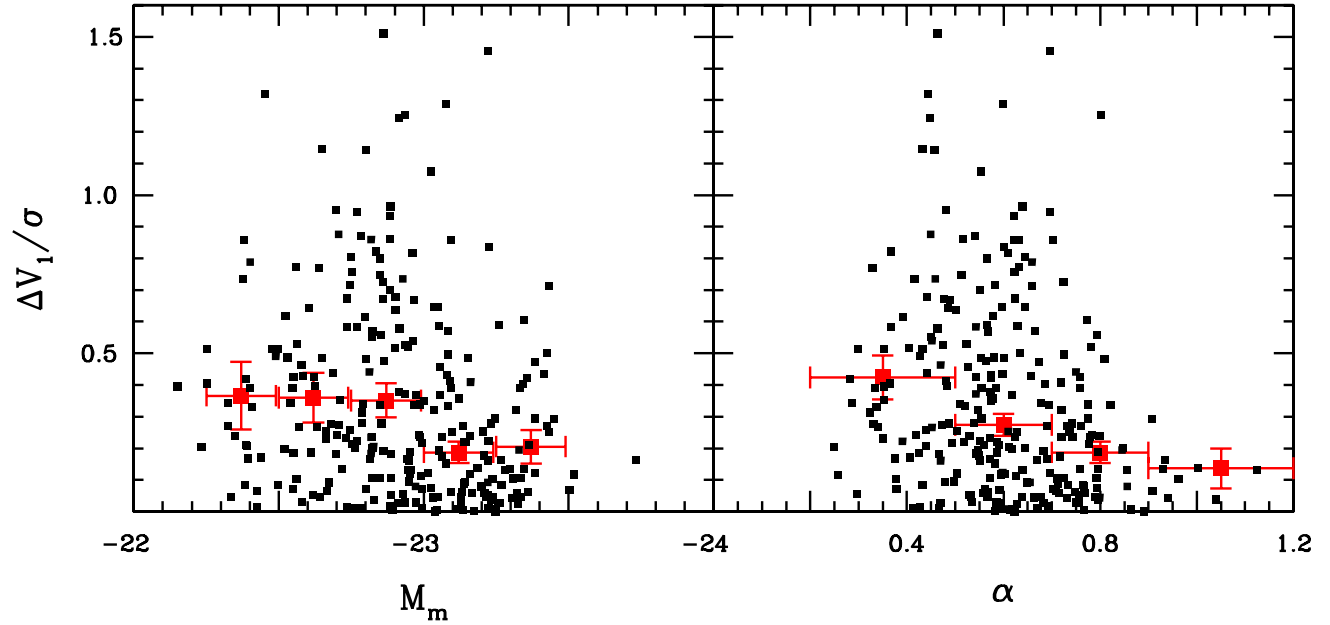
to  $\sim 0.07$  mag/dex with no significance over the sample range in dispersion. Notably, the  $L_m$  residuals from this relation are already slightly better than those of the Hudson & Ebeling (1997)  $L_m - \alpha - L_X$  relationship. The present  $L_m - \alpha - \sigma$  relation thus offers a BCG-based distance indicator with the effects of the cluster environment removed.

Both the metric luminosity and structure of the BCGs may also be related to the peculiar velocities of the BCGs within their hosting clusters. Figure 20 plots the peculiar velocities of the BCGs normalized by cluster velocity dispersion as a function of BCG  $L_m$  and  $\alpha$  for the subset of clusters with 25 or more members. The median peculiar velocity steadily decreases with increasing  $\alpha$ . The trend of median  $|\Delta V_1/\sigma|$  with  $M_m$  is less clear; however, the most luminous BCGs have relatively smaller peculiar velocities.

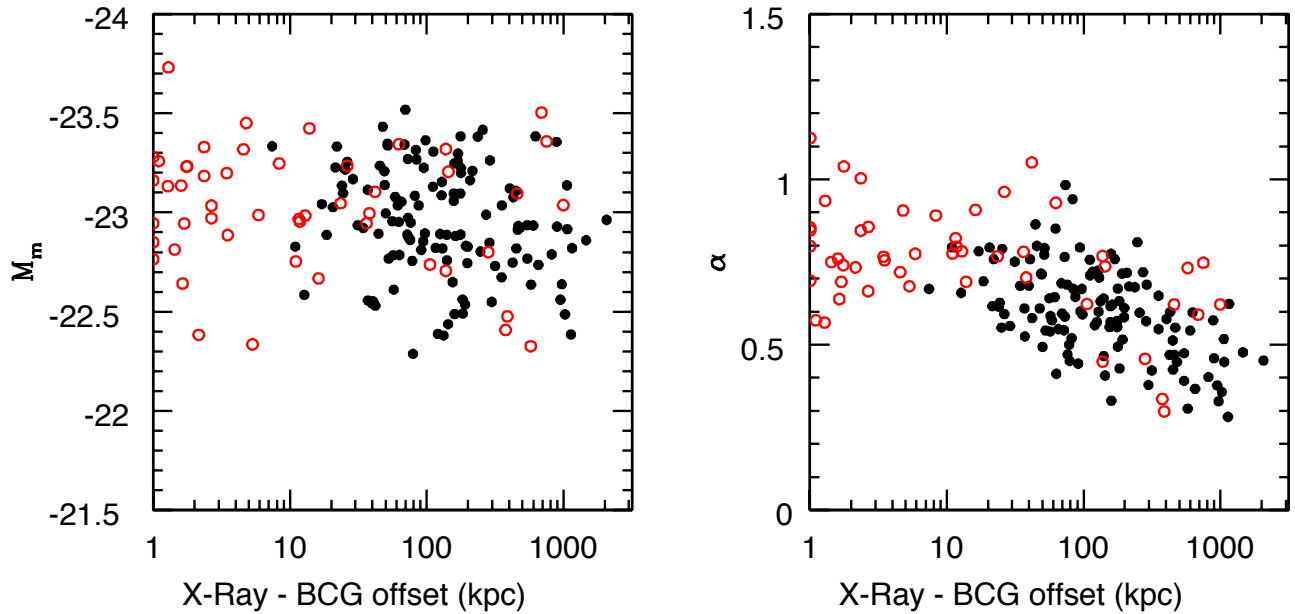
#### 4.5.2. The Structure of BCGs and Their Positions Within the Clusters

Figure 21 shows that  $\alpha$  is also correlated with the offset of the BCG within the cluster relative to the X-ray center. The right panel shows that  $\alpha$  is clearly larger for BCGs closer to the center of their clusters, while left panel of the figure shows that  $M_m$  is largely unrelated to the position of the BCG within the cluster. The former result appears to be consistent with the weak correlation discovered by Ascaso et al. (2011) between the effective radii of the BCGs and their spatial offsets, with larger BCGs being positioned closer to the centers of the clusters.

One possibility is that the increase of  $\alpha$  may be dominated by high-speed or non-merging interactions with other galaxies in the cluster. The interactions would preferentially take place more often at the center of the clus-



**Figure 20.** Absolute peculiar velocity of the BCGs normalized by cluster velocity dispersion is plotted as a function of BCG  $M_m$  and  $\alpha$  for the subset of clusters with 25 or more members. The red points gives the *median*  $|\Delta V_1/\sigma|$  in 0.25 mag bins in  $M_m$  or 0.2 bins in  $\alpha$ .



**Figure 21.**  $M_m$  and  $\alpha$  are plotted as a function of distance of the BCG from the X-ray defined center of the cluster. Solid black symbols indicate clusters with ROSAT measurements, while the open red symbols indicate clusters with Chandra-based X-ray centers. Little dependence on  $M_m$  with distance from the center is seen, while  $\alpha$  increases with decreasing distance.

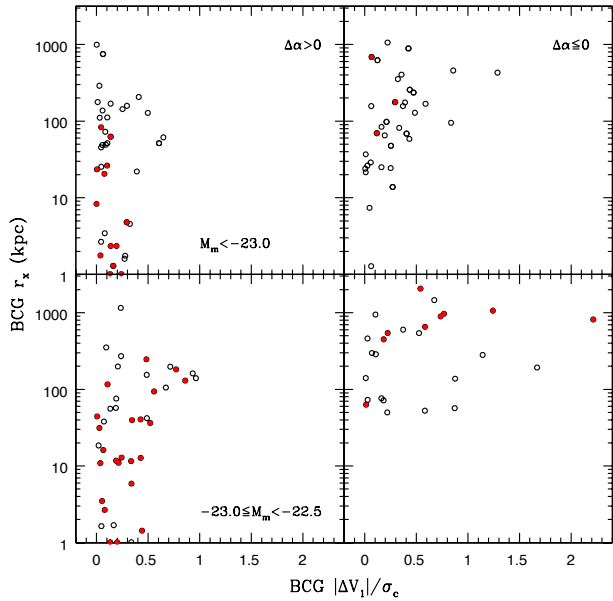


**Figure 22.** The distribution of BCG X-ray offset,  $r_x$ , and normalized velocity offset,  $|\Delta V_1|/\sigma_c$ , (for clusters with  $N \geq 25$  velocities) are shown for four regions in the BCG  $M_m - \alpha$  space. The columns separate BCGs by whether or not they fall above (left) or below (right) the mean relation of  $\alpha$  on  $M_m$  (equation 14). The rows then segregate the BCGs by  $M_m$  interval, with the brightest BCGs plotted in the top row. Red points are BCGs with  $\alpha$  deviating from the mean  $\alpha(M_m)$  relationship by  $1\sigma$  or more.

ter and would add energy to the stellar envelope of the BCGs, causing them to become more extended. Without actual mergers, however, little stellar mass is added to the BCGs, thus no overall luminosity growth occurs as the structure of the BCGs becomes more extended. A second hypothesis is that merging does occur as the BCG dwells within the cluster center, but the density of stars within the metric aperture does not increase in the process. Hausman & Ostriker (1978) argued that dry mergers in fact would cause little central growth of the BCGs, a phenomenon that is also seen in merger simulations (Boylan-Kolchin et al. 2006). Recent theoretical and observational work (Hopkins et al. 2009; van Dokkum et al. 2010) indeed argues that growth of massive galaxies since redshifts  $\sim 2$  is mainly in their outer envelopes.

Since both  $L_m$  and  $\alpha$  are related to the position of the BCGs with respect to both the spatial and velocity centroids of the clusters, we also examined the combined effect of the last two parameters. Figure 22 revisits the plot of the BCG spatial location within the cluster,  $r_x$ , versus the normalized absolute BCG peculiar velocity,  $|\Delta V_1|/\sigma_c$ , which was first shown for the full sample of BCGs with X-ray centers and accurate mean velocities in Figure 10. We now split the BCGs with  $M_m < -22.5$  into two luminosity bins,<sup>10</sup> each of which is split further into two halves by whether or not the galaxies are above or below the mean relation for  $\alpha$ , given  $M_m$ ,

$$\alpha(M_m) = (-0.256 \pm 0.019)(M_m + 22.5) + 0.484 \pm 0.009. \quad (14)$$

<sup>10</sup> There are very few BCGs with  $M_m > -22.5$  that have X-ray cluster centers available, thus we cannot do this analysis for the lower-luminosity BCGs.

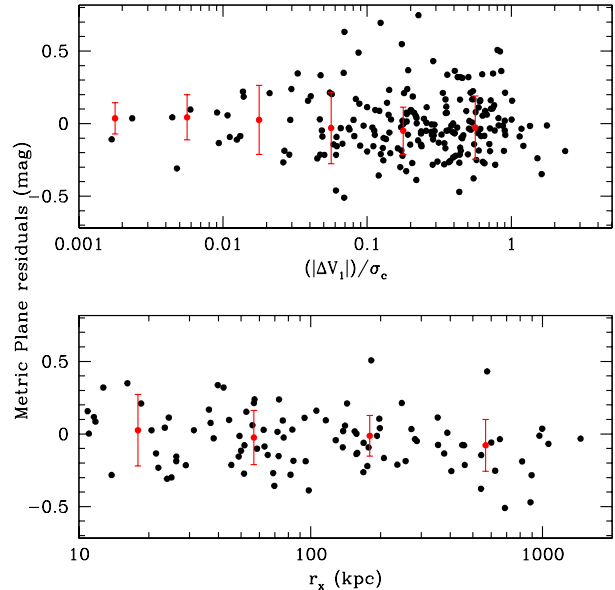


**Figure 23.** The magnitude residuals from the metric plane relation of Equation (13), shown as a function of velocity offset from the mean redshift of the cluster (upper panel) and positional offset from the X-ray center, where available (lower panel). As in Figures 8 and 22, the velocity offset is normalized by the velocity dispersion of the cluster. The median values in bins, and the one-sigma widths (as determined from the interquartile range) are also shown in red. There is no evidence for a systematic bias, or larger scatter, at large offset in either velocity or position.

These four subsets are shown as individual panels in Figure 22, with the columns separating BCGs with higher (left) or lower (right) than average  $\alpha$ , given  $M_m$ , and the rows corresponding to the two luminosity bins, with the brightest BCGs plotted in the top row. In any panel, we additionally note (red symbols) BCGs with  $\alpha$  residuals in excess of the rms residual,  $\sigma_\alpha$  about the mean relation;  $\sigma_\alpha = 0.13$  for the full BCG sample.

Examination of the individual panels suggests that  $r_x$  and  $|\Delta V_1|/\sigma_c$  indeed both work together to moderate the structure of the BCGs. The upper left panel in Figure 22 contains the most luminous ( $M_m < -23.0$ ) and extended BCGs. There are no BCGs with  $|\Delta V_1|/\sigma_c > 0.7$ , and the BCGs with  $\Delta\alpha > \sigma_\alpha$ , have  $|\Delta V_1|/\sigma_c < 0.3$ , or peculiar velocities less than half of those of the BCGs in this luminosity range with  $0 < \Delta\alpha < \sigma_\alpha$ . Moreover, these large  $\Delta\alpha$  galaxies have  $r_x < 100$  kpc, while the BCGs with  $0 < \Delta\alpha < \sigma_\alpha$  can have  $r_x$  an order of magnitude larger.

The galaxies in the upper right panel of Figure 22 are just as luminous as the BCGs in the panel to their left, however this subset now has three galaxies with  $|\Delta V_1|/\sigma_c > 0.7$ , and a paucity of galaxies with  $r_x < 10$  kpc. The three galaxies with  $\Delta\alpha < -\sigma_\alpha$  have  $r_x$  an order of magnitude larger than those with  $\sigma_\alpha < \Delta\alpha < 0$ .

BCGs in the  $-23.0 < M_m < -22.5$  luminosity bin largely echo the behavior exhibited by the more luminous BCGs, although the BCGs with  $\Delta\alpha > \sigma_\alpha$  have  $|\Delta V_1|/\sigma_c$  about twice as large. The BCGs in this luminosity range with  $\Delta\alpha < \sigma_\alpha$  (right-middle panel) avoid the centers of their clusters even more, however, with no galaxies having  $r_x < 50$  kpc. The BCGs with  $\Delta\alpha < -\sigma_\alpha$  have  $r_x$  an order of magnitude yet larger.

The overall picture, again, is that  $\alpha$  is larger for the BCGs that lie closer to the spatial and velocity center

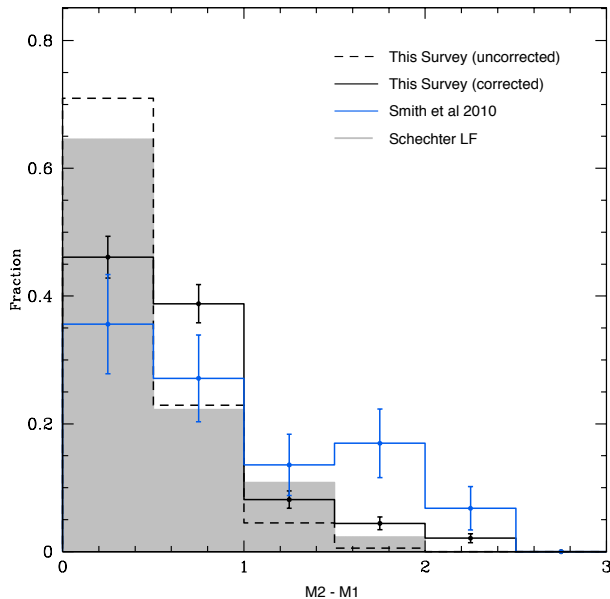


**Figure 24.** The distribution of  $M_2 - M_1$  for various cluster samples. The dashed black histogram shows the  $M_m(M_2) - M_m(\text{BCG})$  distribution for the 179 clusters for which we directly observed both the BCG and the second-ranked galaxy.  $M_m(M_2)$  and  $M_m(\text{BCG})$  are the metric luminosities of the M2 galaxy and the BCG, respectively. The solid black line shows this distribution corrected using a reference set of 30 clusters with  $M_m(M_2) - M_m(\text{BCG})$  derived from the SDSS. These 30 clusters were selected at random from amongst the clusters that we did not directly observe the second-ranked galaxy. The solid blue histogram shows the  $M_2 - M_1$  distribution from the study done by Smith et al. (2010). The light grey shaded histogram shows the expected  $M_2 - M_1$  distribution for 2000 simulated clusters with galaxy luminosities drawn from a Schechter luminosity function.

of their hosting clusters. BCGs with  $r_x < 10$  kpc and  $|\Delta V_1|/\sigma_c < 0.5$  are highly likely to have markedly higher  $\alpha$ , with  $\Delta\alpha > \sigma_\alpha$  as compared to BCGs of the same luminosity. Conversely, galaxies with  $|\Delta V_1|/\sigma_c > 1$  always have large  $r_x$  and  $\Delta\alpha < 0$ . It is striking that the BCGs with  $r_x \sim 50$  kpc have larger  $\alpha$  than do BCGs at larger distances from the center — these galaxies are still well displaced from the X-ray center, but yet are deep enough within the potential such that  $\alpha$  has already been affected. Conversely, position within the cluster seems to have little effect on  $L_m$ , as we already saw in Figures 20 and 21.

While  $\alpha$  is dependent on the spatial and velocity locations of the BCGs within the cluster, the metric plane scatter seems to be independent of both. Figure 23 shows the residuals of the metric plane (equation 13) as a function of  $|\Delta V_1|/\sigma_c$  (upper panel), and for those objects with X-ray data, as a function of  $r_x$  (lower panel). There is no evidence for a bias or increased scatter for objects with large offsets. The metric plane thus again implicitly accounts for the environmental effects of the clusters, regardless of whether the BCGs reside in the center of the cluster or in its outskirts.

## 5. THE NATURE OF SECOND-RANKED GALAXIES

### 5.1. The Photometric Properties of M2

We imaged the second-ranked galaxies, M2, in  $\sim 41\%$  of the clusters in the total sample. As we described in §2.2.1, we did this mainly when the identity of the BCG

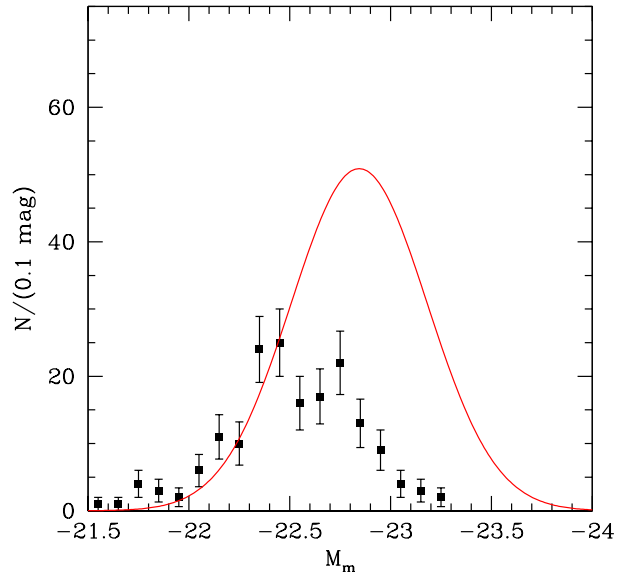


**Figure 25.** This figure shows the distribution of the metric luminosities of the observed M2 sample. The red line is the Gaussian fitted to the BCG luminosity function shown in Figure 13.

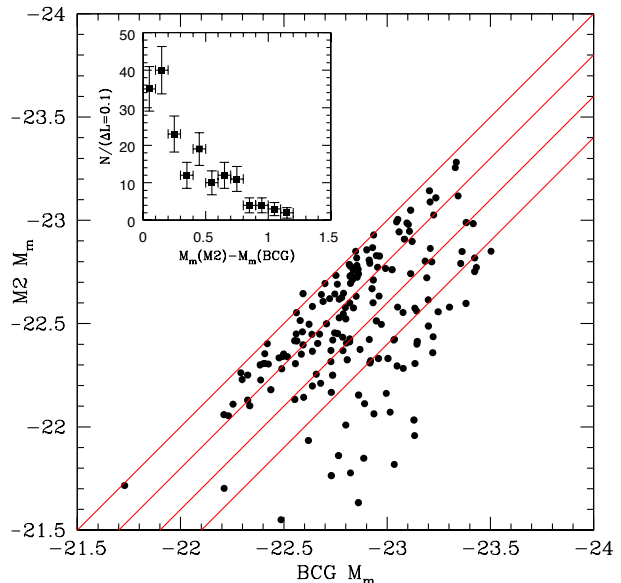


**Figure 26.** The distribution of  $M_m(\text{BCG})$  versus  $M_m(\text{M2})$ , the metric luminosities of the BCG and M2 galaxies, respectively, is plotted for the clusters with M2 observations (41% of the total sample). The upper red line marks  $M_m(\text{BCG}) = M_m(\text{M2})$ , with the subsequent lines marking offsets of  $M_m(\text{M2})$  from  $M_m(\text{BCG})$  in 0.2 mag steps. The inset figure gives the histogram of the difference in metric magnitude between the BCG and M2 in finer bins than shown in Figure 24. This is equivalent to binning along the red lines in the main figure. (The one M2 above the line is that in A3531, where the BCG becomes the brightest galaxy in an aperture slightly larger than the nominal  $r_m$ .)

during the initial definition of the sample was ambiguous, thus we are less likely to have data on M2 in cases where the BCG is *dominant*, i.e., considerably brighter than M2. We assess how strongly our observational procedures bias our derived  $M_m(\text{M2}) - M_m(\text{BCG})$  distribution by randomly selecting 30 clusters in our 15K sample for which we did not observe the second-rank galaxy. Here,



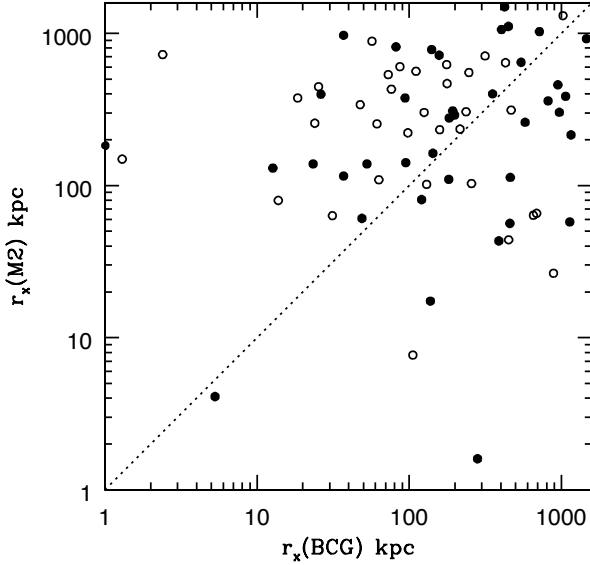


**Figure 27.** The projected offsets of M2 from the cluster X-ray centers are plotted against those of the BCG. Solid symbols are clusters for which  $M_m(\text{M2}) - M_m(\text{BCG}) < 0.3$  mag, while open symbols mark clusters with relatively less luminous M2s. Note that when  $r_x(\text{BCG}) > 100$  kpc there are only three clusters with a “rival” M2 with  $r_x(\text{M2}) < 50$  kpc. Clusters with large  $r_x(\text{BCG})$  thus do not correspond to those with small  $r_x(\text{M2})$ . The cluster in the figure with the smallest  $r_x(\text{M2})$  is A0539. Its BCG has a large peculiar velocity and a smaller  $\alpha$  than its M2, but the BCG is brighter than M2 for all aperture radii.

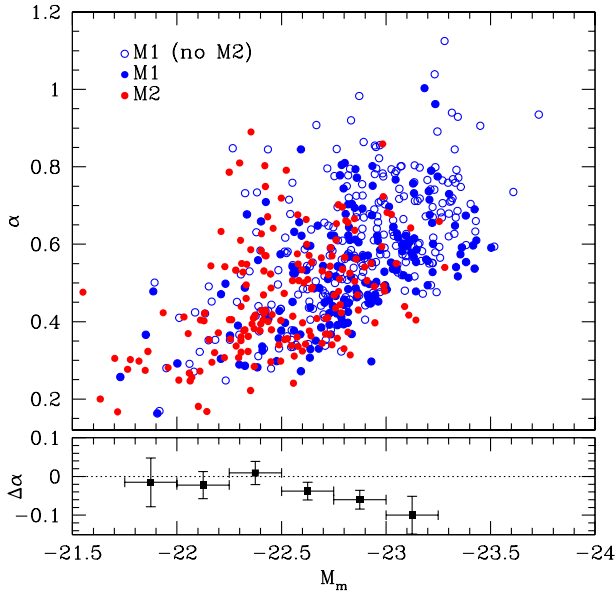


**Figure 28.** The correlation between  $\alpha$  and  $M_m$  for BCGs (blue; open symbols are BCGs in clusters lacking observed M2s) and M2s (red);  $M_m$  is now shown as the independent variable. The mean difference between the BCGs and M2  $\alpha$  in each 0.25 mag bin in  $M_m$  is plotted at the bottom. For  $M_m > -22.5$ , no difference is seen between the two populations, while the M2 have increasingly smaller average  $\alpha$  than the BCGs as  $M_m$  increases in luminosity over  $M_m < -22.5$ .

$M_m(\text{M2})$  and  $M_m(\text{BCG})$  are the metric luminosities of the M2 galaxy and the BCG, respectively. For these 30 clusters, we used the Sloan Digital Sky Survey (SDSS) r-band images to derive  $M_m(\text{M2}) - M_m(\text{BCG})$  using the

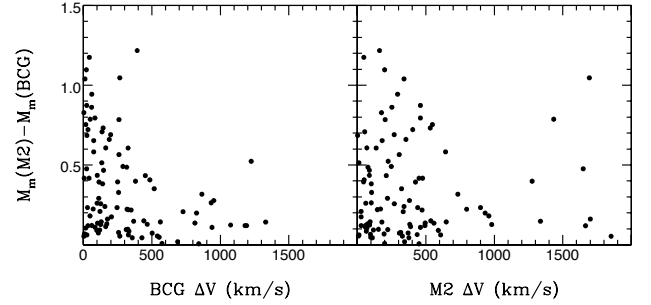


**Figure 29.** The left panel shows the M2-BCG luminosity difference as function of the absolute peculiar radial velocity of the BCG within the cluster. In the right panel the luminosity difference is plotted with respect to the peculiar velocity of M2. Only clusters with 25 members or more are plotted. Note that  $M_m(\text{M2}) - M_m(\text{BCG}) < 0.5$  for nearly all clusters in which the BCG  $\Delta V_1 > 400 \text{ km s}^{-1}$ .

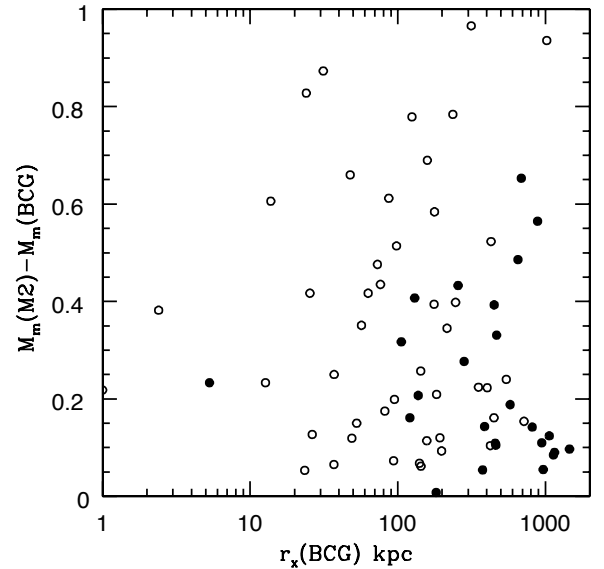


**Figure 30.** The luminosity difference between M2 and their matching BCG,  $M_m(\text{M2}) - M_m(\text{BCG})$  is plotted as a function of the offset of the BCG from the X-ray center. Solid symbols are clusters for which the M2 falls closer than the BCG to the X-ray center, while open symbols mark the opposite case. There is no relationship between the luminosity of M2 and the BCG until  $r_x < 20$  kpc, where no M2s with  $M_m(\text{M2}) - M_m(\text{BCG}) < 0.2$  mag are seen. This figure ratifies the impression from Figure 27 that there are very few clusters with M2 closer to the X-ray center once the BCG  $r_x < 100$  kpc.

same photometric techniques as described in §2.3.2. Under the assumption that this randomly selected sample of 30 clusters is representative of the clusters for which we did not initially observe the second-ranked galaxy, we derive a corrected  $M_m(\text{M2}) - M_m(\text{BCG})$  distribution by drawing  $M_m(\text{M2}) - M_m(\text{BCG})$  values from the SDSS sample for the remaining  $\sim 59\%$  of the clusters in our sample. The results are shown in Figure 24. The clusters for which we did observe M2 in our survey have a  $M_m(\text{M2}) - M_m(\text{BCG})$  distribution that is peaked at lower values than the corrected  $M_m(\text{M2}) - M_m(\text{BCG})$  distribution. We show, for comparison, the  $M_2 - M_1$  distribution from Smith et al. (2010) and from galaxies drawn from 2000 realizations of clusters with a Schechter

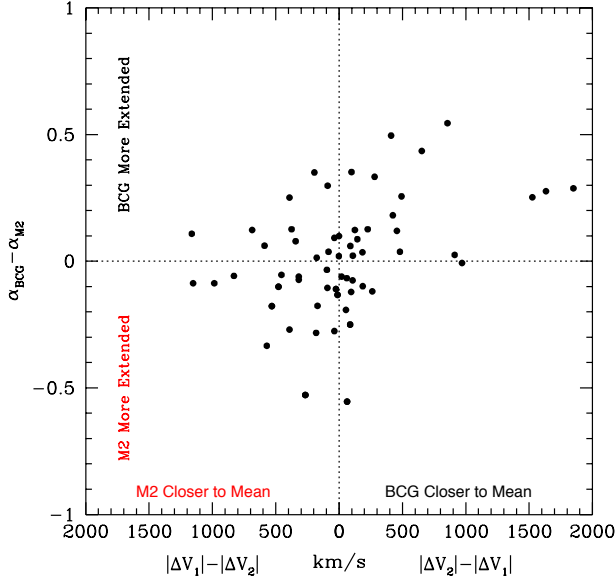


**Figure 31.** The difference in  $\alpha$  between the BCG and M2 in a given cluster is plotted as a function of the difference between the absolute values of their peculiar velocities relative to the mean cluster velocity, for M2 galaxies with  $M_m(\text{M2}) - M_m(\text{BCG}) < 0.3$  mag and clusters having 25 or more galaxy velocities. When the M2 falls closer to the mean velocity, typically  $\alpha_2 > \alpha_1$ , while the opposite is true when the BCG is the galaxy closer to the mean velocity.

(1976) luminosity function. A KS test rejects consistency between our corrected  $M_m(\text{M2}) - M_m(\text{BCG})$  distribution and that from the Smith et al. (2010) study at the 99% confidence level. Our selection procedure clearly introduces a significant bias that cannot be completely compensated for. However, the Smith et al. (2010) clusters are an X-ray selected sample, and thus may favor more luminous BCGs; their corresponding M2s may thus follow a different luminosity-offset distribution from ours as well. While this rules out performing analyses that require a complete distribution of  $M_m(\text{BCG})$  vs.  $M_m(\text{M2})$ , we can, however, compare the structure of the BCG and M2 on a per-cluster basis. It also appears that our M2 sample is close to complete for  $M_m(\text{M2}) - M_m(\text{BCG}) \leq 0.3$  mag.

Figure 25 shows the distribution of the metric absolute magnitude,  $M_m$ , of the present M2 sample compared to the Gaussian representation of the BCG luminosity function shown in Figure 13.<sup>11</sup> Interestingly, the largest differences between the M2 and BCG distributions are seen at the bright end, rather than the fainter end, where one might expect the selection effects to be the most severe. There are few highly luminous M2s, despite a deliberate effort to include such galaxies in the sample. For example, while there are 139 BCGs that have  $M_m < -23$ , there are only nine M2s that exceed this threshold.

### 5.2. The Relationship of M2 versus the BCG in the Hosting Cluster

Figure 26 plots the BCG versus M2 luminosities for each cluster, as well as a histogram of the difference in the metric magnitude between the BCG and M2 in finer

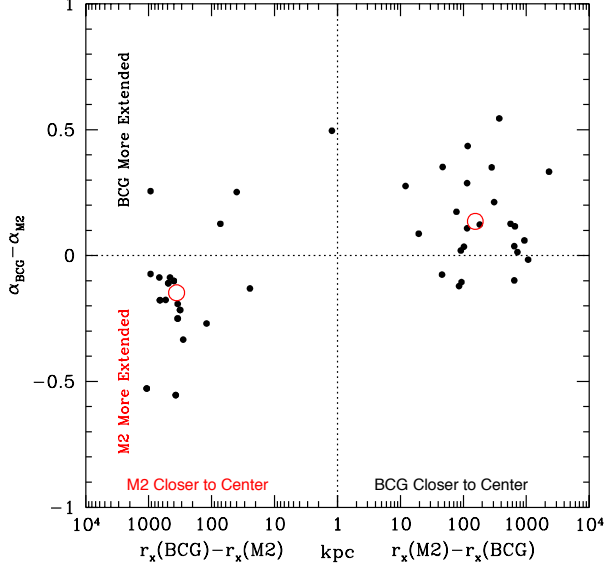
bins than shown in Figure 24. In the majority of cases, the M2 systems imaged are within a few tenths of a magnitude of the BCGs. Indeed, the M2 in any given cluster may be more luminous than many of the BCGs in other clusters. We observed M2s in 54 of the 139 clusters with BCGs with  $M_m \leq -23$ , or 39% of the systems, a fraction essentially identical to that for all clusters. At the same time, only 17/54 or  $\sim 30\%$  of this subset have M2s within 0.3 mag of the BCG  $M_m$ , a level at which we consider the M2 to be a close “rival” of the BCG, while 60/98 or  $\sim 60\%$  of the BCGs with M2s observed and  $-23 < M_m \leq -22.5$  have an M2 that is a close rival. The difference between the two subsets is readily evident in Figure 26. This result is consistent with the classic result from Sandage & Hardy (1973) that the most luminous BCGs are associated with relatively faint M2s. The large luminosity differences between the BCG and M2 for the brightest BCGs are also consistent with the arguments of Tremaine & Richstone (1977), Loh & Strauss (2006), and Lin et al. (2010) that these galaxies are “special” and are not drawn from a standard luminosity function.

Figure 27 shows that the projected offsets of the BCGs and their corresponding M2s from the X-ray center of their clusters follow different distributions. There are essentially no M2s closer to the X-ray center than the BCG once  $r_x(\text{BCG}) < 100$  kpc. Even when  $r_x(\text{BCG}) > 100$  kpc, there are only a handful of M2s with  $r_x(\text{M2}) < 50$  kpc; of these there are only three M2s with luminosities within 0.3 mag of their BCGs. In short, even though we have searched for and selected BCGs at large distances from the X-ray centers of their clusters, we are not overlooking a large population of bright “central” galaxies that might plausibly be better choices for the dominant galaxy in the cluster.

There are other ways in which the population of M2 galaxies differs from that of the BCGs besides just being less luminous. Figure 28 compares the  $L_m - \alpha$  properties of the two sets. In this case, we plot  $M_m$  as the independent variable, instead of assigning this role to  $\alpha$  as we did in §4.2. Intriguingly, this figure echoes the conclusion suggested by Figures 25 and 26 that the differences between M2 and the BCGs are most important for the brightest BCGs. For  $M_m > -22.75$ , the M2 and BCG galaxies have essentially indistinguishable distributions of  $\alpha$  as a function of  $M_m$ . It’s also worth noting that given the large scatter in the  $L_m - \alpha$  relation, many of the M2s may actually have larger  $\alpha$  values than do their corresponding BCGs. For  $M_m < -23$ , however, while the mean  $\alpha$  continues to increase for BCGs, it does not for the M2s. The few M2s with  $M_m < -23$  have significantly lower  $\alpha$  on average than the corresponding set of BCGs. Considering the results from both the previous and following sections, this implies that the bright M2s are galaxies that are not likely to be close to the X-ray center of their clusters. Bright M2s with more “normal”  $\alpha$  would be more centrally located, and thus vulnerable to merging with the BCG. The median  $r_x$  for M2 with  $M_m \leq -22.5$  is 327 kpc, indeed showing that the brightest M2s are most likely to be found markedly displaced from the center of the cluster.

Additional insight into the differences between M2 and the BCG comes from considering their relative velocity and spatial displacements within their clusters. Figure 29 plots luminosity difference between M2 and the BCG,

<sup>11</sup> All the M2 parameters plotted in the figures in this section are provided in Table 8.



**Figure 32.** The difference in  $\alpha$  between the BCG and M2 in a given cluster is plotted as a function of the difference between their radial offsets from the X-ray center in clusters where  $M_m(\text{M2}) - M_m(\text{BCG}) < 0.3$  mag. The left half of the graph plots clusters in which the BCG is further from the X-ray center than the M2 galaxy, while the right side plots clusters in which M2 is further away. The red circle indicates the mean  $\Delta\alpha$  for each half of the figure. When M2 and the BCG are close in luminosity the galaxy closest to the X-ray center is most likely to have the larger  $\alpha$ .

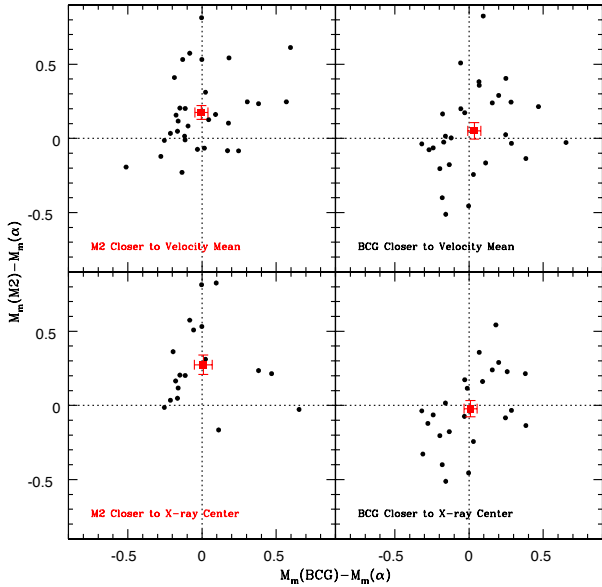


**Figure 33.** The luminosity residuals of the BCGs from the  $L_m - \alpha$  relation (equation 8) are plotted against those of M2 for clusters in which  $M_m(\text{M2}) - M_m(\text{BCG}) < 0.3$  mag. This set of clusters is further divided into four subsets depending on whether the BCG or M2 is closer to the mean cluster velocity or X-ray center. The red symbol in each panel shows the mean BCG and M2 luminosity residuals. When M2 is further from the velocity or X-ray center it appears to follow the  $L_m - \alpha$  relation. M2s closer to the center, however, are significantly dimmer than predicted by the  $L_m - \alpha$  relation, given their large  $\alpha$  values but lower metric luminosities.

$M_m(\text{M2}) - M_m(\text{BCG})$  as a function of either the peculiar velocity of the BCG with the cluster (left panel) or that

of M2 (right panel) for clusters with 25 or more members (so as to minimize the contribution of the error in the mean redshift to the peculiar velocities). It is striking that  $M_m(\text{M2}) - M_m(\text{BCG}) < 0.5$  mag for nearly all clusters in which the BCG  $\Delta V_1 > 400$  km s $^{-1}$ . This suggests a picture in which the BCGs with high peculiar velocities are relatively recent additions to the cluster that have not had enough time to undergo the relaxation interactions that would move them closer to the cluster velocity centroid. In this case the M2 is likely to be the “former BCG,” reflecting its rank prior to the infall of a more luminous galaxy. However, a fraction of these M2s will ultimately merge with the “new” BCG once the latter’s peculiar velocity has been reduced enough to make merging interactions possible. The “new” M2 will be less luminous than the old M2 that merged with the BCG, thus increasing the BCG-M2 luminosity difference for that cluster.

The effect of the BCG on M2 is also visible when  $M_m(\text{M2}) - M_m(\text{BCG})$  is plotted as function of the BCG X-ray offset (Figure 30). The main signature is that there are no M2s with  $M_m(\text{M2}) - M_m(\text{BCG}) < 0.2$  mag once the BCG gets within 20 kpc of the X-ray center. Conversely, there appears to be no relationship between  $M_m(\text{M2}) - M_m(\text{BCG})$  and  $r_x$  for BCGs falling outside this radius. The figure also ratifies the conclusion discussed in the context of Figure 27 that there are essentially no M2s closer to the center than the BCG once  $r_x(\text{BCG}) < 100$  kpc.

The structure of M2 also appears to be affected by its proximity to the mean velocity of its hosting cluster, as is the case for the BCGs. Figure 31 compares  $\alpha$  between the BCG and M2 in clusters (with 25 or more galaxy velocities) in which M2 is a close rival of the BCG ( $M_m(\text{M2}) - M_m(\text{BCG}) < 0.3$  mag). On average, the M2s should have smaller  $\alpha$ , given their smaller  $L_m$ ; however, the figure shows that this is clearly over-ridden by the effect of the proximity of the galaxies to the velocity centroid of the cluster. The M2s have slightly *larger*  $\alpha$  when  $|\Delta V_2| < |\Delta V_1|$ , that is when M2 has the smaller peculiar velocity, while the BCGs nearly always have large  $\alpha$  when the situation is reversed. The  $\alpha$  differences are not symmetrical with the difference in absolute peculiar velocities, given the initial bias for the BCGs to have higher  $\alpha$ , but the effect is clear. The processes that increase  $\alpha$  as the BCG approaches the center of the cluster are also in play for M2.

Likewise, when  $M_m(\text{M2}) - M_m(\text{BCG}) < 0.3$  mag, the galaxy of the two that is closest to the X-ray center of the cluster is more likely to have the higher  $\alpha$ . Figure 32 plots the difference in  $\alpha$  between the BCG and M2 as function of the difference between each galaxy’s offset from the X-ray center. For the 24 clusters with  $M_m(\text{M2}) - M_m(\text{BCG}) < 0.3$  (and X-ray positions available) and the BCG closer to the X-ray center than M2 (right half of the figure),  $\alpha(\text{M2}) - \alpha(\text{BCG}) = -0.14 \pm 0.4$ . When M2 is closer to the center (left half of the figure), the situation is reversed, with  $\alpha(\text{M2}) - \alpha(\text{BCG}) = +0.15 \pm 0.5$  for the 17 clusters in this subset.

The finding that rival M2s have larger  $\alpha$  than their corresponding BCGs despite their smaller metric luminosities when closer to the X-ray or velocity centers can the BCGs implies that they will strongly deviate from

the  $L_m - \alpha$  relation. This is shown in Figure 33, which plots the BCG versus M2 luminosity residuals from the  $L_m - \alpha$  relation (equation 8) for clusters in which the BCG has  $M_m(\text{M2}) - M_m(\text{BCG}) < 0.3$  mag. The set of clusters is divided into four subsets depending on which of the BCG or M2 is closer to the velocity or X-ray center. When the M2 is further from either center, both the M2 and BCG luminosity residuals average to zero, showing that the M2s act as essentially lower-luminosity BCGs. Interestingly, the residuals of both galaxies appear to be correlated for this subset. When M2 is closer to either the velocity or X-ray center, however,  $M_m(\text{M2})$  is significantly dimmer than predicted from their large  $\alpha$  values. M2s closer to the cluster center than their matching BCGs cannot be simply considered to be less luminous examples of a BCG.

## 6. THE PRESENT STRUCTURE OF BCGS AS A REFLECTION OF THEIR ORIGIN

The initial motivation of this work was to define a BCG sample to extend our earlier studies of deviations from the smooth Hubble flow (Lauer & Postman 1992, 1994) from the 15K velocity limit to 24K. As such, a large portion of this paper was concerned with revisiting the complete definition of the sample, including selection of the galaxy clusters, selection of the BCG, measurement of the photometry, spectroscopy, and so on. Compared to the LP94 sample, the present increase in limiting redshift leads to a substantial increase in sample size; the 15K sample included 119 BCGs, while the 24K sample comprises 433 galaxies. Apart from its present use to elucidate the present structure of BCGs, the sample represents a substantial, full-sky collection of precise BCG photometry, BCG central stellar velocity dispersions, cluster redshifts, and cluster velocity dispersions for nearby galaxy clusters, all of which can be used for many other investigations. We return to the questions posed in the Introduction, and finish with an attempt to integrate these results into an improved picture of the origin and evolution of BCGs.

### 6.1. What Are the Properties of BCGs?

The initial survey of BCG photometric parameters shows essentially identical results to those presented in PL95. The distribution of  $M_m$  is Gaussian with a dispersion of 0.337 mags, and the  $L_m - \alpha$  relation has scatter of 0.267 mag in the CMB frame. We now also offer a form that predicts  $M_m$  from a linear relationship in  $\log \alpha$ , rather than the quadratic form of PL95, due to its monotonic behavior with  $\alpha$ ; it also provides an acceptable fit to the data. It is notable that the random scatter in  $M_m$  has not been reduced from that presented in PL95, despite new photometry obtained for most of the 15K BCGs, and improved cluster velocities.

The present work goes beyond PL95 by including central stellar velocity-dispersion observations of the BCGs. Use of metric luminosities obtained in different aperture sizes allows us to track the flattening of the Faber & Jackson (1976) relationship between  $L$  and  $\sigma$  as the aperture grows to include a larger fraction of the total galaxy luminosity. The relationship between  $L_m$  and  $\sigma$  using our standard 14.3 kpc metric radius resembles the classic  $\sigma \propto L^{1/4}$  relation, while increasing  $r_m$  4 $\times$  larger to 57.1 kpc yields a much shallower  $\sigma \propto L^{1/6}$  relation. The

flatter Faber-Jackson relation for BCGs has been discussed extensively in the literature, but this shows that it is likely a consequence of the extremely large envelopes of the BCGs.

The residuals of the  $L_m - \alpha$  relationship correlate strongly with  $\sigma$ , thus motivating the development of a three-parameter “metric plane” relationship between  $L_m$ ,  $\alpha$ , and  $\sigma$  analogous to the “fundamental plane” relations. Use of  $\alpha$  and  $\sigma$  together predicts  $M_m$  to a precision of 0.206 mag, a substantial improvement over the  $L_m - \alpha$  relationship. The metric plane relation also implicitly removes correlations between the residuals of the  $L_m - \alpha$  relation and the cluster velocity dispersion.

### 6.2. Where Are the BCGs Located in Their Galaxy Clusters?

A first step in understanding the relationship of BCGs to their galaxy clusters is to ask where they are located in the clusters. In answering this question we have produced quantitative distribution functions for both the projected spatial and peculiar velocities of the BCGs with the cluster, where the spatial offset is defined with respect to the cluster X-ray center, and the velocity with respect to the mean cluster velocity. The spatial offset,  $r_x$  follows a steep power-law with  $\gamma = -2.33$  over three decades in radius; there is no evidence for any core at scales  $> 10$  kpc.

The absolute normalized peculiar velocities  $|\Delta V_1|/\sigma_c$  of BCGs within their clusters follows an exponential distribution, with scale length 0.39. The spatial and velocity offsets are correlated. Large  $|\Delta V_1|/\sigma_c$  always corresponds to large  $r_x$  and small  $r_x$  always corresponds to small  $|\Delta V_1|/\sigma_c$ .

These results raise an important caveat in understanding the relation between the BCGs and their hosting clusters. While BCGs do prefer to reside near the central regions of galaxy clusters, BCGs with  $r_x > 100$  kpc or  $|\Delta V_1|/\sigma_c > 0.5$  are common. These outlying BCGs further follow the same metric plane as do those closer to the center of their parent clusters. This has important consequences for understanding the relationship between “intercluster light” (ICL) and the extended envelopes of BCGs. BCGs are often simplistically assumed to *always* reside at both the spatial and velocity center of ICL, such that it becomes ambiguous as to where the BCG ends and the ICL picks up (see the discussion in Lauer et al. 2007). While this may be true in some cases, it will not be true in general.

Our BCGs are defined by metric luminosity, while some authors choose the brightest galaxy close to the X-ray center, even if it turns out to be the M2. The latter definition would risk the possibility of missing BCG that are still being accreted by rich galaxy clusters at the present epoch. There is no question that there are first-ranked galaxies in many clusters that are offset by large velocities and projected separations for the X-ray defined centers. These are most easily understood as recently accreted additions to the cluster. The identity of the galaxy that occupies the first-ranked position will change as new galaxies are brought in, and may have changed a number of times in a given cluster over cosmological history, as is found in the simulations of De Lucia & Blaizot (2007) and Martel et al. (2014).

### 6.3. How Does the Cluster Environment Influence the Properties of the BCGs?

The relationships that we have observed between the properties of the BCGs and their clusters support the picture that the bulk of any given BCG is largely assembled outside of the cluster, before the galaxy is accreted by the cluster. The strongest effect is that  $\alpha$  is clearly moderated by both  $r_x$  and  $|\Delta V_1|/\sigma_c$ , such that  $\alpha$  increases monotonically as the BCG lies closer and closer to the center of the cluster. BCGs with the largest  $\alpha$  for their  $L_m$  always reside close to the X-ray and velocity center of the cluster. Conversely, BCGs with the smallest  $\alpha$  given  $L_m$  are strongly displaced from the center, often with  $r_x \gg 100$  kpc and  $|\Delta V_1|/\sigma_c > 0.5$ . However,  $L_m$  is only weakly, if at all, related to the position of the BCG within the cluster.

We conclude that the envelopes of the BCGs are expanded by and perhaps even grown by interactions that become increasingly important as the BCG spends the majority of the time in ever denser regions of the clusters and dynamical relaxation reduces its peculiar velocity. The fact that  $L_m$  does not vary with spatial or velocity offset from the center of the cluster argues that the denser central body of the BCG, however, is less affected the same processes. Some BCGs, even at low redshifts, have been recently accreted into the outskirts of the clusters. Even though they may not have the classic extended envelopes associated with, say, massive cD galaxies, their  $L_m$  is already high enough that they can claim first rank over all other galaxies within the cluster.

It is here that the properties of the M2 galaxies are important. When M2 is close in luminosity to the BCG, we see that which of the BCG or M2 has higher  $\alpha$  depends on which is closer to the mean cluster velocity or the center of the cluster potential as marked by X-ray emission. Clearly, the processes that act on the BCG as a function of its location in the cluster also act on M2. In fact, the luminosity differences between the two sets of galaxies reveal the nature of the competition for first rank. While our sample of M2 is incomplete, we only see large luminosity differences between them when  $|\Delta V_1|$  is relatively small. We hypothesize that when the BCG initially enters the cluster with a high  $|\Delta V_1|$ , the previous BCG, now demoted to M2, can still survive as a close rival until the BCG undergoes enough interactions to be captured into the central potential of the cluster. Conversely, when it is the M2 that has a high peculiar velocity or has an orbit that keeps it mainly in the outskirts of the cluster, it can persist as close rival in luminosity to the BCG.

### 6.4. A Brief History of BCGs

Throughout the narrative our results raise the question of the extent to which BCGs grow their luminosity inside versus outside of their present hosting clusters. We see that there are some BCGs with large  $L_m$ , meaning that the assembly of their stellar mass is essentially complete, but that also have large  $r_x$  and large  $|\Delta V_1|/\sigma_c$ , which means that they are relatively recent arrivals to their hosting clusters. In the clusters for which this is so, there may also be a centrally-located M2 that many would pick as the “true” BCG — certainly, that galaxy is more likely to have the greatly extended enve-

lope that’s often associated with the classical pictures of BCGs. The inference is that most of the stellar mass of any given BCG, or at least its portion within the metric radius, grew from the merger of progenitor galaxies outside the rich cluster environment. Such a scenario was suggested by Merritt (1985), who noted that the lower velocity dispersions of galaxy groups, rather than rich clusters, made them attractive as the birthplace of future BCGs. The BCG may represent the merging terminus of many of the galaxies within the group. The merged system may later be accreted by a rich cluster, but then may be subjected to only minor interactions or mergers once it arrives there. These would add energy to its envelope but little stellar mass.

On the other hand, in this study we see that BCG  $L_m$  increases markedly with  $\sigma_c$ , and as we noted earlier in the Introduction, BCG luminosity also tracks cluster X-ray luminosity and temperature. One might presume that this only reflects the likelihood that today’s rich clusters once had the richest retinue of surrounding groups, but there is evidence that major mergers can take place within clusters (Lauer 1988). The most luminous BCGs are unlikely to have strong M2 rivals for the position of first rank. Faint M2 galaxies are further uniquely associated with BCGs with modest  $|\Delta V_1|/\sigma_c$ . Whatever level of minor merging that may have taken place, this result suggests that many of the current BCGs have cannibalized their closest rivals, an event that would have been a major merger. It is also a feature of dry merging that this may cause little luminosity growth *within* the metric aperture (Hausman & Ostriker 1978; Boylan-Kolchin et al. 2006), while greatly extending the envelope. The growth in  $\alpha$  as the BCGs become more centrally located argue that this is happening.

The question of whether most BCG luminosity growth occurs inside or outside of rich clusters intersects with the issue of whether or not BCGs are “special.” Lin et al. (2010) have argued that only the BCGs in the most X-ray luminous clusters exhibit luminosities high enough such that they cannot be explained as simply being drawn from a standard cluster luminosity function. This is thus a partial contradiction of the analysis of Tremaine & Richstone (1977) that suggested that all BCGs were created by special processes. In this work we see that the M2s are most structurally similar to their corresponding BCGs when the BCGs have more modest metric luminosities. It is when  $M_m$  starts to grow beyond  $\sim -22.5$  that we begin to see their properties diverge. We conclude that if BCGs were born in relatively small groups, it is their accretion into rich clusters that later shapes and grows them to their final form and special luminosities. We will explore these themes further in follow-on papers that will elucidate the relation of the present sample of BCGs to the properties of giant elliptical galaxies and measure the on-going rate of merger interactions in BCGs.

This work is based on extensive observational work conducted at Kitt Peak National Observatory and Cerro Tololo Inter-American Observatory, both operated by the National Optical Astronomy Observatory (NOAO). We are indebted to the professional staff of NOAO for the development and operation of the telescopes and instru-

ments that we used for this project. NOAO is operated by AURA, Inc., under cooperative agreement with the National Science Foundation. We thank Beth Reid, Megan Donahue, Kayhan Gültekin, Christine Jones, and William Forman for useful conversations. We thank Katelyn Millette for a critical reading of the manuscript. This research has made use of the NASA/IPAC Extragalactic Database (NED), which is operated by the Jet Propulsion Laboratory, California Institute of Technology, under contract with the National Aeronautics and Space Administration. This paper has also made use of the data from the SDSS. Funding for the SDSS and SDSS-II has been provided by the Alfred P. Sloan Foundation, the Participating Institutions, the National Science Foundation, the U.S. Department of Energy, the National Aeronautics and Space Administration, the Japanese Monbukagakusho, the Max Planck Society, and the Higher Education Funding Council for England.

## REFERENCES

- Abazajian, K. N., Adelman-McCarthy, J. K., Agüeros, M. A., et al. 2009, *ApJS*, 182, 543
- Abell, G. O. 1958, *ApJS*, 3, 211
- Abell, G. O., Corwin, H. G., Jr., & Olowin, R. P. 1989, *ApJS*, 70, 1
- Adelman-McCarthy, J. K., Agüeros, M. A., Allam, S. S., et al. 2008, *ApJS*, 175, 297
- Allen, S. W. 1998, *MNRAS*, 296, 392
- Ascaso, B., Aguerri, J. A. L., Varela, J., et al. 2011, *ApJ*, 726, 69
- Bahcall, N., & Soniera, R. M. 1983, *ApJ*, 270, 20
- Bechtold, J., Forman, W., Jones, C., et al. 1983, *ApJ*, 265, 26
- Beers, T. C., & Geller, M. J. 1983, *ApJ*, 274, 491
- Beers, T. C., Flynn, K., & Gebhardt, K. 1990, *AJ*, 100, 32
- Bernardi, M., Hyde, J. B., Sheth, R. K., Miller, C. J., & Nichol, R. C. 2007, *AJ*, 133, 1741
- Binggeli, B. 1982, *A&A*, 107, 338
- Bolton, A. S., Schlegel, D. J., Aubourg, É., et al. 2012, *AJ*, 144, 144
- Boylan-Kolchin, M., Ma, C.-P., & Quataert, E. 2006, *MNRAS*, 369, 1081
- Brough, S., Collins, C. A., Burke, D. J., Lynam, P. D., & Mann, R. G. 2005, *MNRAS*, 364, 1354
- Burstein, D., & Heiles, C. 1982, *AJ*, 87, 1165
- Cappellari, M., & Emsellem, E. 2004, *PASP*, 116, 138
- Carlberg, R. G., Yee, H. K. C., & Ellingson, E. 1997, *ApJ*, 478, 462
- Cavagnolo, K. W., Donahue, M., Voit, G. M., & Sun, M. 2009, *ApJS*, 182, 12
- Chisari, N. E., Lauer, T. R., Postman, M., Strauss, M. A., & Graves, G. J. 2014, in preparation.
- Collins, C. A., & Mann, R. G. 1998, *MNRAS*, 297, 128
- Coziol, R., Andernach, H., Caretta, C. A., Alamo-Martínez, K. A., & Tago, E. 2009, *AJ*, 137, 4795
- De Lucia, G., & Blaizot, J. 2007, *MNRAS*, 375, 2
- Diaferio, A., & Geller, M. J. 1996, *ApJ*, 467, 19
- Djorgovski, S., & Davis, M. 1987, *ApJ*, 313, 59
- Dressler, A., Lynden-Bell, D., Burstein, D., et al. 1987, *ApJ*, 313, 42
- Ebeling, H., Voges, W., Bohringer, H., et al. 1996, *MNRAS*, 281, 799
- Edge, A. C. 1991, *MNRAS*, 250, 103
- Edge, A. C., & Stewart, G. C. 1991, *MNRAS*, 252, 414
- Faber, S. M., & Jackson, R. E. 1976, *ApJ*, 204, 668
- Finkbeiner, D. P., Davis, M., & Schlegel, D. J. 1999, *ApJ*, 524, 867
- Fisher, K. B., Davis, M., Strauss, M. A., Yahil, A., & Huchra, J. P. 1994, *MNRAS*, 267, 927
- Geller, M. J., & Postman, M. 1983, *ApJ*, 274, 31.
- Graves, G. J., Faber, S. M., Schiavon, R. P., & Yan, R. 2007, *ApJ*, 671, 243
- Greene, J. E., Murphy, J. D., Graves, G. J., Gunn, J. E., Raskutti, S., Comerford, J. M., & Gebhardt, K. 2013, *ApJ*, 776, 64
- Gunn, J. E., & Oke, J. B. 1975, *ApJ*, 195, 255
- Haarsma, D. B., Leisman, L., Donahue, M., et al. 2010, *ApJ*, 713, 1037
- Hao, J., Kubo, J. M., Feldmann, R., et al. 2011, *ApJ*, 740, 39
- Hashimoto, Y., Henry, J. P., & Boehringer, H. 2014, *MNRAS*, 440, 588
- Hausman, M. A., & Ostriker, J. P. 1978, *ApJ*, 224, 320
- Hogg, D. W., Bovy, J., & Lang, D. 2010, arXiv:1008.4686
- Hudson, D. S., Mittal, R., Reiprich, T. H., et al. 2010, *A&A*, 513, A37
- Hudson, M. J., & Ebeling, H. 1997, *ApJ*, 479, 621
- Humason, M. L., Mayall, N. U., & Sandage, A. R. 1956, *AJ*, 61, 97
- Hoessel, J. G. 1980, *ApJ*, 241, 493
- Hopkins, P. F., Bundy, K., Murray, N., et al. 2009, *MNRAS*, 398, 898
- Jones, C., & Forman, W. 1984, *ApJ*, 276, 38
- Juzskiewicz, R., Fisher, K. B., & Szapudi, I. 1998, *ApJ*, 504, L1
- Kelly, B. C. 2011, arXiv:1112.1745
- Lambas, D. G., Groth, E. J., & Peebles, P. J. E. 1988, *AJ*, 95, 996
- Landolt, A. U. 1983, *AJ*, 88, 439
- Lauer, T. R. 1986, *ApJ*, 311, 34
- Lauer, T. R. 1988, *ApJ*, 325, 49
- Lauer, T. R., Faber, S. M., Richstone, D., et al. 2007, *ApJ*, 662, 808
- Lauer, T. R., & Postman, M. 1992, *ApJ*, 400, L47
- Lauer, T. R., & Postman, M. 1994, *ApJ*, 425, 418
- Ledlow, M. J., Voges, W., Owen, F. N., & Burns, J. O. 2003, *AJ*, 126, 2740
- Lin, Y.-T., Ostriker, J. P., & Miller, C. J. 2010, *ApJ*, 715, 1486
- Liu, F. S., Xia, X. Y., Mao, S., Wu, H., & Deng, Z. G. 2008, *MNRAS*, 385, 23
- Loh, Y.-S., & Strauss, M. A. 2006, *MNRAS*, 366, 373
- Mahdavi, A., & Geller, M. J. 2001, *ApJ*, 554, L129
- Malumuth, E. M. 1992, *ApJ*, 386, 420
- Martel, H., Robichaud, F., & Barai, P. 2014, *ApJ*, 786, 79
- Marzke, R. O., Geller, M. J., da Costa, L. N., & Huchra, J. P. 1995, *AJ*, 110, 477
- Merritt, D. 1985, *ApJ*, 289, 18
- Miller, C. J., Nichol, R. C., Reichart, D., et al. 2005, *AJ*, 130, 968
- Newman, A. B., Treu, T., Ellis, R. S., & Sand, D. J. 2011, *ApJ*, 728, L39
- Niederste-Ostholt, M., Strauss, M. A., Dong, F., Koester, B. P., & McKay, T. A. 2010, *MNRAS*, 405, 2023
- Oegerle, W. R., & Hill, J. M. 2001, *AJ*, 122, 2858
- Oegerle, W. R., & Hoessel, J. G. 1991, *ApJ*, 375, 15
- Ostriker, J. P., & Tremaine, S. D. 1975, *ApJ*, 202, L113
- Patel, P., Maddox, S., Pearce, F. R., Aragón-Salamanca, A., & Conway, E. 2006, *MNRAS*, 370, 851
- Postman, M., Huchra, J. P., & Geller, M. J. 1992, *ApJ*, 384, 404
- Postman, M., & Lauer, T. R. 1995, *ApJ*, 440, 28
- Postman, M., Lauer, T. R., Oegerle, W., & Donahue, M. 2002, *ApJ*, 579, 93
- Quintana, H., & Lawrie, D. G. 1982, *AJ*, 87, 1
- Quintana, H., & Melnick, J. 1982, *AJ*, 87, 972
- Reid, B. A., Seo, H.-J., Leauthaud, A., Tinker, J. L., & White, M. 2014, arXiv:1404.3742
- Sánchez-Blázquez, P., Gorgas, J., Cardiel, N., & González, J. J. 2006, *A&A*, 457, 809
- Richstone, D. O. 1975, *ApJ*, 200, 535
- Sandage, A. 1972a, *ApJ*, 173, 485
- Sandage, A. 1972b, *ApJ*, 178, 1
- Sandage, A. 1975, *ApJ*, 202, 563
- Sandage, A. 1976, *ApJ*, 205, 6
- Sandage, A., & Hardy, E. 1973, *ApJ*, 183, 743
- Sastry, G. N. 1968, *PASP*, 80, 252
- Schechter, P. 1976, *ApJ*, 203, 297
- Schlegel, D. J., Finkbeiner, D. P., & Davis, M. 1998, *ApJ*, 500, 525
- Schombert, J. M. 1988, *ApJ*, 328, 475
- Skibba, R. A., van den Bosch, F. C., Yang, X., et al. 2011, *MNRAS*, 410, 417
- Smith, G. P., Khosroshahi, H. G., Dariush, A., et al. 2010, *MNRAS*, 409, 169

Smith, G. P., Kneib, J.-P., Smail, I., et al. 2005, MNRAS, 359, 417  
 Solinger, A. B., & Tucker, W. H. 1972, ApJ, 175, L107  
 Stephens, M. 1974, J. Am. Stat. Assoc., 69, 730  
 Stott, J. P., Hickox, R. C., Edge, A. C., et al. 2012, MNRAS, 422, 2213  
 Tonry, J., & Davis, M. 1979, AJ, 84, 1511  
 Tremaine, S. D., & Richstone, D. O. 1977, ApJ, 212, 311  
 van Dokkum, P. G., Whitaker, K. E., Brammer, G., et al. 2010, ApJ, 709, 1018  
 Vazdekis, A., Sánchez-Blázquez, P., Falcón-Barroso, J., Cenarro, A. J., Beasley, M. A., Cardiel, N., Gorgas, J., & Peletier, R. F. 2010, MNRAS, 404, 1639

Voges, W., Aschenbach, B., Boller, T., et al. 1999, A&A, 349, 389  
 von der Linden, A., Best, P. N., Kauffmann, G., & White, S. D. M. 2007, MNRAS, 379, 867  
 White, S. D. M., Briel, U. G., & Henry, J. P. 1993, MNRAS, 261, L8  
 Wu, X.-P., Xue, Y.-J., & Fang, L.-Z. 1999, ApJ, 524, 22  
 Yahil, A., & Vidal, N. V. 1977, ApJ, 214, 347  
 Zabludoff, A. I., Geller, M. J., Huchra, J. P., & Ramella, M. 1993, AJ, 106, 1301  
 Zabludoff, A. I., Huchra, J. P., & Geller, M. J. 1990, ApJS, 74, 1

**Table 1**  
 The BCG and Abell Cluster Sample

Abell	$\alpha$ (2000)	$\delta$ (2000)	$V_1$ km s <sup>-1</sup>	$V_c$ km s <sup>-1</sup>	$\sigma_c$ km s <sup>-1</sup>	$N_g$	$A_B$	Notes
14	3.7957	-23.8823	19280 ± 26	19397 ± 111	474 ± 118	18	0.094	E473-G005
27	6.1965	-20.7324	15519 ± 0	16037 ± 90	339 ± 79	14	0.094	E539-G013
71	9.4947	+29.6035	22044 ± 33	22044 ± 33	...	2	0.210	
74	9.5903	-22.3449	19013 ± 46	19326 ± 56	212 ± 59	14	0.091	
75	9.8692	+21.2295	17610 ± 42	17355 ± 326	731 ± 511	5	0.146	
76	9.8597	+6.7340	11283 ± 17	11969 ± 148	491 ± 120	11	0.179	I1565 15K
77	10.1181	+29.5558	21424 ± 35	21135 ± 187	419 ± 246	5	0.190	U00428
85	10.4602	-9.3034	16581 ± 56	16622 ± 62	1009 ± 31	263	0.162	
86	10.6762	-21.7745	18481 ± 41	18887 ± 111	415 ± 72	14	0.086	
102	12.1301	+1.3547	18946 ± 37	19702 ± 166	624 ± 125	14	0.124	U00496
114	13.5312	-21.7143	17290 ± 45	17705 ± 105	515 ± 77	24	0.079	
116	13.9435	+0.6450	20100 ± 42	19992 ± 92	629 ± 80	46	0.122	
117	13.9662	-9.9857	16453 ± 47	16460 ± 63	629 ± 49	99	0.156	I1602
119	14.0672	-1.2561	13338 ± 22	13334 ± 55	901 ± 40	267	0.167	U00579 15K
133	15.6739	-21.8820	17041 ± 50	16759 ± 94	790 ± 63	70	0.080	E541-G013
134	15.6628	-2.6962	20639 ± 31	21000 ± 86	345 ± 61	16	0.190	
147	17.1579	+2.2684	13149 ± 56	13030 ± 115	621 ± 79	29	0.108	15K
150	17.3268	+13.1687	17754 ± 38	17750 ± 191	664 ± 151	12	0.122	U00716
151	17.2130	-15.4072	15936 ± 49	16011 ± 66	795 ± 59	144	0.113	I0080
152	17.5135	+13.9778	17491 ± 35	17611 ± 99	844 ± 59	72	0.154	U00727
154	17.7647	+17.6518	18236 ± 39	19115 ± 183	988 ± 146	29	0.276	I1635
158	17.9387	+16.8862	18958 ± 38	18958 ± 38	...	2	0.349	
161	18.8433	+37.3396	22185 ± 45	22185 ± 45	...	2	0.279	
168	18.7404	+0.4311	13546 ± 50	13476 ± 54	625 ± 36	133	0.149	U00797 15K
171	19.3248	+16.2652	20718 ± 45	20718 ± 45	...	2	0.466	
174	20.0677	+35.8072	22490 ± 43	22490 ± 43	...	2	0.250	
179	20.5452	+19.6205	15618 ± 39	16187 ± 127	284 ± 0	5	0.224	
189	20.8597	+1.7049	10195 ± 14	9600 ± 66	332 ± 46	25	0.142	VV 509 15K
193	21.2814	+8.6992	14664 ± 43	14529 ± 78	776 ± 62	97	0.219	I1695 15K
194	21.4952	-1.3394	5296 ± 20	5390 ± 43	495 ± 29	132	0.182	N0545 15K
195	21.7281	+19.2139	12915 ± 60	12656 ± 85	306 ± 58	13	0.236	I0115 15K
208	22.8873	+0.5558	23802 ± 41	23729 ± 76	601 ± 50	61	0.102	
225	24.7043	+18.8251	20819 ± 41	20832 ± 269	660 ± 272	6	0.249	
240	25.5252	+7.6646	18253 ± 36	18253 ± 36	...	3	0.181	U01191
245	26.0341	+6.3162	23391 ± 34	23391 ± 34	...	2	0.240	
246	26.1812	+5.8119	22691 ± 51	22617 ± 158	571 ± 138	13	0.308	
257	27.2851	+13.9629	21143 ± 42	21054 ± 72	499 ± 42	47	0.239	
260	27.6790	+33.0819	10642 ± 19	10931 ± 90	754 ± 74	70	0.210	I1733 15K
261	27.8603	-2.2532	13965 ± 21	14159 ± 69	183 ± 61	7	0.125	15K
262	28.1928	+36.1515	4813 ± 41	4860 ± 44	540 ± 38	150	0.373	N0708 15K
267	28.3134	+1.0388	17963 ± 34	17878 ± 46	296 ± 42	40	0.108	
268	28.2052	-1.0018	17917 ± 29	17925 ± 35	160 ± 88	20	0.121	
279	29.0707	+1.0507	23680 ± 34	24013 ± 78	753 ± 78	92	0.126	
292	30.5789	+19.0669	19423 ± 48	19423 ± 48	...	3	0.340	U01518
295	30.5718	-1.1279	12813 ± 56	12694 ± 49	406 ± 37	66	0.122	U01525 15K
311	32.3687	+19.7761	19580 ± 43	19580 ± 43	...	1	0.751	
326	33.4156	-7.1453	17052 ± 51	16503 ± 216	483 ± 0	5	0.126	
347	36.3603	+41.8242	5234 ± 14	5628 ± 80	627 ± 61	60	0.251	N0910 15K
357	37.3652	+13.2661	16948 ± 48	16948 ± 48	...	3	0.461	
358	37.4957	-13.2649	16951 ± 41	16855 ± 97	322 ± 232	11	0.073	
376	41.5168	+36.9046	14560 ± 36	14394 ± 72	830 ± 59	130	0.314	U02232 15K
386	42.5095	-17.0484	17835 ± 34	17835 ± 34	...	3	0.112	
397	44.1205	+15.9164	10381 ± 17	9920 ± 111	638 ± 85	33	0.650	U02413 15K
399	44.4715	+13.0305	21415 ± 49	21550 ± 110	1224 ± 62	122	0.759	U02438
400	44.4240	+6.0214	7250 ± 10	7281 ± 63	683 ± 39	116	0.779	N1128
401	44.7410	+13.5826	22215 ± 58	22045 ± 104	1161 ± 76	124	0.678	U02450
404	45.3950	+41.4873	18420 ± 34	18686 ± 101	202 ± 145	4	0.525	
407	45.4650	+35.8409	14059 ± 110	13872 ± 85	762 ± 62	80	0.843	U02489 15K
415	46.7200	-12.1063	23588 ± 53	24025 ± 192	665 ± 130	12	0.257	
423	47.8220	-12.1284	23435 ± 49	24147 ± 404	1280 ± 315	10	0.271	

Table 1 — *Continued*

Abell	$\alpha$ (2000)	$\delta$ (2000)	$V_1$ km s <sup>-1</sup>	$V_c$ km s <sup>-1</sup>	$\sigma_c$ km s <sup>-1</sup>	$N_g$	$A_B$	Notes
428	49.0522	-19.0822	19908 ± 42	20024 ± 62	317 ± 51	26	0.127	
436	51.6473	+9.1841	19061 ± 51	19061 ± 51	...	2	1.189	
450	55.2308	+23.5922	17685 ± 51	17685 ± 51	...	2	0.881	
496	68.4070	-13.2610	9839 ± 7	9899 ± 42	737 ± 29	305	0.586	15K
498	69.4616	+21.2053	17399 ± 55	17399 ± 55	...	1	1.725	
500	69.7190	-22.1110	20340 ± 48	20347 ± 80	771 ± 175	92	0.215	
505	74.9836	+80.1784	16017 ± 47	16017 ± 47	...	1	0.409	U03197
514	71.7771	-20.4811	21359 ± 49	21638 ± 129	1180 ± 69	83	0.237	
533	75.2844	-22.5828	14384 ± 28	14563 ± 119	610 ± 157	26	0.151	15K
539	79.2297	+6.5526	9690 ± 23	8710 ± 94	833 ± 40	78	0.726	15K
548	87.3406	-25.3464	11858 ± 19	12293 ± 59	795 ± 28	178	0.124	E488-G033 15K
564	105.1685	+69.9069	23188 ± 34	23188 ± 34	0 ± 70	3	0.243	
568	106.9232	+35.0582	23496 ± 48	23025 ± 259	687 ± 0	7	0.277	
569	107.2823	+48.6154	5839 ± 3	5949 ± 58	394 ± 25	45	0.307	N2329 15K
576	110.5285	+55.8748	12087 ± 21	11503 ± 76	1093 ± 37	205	0.325	15K
582	112.0035	+41.9185	17518 ± 5	17336 ± 74	324 ± 56	19	0.375	
592	115.7208	+9.2809	18697 ± 35	18846 ± 55	123 ± 0	5	0.154	
595	117.1535	+52.2220	19282 ± 36	20705 ± 85	601 ± 56	49	0.237	
600	119.1492	+63.7397	23302 ± 34	23302 ± 34	...	3	0.216	
602	118.1166	+29.5423	17784 ± 28	18137 ± 93	796 ± 61	73	0.244	
634	123.9371	+58.3211	8139 ± 13	7921 ± 38	331 ± 25	74	0.238	U04289 15K
644	124.3569	-7.5128	21176 ± 43	20982 ± 148	960 ± 114	42	0.471	
671	127.1330	+30.4300	14970 ± 120	14877 ± 75	850 ± 33	126	0.203	I2378 15K
690	129.8163	+28.8439	23750 ± 250	24045 ± 66	546 ± 46	68	0.240	
695	130.3047	+32.4161	20560 ± 84	20282 ± 80	402 ± 52	25	0.168	
744	136.8357	+16.6514	21865 ± 25	21844 ± 76	445 ± 920	34	0.150	
754	137.1347	-9.6303	16440 ± 57	16374 ± 50	995 ± 35	389	0.277	
757	138.2826	+47.7082	15415 ± 0	15410 ± 46	360 ± 32	61	0.072	
779	139.9450	+33.7496	6897 ± 1	6885 ± 39	450 ± 23	133	0.073	N2832 15K
780	139.5238	-12.0955	16286 ± 8	16356 ± 139	871 ± 112	39	0.193	
819	143.0709	+9.6831	22912 ± 95	22757 ± 96	654 ± 66	46	0.166	
834	145.3872	+66.7105	21307 ± 50	20910 ± 68	392 ± 0	33	0.602	
838	144.2860	-5.0417	15668 ± 39	15524 ± 143	477 ± 120	11	0.201	
841	144.6500	-4.3353	20838 ± 34	20838 ± 34	...	3	0.229	
912	150.2892	-0.0796	13580 ± 8	13660 ± 66	369 ± 49	31	0.158	15K
957	153.4095	-0.9254	13387 ± 19	13497 ± 70	772 ± 52	119	0.181	U05515 15K
970	154.3572	-10.6892	17496 ± 38	17682 ± 72	841 ± 75	135	0.233	
978	155.1107	-6.5270	16211 ± 29	16215 ± 87	837 ± 55	91	0.181	
979	155.0804	-7.8937	15907 ± 39	15919 ± 129	484 ± 86	14	0.214	
993	155.4832	-4.8905	16300 ± 52	16213 ± 50	513 ± 37	104	0.212	
999	155.8494	+12.8349	9750 ± 10	9621 ± 38	286 ± 25	56	0.175	15K
1003	156.2570	+47.8416	19153 ± 40	18726 ± 72	501 ± 50	48	0.049	VV 675
1016	156.7830	+11.0103	9711 ± 5	9693 ± 30	204 ± 53	45	0.137	I0613 15K
1020	156.9567	+10.4416	19611 ± 10	19598 ± 68	314 ± 41	21	0.148	
1032	157.5425	+4.0068	19823 ± 40	19990 ± 114	706 ± 47	38	0.141	
1035	158.0584	+40.2711	23951 ± 150	23524 ± 115	814 ± 79	50	0.056	
1060	159.1773	-27.5286	3858 ± 5	3714 ± 37	712 ± 25	371	0.342	N3311 15K
1066	159.9119	+5.1751	21216 ± 7	20718 ± 79	817 ± 55	105	0.110	
1069	159.9313	-8.6870	19612 ± 57	19589 ± 85	706 ± 66	69	0.175	
1090	161.4225	-18.3571	22994 ± 0	22994 ± 0	...	1	0.174	
1100	162.1905	+22.2176	13981 ± 35	13947 ± 47	451 ± 0	89	0.093	15K
1139	164.5459	+1.6043	11515 ± 20	11839 ± 37	436 ± 25	136	0.135	U06057 15K
1142	165.1891	+10.5532	10138 ± 39	10595 ± 79	757 ± 44	91	0.125	I0664 15K
1145	165.3681	+16.7680	20704 ± 100	20565 ± 49	322 ± 134	43	0.082	
1149	165.7401	+7.6031	21247 ± 35	21522 ± 50	314 ± 37	39	0.173	
1155	166.1649	+35.2295	22139 ± 95	22063 ± 52	277 ± 41	28	0.101	
1169	166.9560	+43.9166	17531 ± 6	17664 ± 78	738 ± 49	89	0.050	
1171	166.8750	+2.9101	22666 ± 38	22459 ± 91	388 ± 56	18	0.225	
1177	167.4355	+21.7588	9561 ± 26	9597 ± 49	331 ± 59	45	0.077	N3551 15K
1185	167.6597	+28.7675	10521 ± 30	9791 ± 56	758 ± 54	183	0.124	N3550 15K
1186	168.5090	+75.4309	23540 ± 30	23540 ± 30	...	1	0.263	
1187	167.7902	+39.5976	23714 ± 0	22397 ± 118	952 ± 55	65	0.094	
1190	167.9320	+40.8205	23489 ± 36	22584 ± 64	671 ± 43	110	0.075	
1203	168.4510	+40.2856	22655 ± 38	22565 ± 55	552 ± 36	99	0.121	
1213	169.0953	+29.2523	13535 ± 35	14051 ± 51	572 ± 43	125	0.080	15K
1216	169.5337	-4.4303	15885 ± 24	15994 ± 78	390 ± 51	25	0.217	
1228	170.3466	+34.3568	10674 ± 29	10549 ± 28	246 ± 23	76	0.102	I2738 15K
1238	170.7267	+1.1142	21628 ± 150	22149 ± 58	564 ± 46	94	0.155	
1257	171.3796	+35.5042	10175 ± 39	10430 ± 138	1202 ± 58	75	0.098	15K
1267	172.1517	+26.9054	9795 ± 39	9880 ± 34	210 ± 52	38	0.081	15K
1279	172.9149	+67.2414	16258 ± 18	16293 ± 38	186 ± 30	23	0.050	
1291	173.0499	+56.0477	17556 ± 67	17502 ± 78	724 ± 53	85	0.080	
1308	173.2712	-4.0138	15535 ± 27	15465 ± 67	375 ± 31	31	0.199	15K
1314	173.7059	+49.0773	9999 ± 31	9877 ± 58	648 ± 25	123	0.071	I0712 15K
1317	173.8044	-13.5519	21632 ± 40	21706 ± 185	717 ± 111	15	0.160	
1318	174.3931	+54.8529	17335 ± 37	16992 ± 59	482 ± 36	66	0.057	



Table 1 — *Continued*

Abell	$\alpha$ (2000)	$\delta$ (2000)	$V_1$ km s <sup>-1</sup>	$V_c$ km s <sup>-1</sup>	$\sigma_c$ km s <sup>-1</sup>	$N_g$	$A_B$	Notes
1334	174.7656	-4.3177	16882 ± 49	16706 ± 102	687 ± 70	45	0.218	
1344	175.2210	-10.7238	23213 ± 6	23300 ± 68	137 ± 142	4	0.125	
1365	176.1274	+30.8831	22904 ± 41	22709 ± 78	369 ± 61	22	0.104	
1367	176.0090	+19.9496	6276 ± 21	6562 ± 59	872 ± 42	217	0.100	N3842 15K
1371	176.3290	+15.4867	20348 ± 45	20475 ± 68	577 ± 50	71	0.188	
1375	176.5157	-8.2711	22338 ± 50	23951 ± 285	570 ± 530	4	0.209	10734
1377	176.8394	+55.7297	15457 ± 36	15465 ± 66	745 ± 47	126	0.047	
1383	177.1909	+54.5190	17988 ± 51	17898 ± 85	816 ± 39	92	0.057	
1400	177.8067	+55.1161	23684 ± 60	23819 ± 78	332 ± 53	18	0.058	
1404	178.0518	-2.8050	23182 ± 46	23251 ± 74	365 ± 52	24	0.080	
1424	179.3710	+5.0889	23150 ± 13	22708 ± 77	697 ± 55	80	0.089	
1436	179.8603	+56.4036	18889 ± 36	19464 ± 71	703 ± 36	97	0.077	
1452	180.8684	+51.7153	18229 ± 37	18608 ± 86	560 ± 63	42	0.098	
1461	181.1035	+42.5615	16180 ± 27	15984 ± 66	402 ± 35	37	0.045	
1474	182.0659	+15.0380	24327 ± 38	24135 ± 94	739 ± 42	61	0.138	
1507	183.7030	+59.9060	18438 ± 30	18024 ± 50	405 ± 48	65	0.082	N4199
1520	184.8960	-13.4368	21260 ± 30	20853 ± 92	320 ± 180	12	0.238	
1534	186.1789	+61.4705	21008 ± 7	20983 ± 64	371 ± 55	33	0.081	
1569	189.0342	+16.6411	23597 ± 4	23814 ± 105	622 ± 1314	35	0.123	13557
1589	190.3230	+18.5743	20955 ± 0	21643 ± 99	899 ± 546	82	0.090	
1610	191.9402	+30.0769	18174 ± 0	18659 ± 62	292 ± 403	22	0.070	10822
1630	192.9729	+4.5796	19355 ± 47	19529 ± 71	441 ± 53	38	0.159	
1631	193.3258	-15.5328	14278 ± 3	13830 ± 43	753 ± 24	305	0.235	15K
1644	194.2990	-17.4097	14267 ± 49	14120 ± 61	1016 ± 49	273	0.309	15K
1648	194.7155	-26.6492	23462 ± 53	23182 ± 294	721 ± 382	6	0.339	
1656	195.0335	+27.9767	6498 ± 10	6960 ± 38	1035 ± 25	713	0.035	N4889 15K
1691	197.7863	+39.2267	21686 ± 16	21723 ± 79	784 ± 45	97	0.074	
1709	199.6266	-21.4416	15429 ± 45	15700 ± 114	414 ± 173	13	0.585	
1736	201.8668	-27.3243	13608 ± 65	13530 ± 95	1127 ± 54	139	0.250	14252 15K
1741	201.1101	+71.4055	22650 ± 42	22650 ± 42	...	2	0.064	
1749	202.3377	+37.6227	16881 ± 7	16838 ± 94	707 ± 66	56	0.047	14269
1767	204.0354	+59.2061	21194 ± 150	21150 ± 78	887 ± 31	127	0.047	
1773	205.5404	+2.2270	23232 ± 6	23257 ± 84	839 ± 59	98	0.124	
1775	205.4551	+26.3736	22616 ± 39	22581 ± 64	568 ± 60	77	0.050	U08669
1780	206.1360	+2.9538	23259 ± 42	23276 ± 74	590 ± 44	62	0.114	
1795	207.2191	+26.5927	19019 ± 92	18797 ± 64	861 ± 56	177	0.055	
1800	207.3484	+28.1070	22554 ± 42	22590 ± 84	767 ± 190	82	0.066	U08738
1809	208.2769	+5.1494	23618 ± 40	23822 ± 71	745 ± 30	110	0.112	
1825	209.5019	+20.6318	18050 ± 10	18919 ± 154	1024 ± 0	44	0.136	U08888
1827	209.5256	+21.6722	19917 ± 39	19743 ± 49	282 ± 76	32	0.136	
1828	209.5617	+18.3459	18830 ± 20	18736 ± 94	388 ± 84	17	0.124	
1831	209.8131	+27.9760	22777 ± 41	22644 ± 111	1176 ± 118	112	0.083	
1836	210.4243	-11.6063	11231 ± 68	11275 ± 48	354 ± 37	54	0.277	15K
1873	212.8771	+28.1707	22983 ± 44	22594 ± 169	656 ± 0	15	0.085	
1890	214.4077	+8.1792	17569 ± 16	17294 ± 61	550 ± 59	80	0.147	N5539
1898	215.1374	+25.3439	23695 ± 24	23589 ± 74	419 ± 111	32	0.090	
1899	215.4241	+17.7520	16445 ± 39	15796 ± 89	646 ± 0	52	0.112	
1904	215.5429	+48.5701	21555 ± 0	21533 ± 66	772 ± 31	134	0.090	
1913	216.8215	+16.8307	15452 ± 39	15944 ± 60	636 ± 130	111	0.106	14426
1964	221.6482	-8.7685	21313 ± 44	21313 ± 44	...	2	0.364	
1982	222.8104	+30.6919	16494 ± 62	16775 ± 241	1325 ± 0	30	0.088	
1983	223.1802	+16.9036	13829 ± 39	13499 ± 48	541 ± 27	122	0.114	15K
1991	223.6314	+18.6420	17752 ± 14	17538 ± 69	604 ± 57	76	0.144	N5778
2022	226.0664	+28.4963	16938 ± 0	17354 ± 68	607 ± 74	79	0.120	
2028	227.3677	+7.5563	23148 ± 35	23213 ± 89	658 ± 57	54	0.149	
2029	227.7337	+5.7444	23401 ± 9	23186 ± 124	1222 ± 75	97	0.170	I1101
2040	228.1989	+7.4339	13734 ± 47	13530 ± 52	567 ± 39	119	0.186	U09767 15K
2052	229.1856	+7.0213	10314 ± 14	10406 ± 65	681 ± 41	109	0.160	U09799 15K
2061	230.3360	+30.6706	23706 ± 34	23436 ± 66	851 ± 28	166	0.091	
2063	230.7728	+8.6092	10269 ± 36	10474 ± 78	930 ± 57	141	0.147	15K
2065	230.6005	+27.7141	20740 ± 15	21667 ± 109	1286 ± 140	137	0.174	
2067	230.7852	+30.8771	22061 ± 54	22346 ± 69	621 ± 31	80	0.093	
2079	231.9383	+28.9286	19616 ± 33	19828 ± 68	676 ± 41	97	0.096	U09861
2089	233.2082	+28.0392	22073 ± 21	22072 ± 80	593 ± 57	55	0.123	
2092	233.3144	+31.1446	20410 ± 45	19979 ± 53	470 ± 49	77	0.110	
2107	234.9127	+21.7821	12611 ± 60	12429 ± 66	629 ± 46	90	0.247	U09958 15K
2147	240.5710	+15.9743	10617 ± 42	10978 ± 54	1033 ± 33	359	0.139	U10143 15K
2151	241.1490	+17.7217	10552 ± 23	10937 ± 46	842 ± 30	335	0.205	N6041A 15K
2152	241.3720	+16.4364	13249 ± 59	13243 ± 50	456 ± 62	81	0.172	U10187 15K
2162	243.1489	+29.4843	9581 ± 5	9679 ± 57	435 ± 37	57	0.161	N6086 15K
2184	245.2711	+50.2223	16017 ± 6	16361 ± 124	634 ± 357	26	0.092	
2197	247.4377	+40.8118	8825 ± 8	9093 ± 41	615 ± 21	216	0.031	N6173 15K
2198	246.9807	+43.9480	17485 ± 32	17581 ± 69	208 ± 60	9	0.031	
2199	247.1602	+39.5508	9317 ± 10	9088 ± 38	819 ± 32	454	0.050	N6166 15K
2241	254.7856	+32.5005	18467 ± 60	18573 ± 57	275 ± 42	23	0.130	
2247	253.2003	+81.6328	11135 ± 18	11583 ± 75	353 ± 59	22	0.274	U10638 15K

Table 1 — *Continued*

Abell	$\alpha$ (2000)	$\delta$ (2000)	$V_1$ km s <sup>-1</sup>	$V_c$ km s <sup>-1</sup>	$\sigma_c$ km s <sup>-1</sup>	$N_g$	$A_B$	Notes
2248	254.7646	+77.0476	19481 ± 60	19128 ± 306	1224 ± 1758	16	0.168	
2250	257.7555	+39.6903	19721 ± 40	19416 ± 160	699 ± 0	19	0.186	
2256	256.1144	+78.6401	17808 ± 53	17461 ± 75	1301 ± 42	299	0.227	U10726
2271	259.5696	+78.0182	16962 ± 45	17133 ± 162	538 ± 135	11	0.183	
2293	270.5712	+57.5480	21151 ± 35	20782 ± 337	754 ± 0	5	0.225	
2308	278.5358	+70.9552	23970 ± 39	23970 ± 39	...	2	0.287	
2309	279.7795	+77.8395	15393 ± 49	15393 ± 49	...	3	0.318	
2325	307.5258	-24.9837	24129 ± 51	24154 ± 146	293 ± 0	4	0.225	
2331	314.5507	-7.7599	23681 ± 44	24092 ± 141	788 ± 101	31	0.348	
2361	324.7629	-14.3646	17987 ± 54	18260 ± 46	313 ± 36	46	0.231	
2362	325.0611	-14.2315	18379 ± 35	18238 ± 47	321 ± 39	45	0.242	
2366	325.7031	-6.8687	16130 ± 31	15908 ± 69	540 ± 49	61	0.189	
2370	326.0999	-19.4410	17728 ± 36	17783 ± 281	744 ± 260	7	0.158	
2372	326.3148	-19.9947	17623 ± 39	17857 ± 231	612 ± 183	7	0.154	
2382	327.9820	-15.7063	19704 ± 40	19170 ± 66	900 ± 81	184	0.248	
2383	327.8515	-21.0779	17224 ± 54	17252 ± 33	75 ± 162	5	0.164	
2388	328.4138	+8.2524	18202 ± 36	18202 ± 36	...	1	0.209	
2399	329.2572	-7.8397	18630 ± 35	17370 ± 51	713 ± 27	190	0.168	
2401	329.5939	-20.1046	17379 ± 48	17164 ± 83	470 ± 62	32	0.126	
2405	329.9260	-17.8009	10961 ± 41	11045 ± 78	234 ± 47	9	0.179	
2412	331.0102	-21.4482	21963 ± 42	21620 ± 370	1282 ± 281	12	0.161	
2415	331.3591	-5.7424	17007 ± 31	17291 ± 70	722 ± 202	105	0.286	
2457	338.9204	+1.4845	17602 ± 43	17608 ± 67	642 ± 53	91	0.363	
2459	339.1904	-15.7347	21822 ± 42	21898 ± 234	620 ± 218	7	0.225	
2462	339.7976	-17.3413	22281 ± 53	22235 ± 96	702 ± 67	53	0.153	
2469	340.1448	+12.3115	18918 ± 40	18918 ± 40	...	2	0.213	
2480	341.4961	-17.6258	20450 ± 41	21640 ± 237	823 ± 187	12	0.123	
2492	342.6269	-19.2430	20728 ± 39	20968 ± 233	739 ± 336	10	0.123	
2495	342.5824	+10.9033	23895 ± 45	23744 ± 212	638 ± 188	9	0.329	
2511	344.7129	-7.5828	23078 ± 51	23359 ± 238	534 ± 816	5	0.192	
2524	345.7331	+17.7498	24304 ± 33	23902 ± 173	627 ± 175	13	0.400	
2525	346.0086	-10.7519	23554 ± 47	23568 ± 81	425 ± 48	27	0.167	
2558	348.1816	+10.3619	19450 ± 38	19450 ± 38	...	2	0.188	
2559	348.2615	-13.6233	23770 ± 44	23749 ± 57	163 ± 75	8	0.140	
2572	349.3064	+18.7078	12175 ± 61	11638 ± 62	593 ± 36	90	0.222	N7578B 15K
2589	350.9898	+16.7766	12442 ± 57	12394 ± 84	872 ± 60	107	0.129	N7647 15K
2593	351.0840	+14.6473	12507 ± 28	12532 ± 43	644 ± 23	217	0.188	N7649 15K
2618	353.5233	+22.9830	21036 ± 36	21036 ± 36	...	2	0.343	
2622	353.7563	+27.3719	18417 ± 38	18296 ± 114	860 ± 121	56	0.246	
2625	354.4560	+20.8091	17200 ± 46	18063 ± 235	1506 ± 171	41	0.295	
2626	354.1276	+21.1466	16559 ± 38	16505 ± 73	648 ± 53	78	0.270	I5338
2630	354.5735	+15.6689	19788 ± 39	20087 ± 68	420 ± 1336	38	0.265	
2634	354.6227	+27.0305	9105 ± 44	9343 ± 66	919 ± 45	193	0.303	N7720 15K
2637	354.7225	+21.4644	21283 ± 37	21104 ± 90	361 ± 59	16	0.187	
2644	355.2803	+0.0949	20599 ± 33	20684 ± 205	943 ± 50	21	0.127	
2656	356.1805	-4.0123	23034 ± 41	22926 ± 262	695 ± 280	7	0.165	
2657	356.1270	+9.2643	12296 ± 59	12019 ± 105	807 ± 52	59	0.546	15K
2660	356.3166	-25.8358	16398 ± 59	15953 ± 107	870 ± 71	65	0.088	E537-G005
2665	357.7109	+6.1492	16840 ± 57	16840 ± 57	...	3	0.345	
2666	357.7444	+27.1466	8165 ± 43	8240 ± 66	377 ± 47	32	0.168	N7768 15K
2670	358.5570	-10.4193	23290 ± 51	22870 ± 66	963 ± 34	208	0.187	
2675	358.9278	+11.3429	22168 ± 44	21559 ± 117	372 ± 156	10	0.362	
2678	359.0014	+11.7238	21475 ± 41	21552 ± 108	361 ± 156	11	0.347	
2716	0.7546	-27.1355	20134 ± 78	19905 ± 91	683 ± 58	56	0.072	
2717	0.8032	-35.9380	14853 ± 34	14814 ± 60	568 ± 40	89	0.045	E349-G022 15K
2731	2.4960	-57.0216	9434 ± 33	9236 ± 86	564 ± 76	43	0.064	N0025 15K
2734	2.8406	-28.8548	18456 ± 39	18461 ± 68	843 ± 49	151	0.072	E409-G025
2764	5.1489	-49.2132	21424 ± 55	21370 ± 177	924 ± 119	27	0.073	E194-G006
2771	6.1340	-40.1253	20839 ± 40	20984 ± 56	285 ± 46	26	0.039	
2793	8.4373	-82.6024	17498 ± 23	17498 ± 23	...	2	0.691	
2799	9.3651	-39.1301	19015 ± 23	19042 ± 58	475 ± 40	67	0.056	
2800	9.4902	-25.0741	18999 ± 24	18948 ± 48	397 ± 29	66	0.066	
2806	10.2020	-56.2148	8188 ± 37	8291 ± 67	435 ± 78	42	0.065	N0215 15K
2810	10.3740	-61.0817	17138 ± 26	17221 ± 113	321 ± 0	8	0.060	
2819	11.5212	-63.5555	22369 ± 49	22396 ± 64	445 ± 46	48	0.100	
2824	12.1252	-21.3606	18382 ± 39	18131 ± 94	311 ± 104	11	0.070	
2836	13.2174	-47.6247	23684 ± 0	23684 ± 0	...	2	0.067	
2841	13.7691	-48.9383	19342 ± 28	19360 ± 19	38 ± 850	4	0.045	
2854	15.1947	-50.5350	18209 ± 27	18541 ± 63	397 ± 45	39	0.062	E195-G022
2859	15.5518	-67.5813	19491 ± 43	19825 ± 9	21 ± 0	5	0.078	
2864	16.0347	-66.9799	20948 ± 47	20948 ± 47	...	3	0.086	
2870	16.9243	-46.9087	6728 ± 45	6744 ± 170	1165 ± 46	47	0.058	I1625 15K
2877	17.4784	-45.9326	7216 ± 19	7335 ± 98	991 ± 63	102	0.051	I1633 15K
2881	17.8089	-17.0707	13208 ± 57	13674 ± 377	1510 ± 202	16	0.086	15K
2896	19.5775	-37.1047	9473 ± 28	9923 ± 351	995 ± 537	8	0.077	E352-G038 15K
2923	23.0894	-31.0925	21376 ± 37	21395 ± 70	377 ± 50	29	0.089	

Table 1 — *Continued*

Abell	$\alpha$ (2000)	$\delta$ (2000)	$V_1$ km s <sup>-1</sup>	$V_c$ km s <sup>-1</sup>	$\sigma_c$ km s <sup>-1</sup>	$N_g$	$A_B$	Notes
2954	28.9372	-71.4585	16943 ± 87	16975 ± 29	71 ± 43	6	0.141	
2992	33.7125	-26.6601	17389 ± 21	17259 ± 79	463 ± 46	34	0.060	
3004	34.7164	-47.9995	19866 ± 20	19686 ± 188	625 ± 192	11	0.107	
3009	35.5305	-48.5645	19754 ± 26	19731 ± 189	846 ± 170	20	0.071	
3027	37.4830	-33.1779	23761 ± 38	23020 ± 91	909 ± 40	99	0.097	
3045	40.9220	-51.4615	22623 ± 41	22569 ± 274	727 ± 419	7	0.116	
3074	44.5472	-52.7287	21790 ± 44	21578 ± 113	299 ± 107	7	0.084	
3078	45.1065	-51.8475	21771 ± 28	21836 ± 78	500 ± 55	41	0.085	
3089	47.0707	-36.7088	19524 ± 33	19915 ± 122	691 ± 105	32	0.089	
3094	47.8544	-26.9315	20577 ± 31	20269 ± 71	762 ± 47	115	0.071	E481-G006
3095	48.1109	-27.1403	19468 ± 41	19803 ± 90	607 ± 50	45	0.093	E481-G012
3098	48.4314	-38.3037	23895 ± 33	24482 ± 160	679 ± 38	18	0.078	E300-G019
3100	48.4702	-47.7930	18642 ± 230	18910 ± 87	338 ± 55	15	0.076	
3104	48.5910	-45.4206	21791 ± 35	21778 ± 84	618 ± 57	53	0.100	
3106	48.6246	-58.0968	19523 ± 38	19461 ± 112	355 ± 104	10	0.116	E116-G013
3107	49.0260	-42.7534	19833 ± 26	19534 ± 124	483 ± 97	15	0.070	
3109	49.1643	-43.8547	18608 ± 32	19372 ± 261	1045 ± 195	16	0.061	
3110	49.0517	-50.9534	22249 ± 33	22890 ± 270	975 ± 148	13	0.111	
3111	49.4382	-45.7557	23044 ± 47	23201 ± 131	839 ± 93	41	0.123	
3112	49.4905	-44.2382	22777 ± 56	22540 ± 104	919 ± 71	78	0.052	E248-G006
3120	50.4853	-51.3268	21413 ± 44	20543 ± 444	1332 ± 469	9	0.095	
3122	50.5760	-41.3282	20130 ± 45	19137 ± 83	869 ± 59	108	0.075	
3123	50.7284	-52.0303	18278 ± 48	18409 ± 110	480 ± 173	19	0.072	
3125	51.9783	-53.3717	17444 ± 37	18189 ± 61	614 ± 17	101	0.068	
3128	52.6601	-52.6201	17693 ± 39	18030 ± 48	892 ± 42	341	0.070	
3133	53.0252	-45.9300	21377 ± 67	21014 ± 194	726 ± 166	14	0.042	
3135	53.5281	-38.9930	18316 ± 47	18770 ± 96	775 ± 49	65	0.081	
3142	54.1561	-39.7948	20068 ± 30	19986 ± 205	918 ± 138	20	0.066	
3144	54.2703	-55.0224	13205 ± 28	13525 ± 109	598 ± 86	30	0.068	15K
3151	55.1127	-28.6772	20274 ± 52	20339 ± 119	935 ± 72	61	0.053	
3158	55.8747	-53.6924	18766 ± 40	17771 ± 69	1095 ± 37	252	0.066	
3164	56.4457	-57.0358	17823 ± 47	17647 ± 153	703 ± 106	21	0.118	
3188	59.3486	-27.1213	19316 ± 22	19193 ± 181	993 ± 77	30	0.053	
3193	59.5564	-52.3290	10103 ± 31	10188 ± 74	451 ± 51	37	0.058	N1500 15K
3195	59.7288	-35.3026	22525 ± 32	22525 ± 32	...	3	0.022	
3202	59.8714	-53.6396	21090 ± 17	20830 ± 110	613 ± 55	31	0.085	
3223	62.1360	-30.8223	17923 ± 29	18002 ± 87	790 ± 51	81	0.068	
3225	62.4046	-59.5919	16994 ± 33	16740 ± 165	1226 ± 110	55	0.083	
3231	62.8154	-64.5356	23152 ± 39	23152 ± 39	...	1	0.198	
3266	67.8066	-61.4536	18025 ± 181	17768 ± 63	1251 ± 41	387	0.088	E118-G030
3301	75.2054	-38.6745	16297 ± 23	16231 ± 144	706 ± 77	24	0.093	N1759
3323	77.8447	-28.9924	19221 ± 47	19070 ± 59	145 ± 40	6	0.059	E422-G043
3332	79.1462	-42.2029	23954 ± 45	23954 ± 45	...	1	0.109	
3336	80.3782	-40.8173	23900 ± 34	23734 ± 57	114 ± 116	4	0.109	
3341	81.3970	-31.6020	11024 ± 30	11279 ± 63	574 ± 50	83	0.083	
3354	83.6795	-28.6906	17623 ± 60	17504 ± 60	435 ± 49	52	0.113	
3367	87.4238	-24.5455	13432 ± 84	13480 ± 49	273 ± 121	31	0.129	15K
3374	89.1790	-21.2534	14237 ± 62	14552 ± 114	343 ± 0	9	0.264	15K
3376	90.1709	-40.0463	13829 ± 30	13831 ± 68	855 ± 54	154	0.223	E307-G013 15K
3380	91.7425	-49.4934	15692 ± 34	15831 ± 165	573 ± 0	12	0.224	
3381	92.4740	-33.5928	11493 ± 3	11358 ± 50	333 ± 34	43	0.160	15K
3389	95.5888	-64.9346	8263 ± 23	8052 ± 77	616 ± 64	63	0.333	N2235 15K
3390	96.1659	-37.3359	9283 ± 5	9818 ± 179	1062 ± 155	35	0.358	
3391	96.5850	-53.6934	16522 ± 43	16178 ± 110	1209 ± 55	119	0.408	E161-G007
3392	96.7778	-35.4879	16379 ± 33	16513 ± 97	437 ± 71	20	0.288	
3395	96.9018	-54.4505	14613 ± 29	15132 ± 70	950 ± 57	181	0.486	E161-G008 15K
3407	106.2470	-49.0835	11780 ± 48	12819 ± 111	684 ± 125	38	0.361	E207-G019
3408	107.1236	-49.2137	12483 ± 44	12623 ± 111	638 ± 87	33	0.397	
3420	143.0290	-24.8179	18973 ± 21	18891 ± 121	438 ± 109	13	0.286	
3429	149.8525	-24.9711	14044 ± 42	14768 ± 122	503 ± 78	17	0.261	E499-G030
3432	150.3548	-33.0243	20598 ± 30	20588 ± 55	123 ± 90	5	0.513	
3490	176.3340	-34.4338	20417 ± 36	20589 ± 101	996 ± 158	97	0.374	
3492	179.0938	-33.5132	17125 ± 0	17174 ± 196	481 ± 212	6	0.407	
3494	179.2911	-32.1520	20690 ± 39	20566 ± 104	208 ± 112	4	0.316	
3497	180.0257	-31.3881	20489 ± 49	20413 ± 71	761 ± 81	112	0.309	
3500	180.7318	-30.1275	13249 ± 20	13249 ± 20	...	3	0.313	
3505	182.1788	-34.4436	17322 ± 27	17471 ± 91	389 ± 84	18	0.330	
3526	192.2039	-41.3117	2904 ± 40	3218 ± 58	794 ± 43	182	0.492	N4696 15K
3528	193.5930	-29.0128	16377 ± 51	16330 ± 75	961 ± 35	160	0.334	E443-G004 15K
3530	193.9004	-30.3470	16274 ± 81	16338 ± 103	716 ± 82	48	0.373	E443-G011 15K
3531	194.2873	-32.9168	23105 ± 0	22910 ± 136	409 ± 120	9	0.359	
3532	194.3423	-30.3632	16256 ± 34	16641 ± 82	734 ± 60	79	0.366	15K
3537	195.2530	-32.4414	5072 ± 6	4917 ± 54	333 ± 30	38	0.403	E443-G024 15K
3542	197.1730	-34.5754	10372 ± 34	10372 ± 34	...	2	0.249	15K
3548	198.5019	-44.1782	15618 ± 42	15759 ± 151	566 ± 124	14	0.670	
3549	198.5258	-29.4249	22408 ± 33	22586 ± 101	227 ± 64	5	0.244	

Table 1 — *Continued*

Abell	$\alpha$ (2000)	$\delta$ (2000)	$V_1$ km s <sup>-1</sup>	$V_c$ km s <sup>-1</sup>	$\sigma_c$ km s <sup>-1</sup>	$N_g$	$A_B$	Notes
3552	199.7300	-31.8179	15573 ± 25	15354 ± 180	903 ± 100	25	0.251	
3553	199.8128	-37.1796	14551 ± 29	15172 ± 89	448 ± 90	25	0.252	15K
3554	199.8814	-33.4888	14220 ± 67	14648 ± 96	562 ± 75	34	0.276	E382-G043 15K
3556	201.0282	-31.6708	14424 ± 38	14339 ± 48	657 ± 46	186	0.259	E444-G025 15K
3557	201.2298	-28.8877	23405 ± 61	23341 ± 78	222 ± 230	8	0.256	
3558	201.9855	-31.4963	13986 ± 98	14294 ± 64	1002 ± 51	240	0.218	E444-G046 15K
3559	202.4626	-29.5147	14116 ± 8	14134 ± 87	688 ± 49	62	0.241	E444-G055 15K
3560	202.9722	-33.2346	3705 ± 9	3634 ± 75	261 ± 131	12	0.240	N5193 15K
3562	203.3947	-31.6723	14677 ± 38	14605 ± 94	966 ± 60	105	0.251	E444-G072 15K
3563	203.4536	-42.5430	21202 ± 31	20264 ± 188	777 ± 144	17	0.462	
3564	203.7307	-35.0994	14468 ± 44	14958 ± 155	490 ± 127	10	0.266	15K
3565	204.1627	-33.9658	3754 ± 50	3848 ± 48	414 ± 29	73	0.267	14296 15K
3570	206.6000	-37.9710	11298 ± 36	11146 ± 71	530 ± 39	55	0.351	E325-G016 15K
3571	206.8684	-32.8644	11563 ± 44	11718 ± 107	1128 ± 59	111	0.233	E383-G076 15K
3572	207.0594	-33.3827	12201 ± 28	11830 ± 132	1008 ± 111	58	0.235	15K
3574	207.2720	-30.2958	4538 ± 40	4673 ± 53	566 ± 29	114	0.261	14329 15K
3575	208.1598	-32.8881	11132 ± 19	11216 ± 131	571 ± 99	19	0.247	15K
3577	208.5615	-27.8481	14776 ± 49	14668 ± 94	561 ± 59	35	0.297	
3581	211.8730	-27.0186	6531 ± 29	6506 ± 61	526 ± 47	73	0.263	14374 15K
3599	216.9523	-23.5421	7697 ± 44	6978 ± 292	773 ± 146	7	0.397	
3603	218.3521	-31.8254	18052 ± 0	18128 ± 166	471 ± 171	8	0.379	
3605	218.7682	-28.4255	20633 ± 33	19335 ± 254	623 ± 214	6	0.383	
3615	225.7287	-80.5623	20356 ± 47	20356 ± 191	506 ± 0	7	1.333	
3651	298.0359	-55.0628	17923 ± 28	17958 ± 86	777 ± 61	81	0.229	
3656	300.2082	-38.5766	5972 ± 6	5835 ± 55	386 ± 48	48	0.313	14931 15K
3667	303.1139	-56.8271	16621 ± 51	16558 ± 76	1028 ± 59	179	0.210	14965
3676	306.1021	-40.3665	12124 ± 15	12153 ± 57	127 ± 90	5	0.184	E340-G025 15K
3677	306.5982	-33.3510	13850 ± 47	12388 ± 541	1210 ± 607	5	0.303	15K
3684	308.8428	-78.0939	23036 ± 2	23036 ± 2	...	3	0.682	
3685	308.0675	-56.4277	18632 ± 13	18632 ± 13	...	2	0.252	
3687	308.2502	-63.0292	22898 ± 47	22980 ± 126	358 ± 85	8	0.306	
3698	308.9842	-25.2792	5817 ± 20	5860 ± 59	244 ± 60	17	0.194	N6936 15K
3703	310.0072	-61.3338	21551 ± 44	21929 ± 100	458 ± 76	21	0.231	
3716	312.9867	-52.6300	14046 ± 34	13895 ± 72	609 ± 49	70	0.158	E187-G026 15K
3731	315.4248	-38.4983	13860 ± 45	13821 ± 78	391 ± 47	25	0.193	
3733	315.4961	-28.0596	10990 ± 24	11586 ± 75	743 ± 52	96	0.495	N6999 15K
3736	316.2687	-43.4192	14577 ± 33	14340 ± 127	311 ± 233	6	0.127	E286-G041 15K
3741	317.7610	-82.1486	23114 ± 6	23114 ± 6	...	2	0.774	
3742	316.9678	-47.1787	4811 ± 38	5012 ± 38	269 ± 29	48	0.143	N7014 15K
3744	316.8175	-25.4690	11005 ± 16	11465 ± 68	653 ± 37	90	0.277	N7016 15K
3747	317.1622	-43.4864	9317 ± 2	9244 ± 83	299 ± 50	13	0.133	E286-G059 15K
3753	318.6332	-26.7703	21840 ± 57	21840 ± 57	...	2	0.328	
3764	321.5746	-34.7851	23965 ± 39	22696 ± 97	781 ± 56	64	0.344	
3771	322.4437	-50.7058	22086 ± 39	22642 ± 178	536 ± 920	9	0.110	
3781	323.6044	-66.8459	17091 ± 60	17050 ± 54	122 ± 86	5	0.137	
3782	323.7987	-62.0790	16879 ± 36	16999 ± 144	557 ± 190	15	0.169	
3785	323.5741	-53.6369	22876 ± 60	23492 ± 249	897 ± 312	13	0.077	
3796	324.8754	-51.3957	22693 ± 58	22898 ± 98	197 ± 0	4	0.119	
3799	325.7601	-72.6601	13714 ± 54	13591 ± 142	493 ± 122	12	0.209	
3806	326.5950	-57.2874	22359 ± 3	23005 ± 121	991 ± 58	67	0.150	
3809	326.7465	-43.8992	18642 ± 33	18719 ± 55	677 ± 39	150	0.078	
3816	327.8754	-55.3375	11417 ± 46	11573 ± 61	354 ± 61	33	0.095	
3822	328.7510	-57.6579	23315 ± 51	22720 ± 107	942 ± 76	77	0.128	
3825	329.5412	-60.2455	21276 ± 54	22431 ± 114	865 ± 70	57	0.157	
3826	330.1012	-56.1786	22654 ± 48	22654 ± 48	...	1	0.088	
3844	333.3238	-34.6668	21897 ± 31	21903 ± 39	154 ± 30	15	0.067	
3851	334.2507	-52.5274	16148 ± 21	16116 ± 81	345 ± 64	18	0.081	
3869	335.1294	-55.1250	11869 ± 10	12294 ± 113	253 ± 346	5	0.091	N7249 15K
3879	336.9555	-69.0236	19860 ± 26	20060 ± 76	474 ± 55	39	0.138	
3880	336.9770	-30.5763	17254 ± 29	17279 ± 77	854 ± 41	122	0.065	
3895	339.6907	-36.7444	18018 ± 43	17672 ± 94	532 ± 54	32	0.069	
3897	339.7978	-17.3416	22269 ± 53	22235 ± 96	702 ± 67	53	0.153	
3898	340.0435	-62.4152	22061 ± 28	22061 ± 28	...	1	0.107	
3912	341.5412	-36.0013	20168 ± 33	20664 ± 124	596 ± 71	23	0.055	
3925	342.7925	-46.6728	23289 ± 86	23916 ± 189	500 ± 194	7	0.045	
4008	352.6255	-39.2813	16415 ± 22	16410 ± 56	401 ± 49	51	0.077	
4038	356.8679	-28.1096	8201 ± 25	8950 ± 68	831 ± 35	146	0.081	I5353 15K
4049	357.9027	-28.3655	8227 ± 34	8817 ± 97	768 ± 53	62	0.087	I5362 15K
4059	359.2515	-34.7590	14740 ± 39	14740 ± 67	830 ± 37	151	0.075	E349-G010 15K

**Note.** — Columns: (1) Abell cluster number, (2) J2000 RA of the BCG, (3) J2000 Dec of the BCG, (4) heliocentric velocity of the BCG, (5) mean heliocentric cluster velocity, (6) cluster velocity dispersion (when  $N > 3$ ), (7) number of cluster galaxies used to derive the mean velocity and dispersion, (8) Schlegel et al. (1998)  $A_B$  extinction for the cluster, and (9) notes, which gives the NCG, UGC, IC, and ESO catalogue designations of the BCGs where available, and 15K denotes a BCG originally selected in the LP94 and PL95 sample.

**Table 2**  
Abell Clusters Not Observed

Abell	$V_c$ km s <sup>-1</sup>	$N_g$	Notes
A0087	16566 ± 75	166	No obs.
A0126	16142 ± 139	16	No obs.
A0160	12854 ± 85	113	No obs. M2 misidentified in 15K sample as BCG.
A0396	5301 ± 71	88	No obs.
A0419	20644 ± 127	48	No obs. Foreground group observed in 15K sample.
A0480	4363 ± 200	17	No obs.
A0484	20495 ± 246	20	No obs.
A0524	23330 ± 156	27	No obs.
A0833	20314 ± 161	17	No obs.
A0842	10056 ± 81	24	Non-E BCG
A0865	21707 ± 61	25	Non-E BCG
A0930	17250 ± 101	81	No obs.
A1218	24017 ± 87	23	Non-E BCG
A1270	20681 ± 67	66	Non-E BCG
A1275	18819 ± 64	32	No obs.
A1356	21735 ± 346	14	No obs.
A1423	23965 ± 107	31	No obs.
A1564	23810 ± 81	74	No obs.
A1638	18642 ± 131	4	No obs.
A1668	19192 ± 87	49	No obs.
A1781	18717 ± 67	53	No obs.
A1783	20545 ± 54	58	No obs.
A1837	20974 ± 116	36	No obs.
A1846	6329 ± 59	13	No obs.
A2004	19290 ± 24	1	Non-E BCG
A2020	14460 ± 104	16	Non-E BCG
A2033	23825 ± 180	40	No obs.
A2056	22704 ± 147	8	Non-E BCG
A2122	19793 ± 74	111	No obs.
A2124	19830 ± 76	110	No obs.
A2168	18807 ± 105	12	No obs.
A2169	17352 ± 52	82	No obs.
A2592	12082 ± 125	11	Non-E BCG
A2911	24085 ± 84	45	No obs. Foreground group observed in 15K sample.
A2995	11167 ± 51	7	Non-E BCG. Was in 15K sample.
A3108	18940 ± 89	17	No obs.
A3356	23035 ± 62	5	No obs.
A3397	22005 ± 264	6	No obs.
A3509	17151 ± 146	7	No obs.
A3524	22404 ± 268	22	No obs.
A3535	20203 ± 82	61	Non-E BCG
A3561	20242 ± 168	18	No obs.
A3566	15421 ± 69	48	Non-E BCG. Was in 15K sample.
A3578	11713 ± 230	40	No obs.
A3584	12362 ± 91	4	No obs.
A3623	7673 ± 817	3	Non-E BCG
A3626	20016 ± 39	1	Non-E BCG
A3631	21723 ± 0	1	Non-E BCG
A3756	22919 ± 152	9	No obs.
A3831	20720 ± 608	4	No obs.
A3963	20980 ± 70	9	No obs.
A4016	24115 ± 36	1	Non-E BCG
A4053	21094 ± 123	70	No obs.

**Note.** — Columns: (1) Abell cluster number, (2) mean heliocentric cluster velocity, (3) number of cluster galaxies used to derive the mean velocity, and (4) notes.

**Table 3**  
M2 Galaxy Sample

Abell	$\alpha$ (2000)	$\delta$ (2000)	$V_2$ km s <sup>-1</sup>	Notes
0027	6.2335	-20.7316	16241 ± 47	E539-G013; BCG by total flux
0071	9.4697	+29.6076	21436 ± 31	
0074	9.9201	-22.1967	19194 ± 0	
0075	9.8897	+21.2361	18494 ± 120	
0076	9.8896	+6.8146	11916 ± 31	I1566
0086	10.6667	-21.8004	17639 ± 49	
0102	12.1249	+1.3531	18613 ± 34	U00496
0116	14.0482	+0.6819	20086 ± 60	
0119	14.1064	-1.2625	11399 ± 54	U00583
0134	15.9356	-2.4188	21203 ± 32	
0147	17.0494	+2.1932	12587 ± 75	U00701
0154	17.7623	+17.6625	20107 ± 33	I1634
0161	18.8215	+37.3651	21934 ± 45	
0171	19.3645	+16.3065	20410 ± 41	
0174	20.0019	+35.8062	22459 ± 35	
0179	20.6370	+19.5252	16374 ± 43	BCG by total flux
0240	25.5183	+7.6503	17557 ± 31	VV 177a
0246	26.1973	+5.8316	21302 ± 24	
0399	44.5364	+13.0732	20498 ± 32	
0400	44.4230	+6.0267	6830 ± 10	N1128
0428	49.0694	-19.0834	20420 ± 38	
0436	51.7830	+9.1889	19453 ± 72	
0500	69.5581	-22.2383	20450 ± 0	
0533	75.4000	-22.6009	14642 ± 34	
0539	79.1556	+6.4411	8318 ± 47	U03274
0568	106.9300	+35.0603	22088 ± 150	
0576	110.3855	+55.7572	12177 ± 100	BCG by total flux
0582	112.0198	+41.9630	16916 ± 36	
0592	115.6812	+9.3683	18833 ± 30	
0595	117.3640	+52.0421	20514 ± 37	
0602	118.3612	+29.3592	18067 ± 49	BCG by total flux
0819	143.0760	+9.6983	22185 ± 60	
0838	144.2907	-5.0413	15068 ± 42	
0841	144.6379	-4.3265	21135 ± 40	
0970	154.3435	-10.6634	19483 ± 47	
0978	155.1824	-6.5330	16400 ± 60	
0979	155.0460	-7.8484	16158 ± 17	
1032	157.6027	+3.9917	20354 ± 56	
1066	159.7778	+5.2094	20310 ± 63	
1069	159.9942	-8.7903	19801 ± 66	
1142	165.2394	+10.5058	11150 ± 43	N3492
1145	165.4456	+16.7588	20664 ± 38	
1149	165.8353	+7.5123	21410 ± 57	
1169	166.9835	+43.9187	17378 ± 22	
1171	166.8335	+2.9718	22579 ± 40	BCG by total flux
1187	167.8013	+39.5969	22639 ± 0	
1190	167.9160	+40.8399	22100 ± 0	
1203	168.4483	+40.2979	22070 ± 63	
1228	170.4279	+34.3631	10578 ± 39	I2744
1238	170.7167	+1.1129	22095 ± 64	
1317	173.7233	-13.6104	21871 ± 0	
1318	174.0151	+55.0751	17155 ± 33	
1371	176.3427	+15.4951	20350 ± 100	
1375	176.5165	-8.2652	23751 ± 52	I0734; BCG by total flux
1377	177.0033	+55.7609	15260 ± 150	
1383	177.0247	+54.6459	17834 ± 150	BCG by total flux
1436	180.0593	+56.2501	19474 ± 34	BCG by total flux
1452	180.7798	+51.6748	19007 ± 46	
1630	192.7873	+4.5807	19943 ± 25	
1644	194.4554	-17.5457	14013 ± 50	
1648	194.7360	-26.6264	22664 ± 58	
1656	194.8985	+27.9592	7176 ± 15	N4874
1709	199.7237	-21.5127	16250 ± 60	E576-G028
1736	201.7029	-27.1436	13719 ± 49	E509-G009
1767	203.9866	+59.2330	21660 ± 100	
1773	205.6229	+2.2009	21480 ± 45	
1775	205.4604	+26.3703	20789 ± 37	U08669
1780	206.1693	+2.8616	23351 ± 51	
1809	208.2255	+5.1203	23439 ± 46	
1825	209.5139	+20.6185	18677 ± 60	U08888
1827	209.5400	+21.6976	19817 ± 42	
1890	214.3805	+8.2081	17079 ± 37	N5535
1898	215.1811	+25.1441	24227 ± 31	
1982	222.8340	+30.6636	14986 ± 62	

Table 3 — *Continued*

Abell	$\alpha$ (2000)	$\delta$ (2000)	$V_2$ km s <sup>-1</sup>	Notes
1983	223.2302	+16.7025	13581 ± 52	
2022	226.0306	+28.5194	17183 ± 31	
2028	227.3912	+7.5148	23485 ± 37	
2061	230.3936	+30.7202	23484 ± 42	
2065	230.6218	+27.7072	22454 ± 0	
2079	231.9355	+28.9182	19541 ± 35	U09861
2147	240.5530	+15.9078	10489 ± 39	U10143
2152	241.3607	+16.4424	13713 ± 0	U10187
2197	246.9216	+40.9269	9408 ± 77	N6160
2198	246.9654	+43.9598	17702 ± 18	
2241	254.7547	+32.4943	18710 ± 250	
2247	252.7461	+81.5746	11409 ± 98	U10638; BCG by total flux
2248	254.4118	+77.0629	19034 ± 0	
2250	257.7347	+39.6919	18666 ± 34	
2256	256.0550	+78.6281	16818 ± 39	
2293	270.3396	+57.6506	21198 ± 38	
2325	307.5208	-24.9819	23947 ± 50	
2331	314.4778	-7.6871	25471 ± 42	
2361	324.8019	-14.3188	17924 ± 40	
2370	326.1072	-19.4740	17672 ± 0	
2372	326.3107	-20.0080	17359 ± 32	
2382	327.9763	-15.6246	18843 ± 0	
2399	329.3729	-7.7960	17400 ± 30	
2412	331.1290	-21.4996	21200 ± 130	
2459	339.1995	-15.7443	21376 ± 0	BCG by total flux
2462	339.8252	-17.3369	22184 ± 75	
2492	342.6565	-19.2266	21912 ± 34	
2511	344.7271	-7.6024	23409 ± 45	BCG by total flux
2524	345.8252	17.6729	24399 ± 40	
2525	346.0455	-10.7735	24039 ± 0	
2572	349.3000	+18.7013	11974 ± 37	N7578A
2618	353.3166	+22.9409	20790 ± 38	
2625	354.2523	+20.6493	17538 ± 12	
2637	354.6761	+21.5009	21471 ± 43	
2656	356.1832	-4.0023	22935 ± 47	
2657	356.2393	+9.1919	12361 ± 46	BCG by total flux
2678	358.9390	+11.6533	22509 ± 40	
2764	5.1297	-49.2441	19834 ± 57	
2771	6.1129	-40.1361	21042 ± 0	
2793	8.3710	-82.6114	17976 ± 65	
2799	9.3500	-39.1387	19044 ± 54	
2800	9.5307	-25.0674	19969 ± 54	
2806	10.0538	-56.1542	8227 ± 13	N0212
2810	10.3557	-61.0804	17756 ± 21	
2819	11.5020	-63.5646	22383 ± 52	BCG by total flux
2824	12.1504	-21.3654	18125 ± 39	
2836	13.4048	-47.6053	22683 ± 51	
2854	15.2002	-50.5490	18777 ± 33	E195-G022
2859	15.3283	-67.5410	19940 ± 45	
2864	16.0524	-67.0099	21165 ± 75	
2881	17.7269	-17.1977	12665 ± 38	
2923	23.1002	-31.0835	20808 ± 38	
2954	28.8930	-71.4744	16926 ± 37	
3004	34.7666	-47.9751	19501 ± 45	
3027	37.6363	-33.0153	23391 ± 0	
3074	44.5271	-52.7475	21380 ± 64	
3078	45.1189	-51.8218	22151 ± 27	
3089	47.1586	-36.7471	18489 ± 107	
3094	47.8942	-26.8969	20534 ± 60	
3098	48.4282	-38.2978	25398 ± 32	E300-G019
3104	48.5439	-45.4444	21412 ± 43	
3106	48.3360	-58.1268	18989 ± 45	
3107	48.9867	-42.6537	18599 ± 34	
3109	49.1555	-43.8844	19444 ± 60	
3110	49.1302	-50.9120	22050 ± 100	
3120	50.4407	-51.3547	22215 ± 64	
3122	50.5850	-41.3628	19245 ± 36	
3123	50.7330	-52.0532	18056 ± 0	
3128	52.7127	-52.5090	17184 ± 60	
3133	53.2687	-45.9172	20544 ± 51	
3135	53.5141	-39.0103	18886 ± 0	
3151	55.1055	-28.6776	20403 ± 39	
3158	55.7212	-53.6314	17284 ± 54	E156-G008; BCG by total flux
3164	56.4810	-57.1971	19067 ± 150	
3223	62.1389	-30.8106	18685 ± 36	
3341	81.4110	-31.5530	10346 ± 54	

**Table 3** — *Continued*

Abell	$\alpha$ (2000)	$\delta$ (2000)	$V_2$ $\text{km s}^{-1}$	Notes
3354	83.5789	-28.6657	17737 $\pm$ 60	
3374	89.2291	-21.2517	14502 $\pm$ 36	
3389	95.3600	-64.9936	8023 $\pm$ 3	N2230
3391	96.5773	-53.6927	16034 $\pm$ 43	E161-G007
3408	107.0475	-49.1649	12610 $\pm$ 40	
3420	142.9985	-24.9731	19711 $\pm$ 0	
3492	179.0675	-33.4347	16855 $\pm$ 0	
3497	180.0851	-31.4336	20233 $\pm$ 0	
3505	182.1915	-34.4273	17546 $\pm$ 25	
3531	194.2284	-32.9491	23090 $\pm$ 45	
3548	198.2548	-44.0293	16429 $\pm$ 0	
3570	206.6972	-37.9079	11237 $\pm$ 74	
3577	208.5743	-27.8534	14082 $\pm$ 39	
3603	218.3657	-31.7045	18519 $\pm$ 68	
3605	218.7790	-28.3420	19527 $\pm$ 15	
3651	297.9859	-55.0043	18386 $\pm$ 57	
3733	315.4066	-28.0323	11793 $\pm$ 13	N6998
3764	321.4397	-34.7316	22166 $\pm$ 47	
3771	322.3297	-50.8846	23980 $\pm$ 61	
3785	323.5283	-53.5721	23491 $\pm$ 119	
3799	325.8549	-72.6641	13368 $\pm$ 70	
3822	328.5180	-57.8678	22615 $\pm$ 59	
3825	329.6099	-60.4261	22528 $\pm$ 46	
3844	333.3715	-34.6691	21975 $\pm$ 89	
3880	336.9610	-30.5622	16793 $\pm$ 39	
3895	339.6317	-36.7873	17517 $\pm$ 38	
3912	341.5176	-36.0255	18889 $\pm$ 0	
3925	342.7470	-46.6853	23624 $\pm$ 0	
4038	356.9373	-28.1421	8605 $\pm$ 30	I5358

**Note.** — Columns: (1) Abell cluster number, (2) J2000 RA of M2, (3) J2000 Dec of M2, (4) heliocentric velocity of M2, (5) notes, which gives the NCG, UGC, IC, and ESO catalogue designations of the BCGs where available. M2 galaxies that exceed the luminosity of the nominal BCG at large radii are indicated.



**Table 4**  
Summary of Imaging Runs

Run ID	Telescope	Detector	FOV (')	Scale ("'/pixel)
KP89F	4m	TI-2	3.99	0.299
CT89F	1.5m	TI-2	3.64	0.273
CT90F	1.5m	TI-2	3.64	0.273
KP91S	2.1m	TEK1024	5.19	0.304
CT91S	1.5m	TEK1024	7.41	0.434
KP93F	2.1m	TEK1024	5.19	0.304
CT93F	1.5m	TEK1024	7.41	0.434
CT94S	1.5m	TEK1024	7.41	0.434
KP94S	2.1m	T1KA	5.19	0.304
KP94F	2.1m	T1KA	5.19	0.304
CT94F	1.5m	TEK1024	7.41	0.434
CT95S	1.5m	TEK2K#4	14.80	0.434
KP95S	2.1m	T1KA	5.19	0.304

**Note.** — Run ID names encode the observatory (CT=CTIO, KP=KPNO), the year of the observations (e.g., 94 = 1994), and the observing semester (F=Fall, S=Spring). Note that the first five runs provided data for the 15K sample presented in PL95.

**Table 5**  
Summary of Spectroscopic Runs

Run ID	Telescope	Detector	Disperser	Slit P.A.	Spectral Range (Å)	Dispersion (Å/pixel)	Spatial Scale ("'/pixel)
CT92F	1.5-m	GEC-10	KPGL-3	90°	4351 – 5759	2.449	0.398
CT93S	1.5-m	GEC-10	KPGL-3	90°	4351 – 5759	2.447	0.398
KP92S	2.1-m	TI-800	G32	0°	4275 – 6247	2.471	...
KP92F	2.1-m	Ford 3KA	G32	0°	3344 – 7957	2.442	0.76
KP93S	2.1-m	Ford 3KA	G32	0°	3309 – 7949	2.443	0.76
CT94S	4-m	GEC-16	KPGL-2	90°	4629 – 6280	2.895	0.73
KP94S	2.1-m	Ford 3KC	G32	90°	3706 – 7850	2.440	0.76
CT94F	4-m	GEC-16	KPGL-2	90°	4723 – 6367	2.891	0.73
KP94F	2.1-m	Ford 3KC	G32	90°	3695 – 6852	2.431	0.76
CT95S	4-m	Loral 3K	KPGL-3	90°	3674 – 7351	1.220	0.51
CT95F	4-m	Loral 3K	KPGL-3	90°	3688 – 7357	1.224	0.51
KP95F	2.1-m	Ford 3KA	G32	90°	3536 – 7676	2.439	0.76
KP96S	2.1-m	Ford 3KB	G32	90°	3573 – 7712	2.439	0.78
CT96F	4-m	Loral 3K	KPGL-3	90°	3693 – 7369	1.222	0.51

**Note.** — Run ID names encode the observatory (CT=CTIO, KP=KPNO), the year of the observations (e.g., 94 = 1994), and the observing semester (F=Fall, S=Spring).

**Table 6**  
Redshift Catalog

Galaxy ID	R.A. (J2000)	Dec. (J2000)	$v_{helio}$ km s <sup>-1</sup>	$v_{err}$ km s <sup>-1</sup>	Tonry R value	Emission Flag	Observing Run ID
A0014-A	00 15 10.98	-23 52 56.2	19280	26	10.12		CT94F
A0027-A	00 24 56.04	-20 43 53.8	16241	47	8.47		KP95F
A0044-A	00 29 31.67	+12 02 59.0	21614	29	11.64		KP94F
A0051-A	00 31 42.11	-23 38 45.9	33064	43	8.87		CT95F
A0051-B	00 31 41.52	-23 38 46.2	33250	53	8.04		CT95F
A0071-A	00 37 58.74	+29 36 12.6	22044	33	12.46		KP94F
A0071-B	00 37 52.72	+29 36 27.5	21436	31	12.67		KP94F
A0074-A	00 38 21.67	-22 20 41.5	19013	46	8.72		CT95F
A0075-B	00 39 28.60	+21 13 46.1	17610	42	10.34		KP95F
A0076-1	00 39 26.32	+06 44 02.5	11297	36	11.07		CT94F KP92F KP94F
A0077-A	00 40 28.35	+29 33 20.9	21424	35	11.69		KP94F
A0077-X	...	...	21577	69	3.79		KP94F
A0085-A	00 41 50.45	-09 18 12.3	16581	56	7.90		KP95F
A0086-A	00 42 42.30	-21 46 28.1	18481	41	9.88		KP95F
A0086-B	00 42 40.00	-21 48 01.3	17639	49	8.16		KP95F
A0087-A	00 43 10.10	-09 51 42.3	15118	41	9.75		KP95F
A0093-A	00 44 00.32	-18 27 54.2	31116	37	10.92		KP94F
A0102-A	00 48 31.23	+01 21 17.1	18946	37	11.39		KP94F
A0114-A	00 54 07.50	-21 42 51.4	17290	45	8.77		KP95F
A0116-A	00 55 46.44	+00 38 41.9	20100	42	10.94		KP95F
A0117-A	00 55 51.89	-09 59 08.5	16453	47	9.75		KP95F
A0119-1	00 56 16.13	-01 15 22.1	13357	39	10.63		CT94F KP94F KP92F
A0126-A	01 00 15.94	-14 12 37.4	11456	33	9.96		KP94F
A0126-B	00 59 53.92	-14 14 40.7	16448	39	11.00		KP94F
A0133-A	01 02 41.73	-21 52 55.2	17041	50	8.30		KP95F
A0134-A	01 02 39.08	-02 41 46.3	20639	31	12.96		KP94F
A0147-1	01 08 37.90	+02 16 06.1	13167	55	8.31		KP95F KP92F
A0150-A	01 09 18.44	+13 10 07.5	17754	38	11.43		KP95F
A0151-A	01 08 51.11	-15 24 25.8	15936	49	9.26		KP95F
A0152-A	01 10 03.23	+13 58 40.2	17491	35	11.03		KP95F
A0154-A	01 11 03.54	+17 39 06.3	18236	39	10.86		KP94F
A0158-A	01 11 45.30	+16 53 10.2	18958	38	11.47		KP95F
A0160-1	01 12 59.76	+15 29 29.3	13147	36	10.23		KP94F
A0161-A	01 15 22.39	+37 20 22.6	22185	45	8.94		KP95F
A0168-A	01 14 57.70	+00 25 52.1	13555	54	8.46		KP95F KP92F
A0170-A	01 15 53.94	+13 11 12.5	9843	30	12.72		KP95F
A0171-A	01 17 17.96	+16 15 54.9	20718	45	10.20		KP95F
A0174-A	01 20 16.25	+35 48 25.9	22490	43	9.26		KP95F
A0179-D	01 22 10.86	+19 37 13.9	15618	39	11.30		KP95F
A0189-1	01 23 26.33	+01 42 17.8	10210	33	11.06		CT94F KP94F CT96F
A0193-1	01 25 07.54	+08 41 57.0	14654	61	8.06		KP94F CT96F CT94F
A0194-1	01 25 58.84	-01 20 21.8	5303	38	9.54		CT94F CT96F KP94F
A0194-1a	...	...	5468	33	8.74		CT94F
A0195-1	01 26 54.75	+19 12 50.1	12943	52	8.53		KP95F KP92F
A0208-A	01 31 32.96	+00 33 21.0	23802	41	10.06		KP95F
A0225-A	01 38 49.03	+18 49 30.2	20819	41	9.96		KP95F
A0237-A	01 40 43.02	+00 18 54.0	25203	27	...	E	KP95F
A0237-D	01 40 49.19	+00 05 25.6	25190	41	8.23		KP95F
A0240-A	01 42 06.06	+07 39 52.6	18253	36	11.51		KP95F
A0245-B	01 44 08.19	+06 18 58.3	23391	34	10.08		KP94F
A0246-A	01 44 43.48	+05 48 42.8	22691	51	8.12		KP95F
A0257-A	01 49 08.43	+13 57 46.3	21143	42	9.84		KP94F
A0260-A	01 50 42.96	+33 04 54.8	10647	40	9.78		KP92S KP95F
A0261-1	01 51 26.48	-02 15 11.5	13974	43	10.90		KP95F KP92F
A0262-1	01 52 46.28	+36 09 05.3	4824	50	8.00		KP92S KP95F
A0267-A	01 53 15.22	+01 02 19.5	17963	34	10.49		KP94F
A0268-A	01 52 49.24	-01 00 06.5	17917	29	13.09		KP94F
A0271-A	01 54 06.73	+01 39 52.9	24814	31	12.06		KP94F
A0279-A	01 56 16.96	+01 03 02.5	23680	34	12.05		KP94F
A0292-A	02 02 18.94	+19 04 00.7	19423	48	8.78		KP95F
A0295-1	02 02 17.24	-01 07 40.6	12813	56	8.00		KP92F
A0303-B	02 06 33.60	-03 23 48.8	17416	24	...	E	KP95F
A0311-A	02 09 28.48	+19 46 33.8	19580	43	9.33		KP94F
A0326-A	02 13 39.75	-07 08 43.0	17066	56	6.55		KP95F
A0347-1	02 25 26.47	+41 49 27.1	5229	41	9.38		KP95F
A0357-A	02 29 27.65	+13 15 57.9	16948	48	7.99		KP92S KP95F KP92F
A0358-A	02 29 58.96	-13 15 53.6	16951	41	9.40		KP95F
A0376-1	02 46 04.04	+36 54 16.7	14562	41	9.91		KP94F
A0386-A	02 50 02.29	-17 02 54.3	17835	34	12.71		KP95F KP92F
A0386-B	02 50 04.25	-17 12 35.3	36376	41	9.62		KP94F
A0396-B	02 57 33.45	+41 30 59.1	4911	34	11.43		KP94F
A0396-C	02 57 08.91	+41 30 59.5	6343	36	10.40		KP94F KP95F
A0397-1	02 56 28.91	+15 54 58.9	10383	45	9.19		KP95F KP92F
A0399-A	02 57 53.17	+13 01 49.8	21415	49	7.87		KP94F

Table 6 — *Continued*

Galaxy ID	R.A. (J2000)	Dec. (J2000)	$v_{helio}$ km s <sup>-1</sup>	$v_{err}$ km s <sup>-1</sup>	Tonry R value	Emission Flag	Observing Run ID
A0401-A	02 58 57.84	+13 34 57.2	22215	58	7.12		KP95F
A0404-A	03 01 34.79	+41 29 14.2	18420	34	12.12		KP95F
A0404-B	03 02 06.80	+41 35 36.8	9140	49	7.56		KP95F
A0407-I	03 01 51.60	+35 50 27.4	14376	35	11.97		KP95F
A0415-A	03 06 52.80	-12 06 22.7	23588	53	7.14		KP95F
A0419-1	03 08 15.84	-23 41 29.0	20392	48	5.81		KP92S
A0419-2	03 08 28.73	-23 36 53.2	12246	43	7.99		KP92S KP95F
A0423-A	03 11 17.28	-12 07 42.1	23435	49	8.13		KP95F
A0423-X	...	...	24337	40	10.23		KP95F
A0428-A	03 16 12.53	-19 04 55.9	19908	42	9.09		KP95F
A0428-B	03 16 16.65	-19 05 00.1	20420	38	9.94		KP95F
A0436-A	03 26 35.35	+09 11 02.9	19061	51	7.97		KP94F
A0436-C	03 27 07.91	+09 11 20.0	19459	40	9.16		KP94F
A0450-A	03 40 55.40	+23 35 31.9	17685	51	8.05		KP95F
A0484-D	04 15 49.25	-07 41 20.5	20670	59	6.62		KP95F
A0496-1	04 33 37.68	-13 15 39.7	9830	56	3.59		CT96F KP95F
A0497-A	04 37 36.01	+10 40 40.7	28189	51	7.41		KP95F
A0497-B	04 37 29.37	+10 39 37.0	26842	45	7.88		KP95F
A0498-A	04 37 50.79	+21 12 19.0	17399	55	6.93		KP94F
A0500-A	04 38 52.55	-22 06 39.6	20340	48	9.79		KP95F
A0505-A	04 59 56.06	+80 10 42.3	16017	47	9.65		KP94F
A0514-A	04 47 06.51	-20 28 52.0	21359	49	8.96		KP95F
A0524-F	04 57 51.00	-19 42 29.1	22914	48	8.12		KP95F
A0533-1	05 01 08.25	-22 34 58.1	14380	45	8.69		KP92S CT96F KP95F KP92F
A0533-X	...	...	15899	62	6.11		KP95F
A0536-A	05 07 44.52	-09 15 27.0	44295	45	9.16		KP94F
A0539-1	05 16 55.12	+06 33 09.5	9707	43	10.46		KP92S KP95F KP92F
A0548-B	05 49 21.74	-25 20 47.0	11867	37	9.40		KP92S KP95F
A0550-A	05 52 51.12	-21 03 04.5	29829	54	7.98		KP95F
A0553-A	06 12 41.21	+48 35 43.8	20323	42	10.71		KP94F
A0555-B	06 17 33.37	-17 15 25.3	29742	62	3.87		CT94S
A0559-A	06 39 33.00	+69 51 53.7	23310	37	10.22		KP95F
A0564-A	07 00 40.43	+69 54 24.8	23188	34	10.09		KP94F
A0568-A	07 07 41.58	+35 03 29.6	23496	48	8.01		KP94F
A0569-1	07 09 07.76	+48 36 55.3	5839	46	8.59		KP95F KP93S
A0576-A	07 22 06.83	+55 52 29.3	12093	34	10.42		KP92S KP95F
A0582-A	07 28 00.83	+41 55 06.5	17517	36	12.38		KP94S KP94F
A0592-A	07 42 43.49	+09 22 05.8	18833	30	14.64		KP94F
A0592-C	07 42 52.99	+09 16 51.2	18697	35	13.36		KP94F
A0595-A	07 48 36.83	+52 13 19.1	19282	36	12.04		KP94F
A0595-B	07 49 27.35	+52 02 31.7	20514	37	11.44		KP94F
A0600-A	07 56 35.81	+63 44 23.0	23302	34	10.08		KP94F
A0607-A	07 57 37.11	+39 20 17.8	29448	30	12.03		KP94F
A0612-A	08 01 05.49	+34 49 39.2	46215	70	6.39		KP94F
A0634-A	08 15 44.90	+58 19 15.8	8143	39	9.67		KP92S KP94S KP95F
A0644-A	08 17 25.65	-07 30 46.2	21176	43	6.00		CT94S
A0644-B	08 17 54.50	-07 26 56.2	21191	37	7.26		CT94S
A0695-A	08 41 13.13	+32 24 57.9	20560	84	4.71		KP94S
A0757-A	09 13 07.82	+47 42 29.5	15415	40	10.91		KP95F KP94S
A0779-1	09 19 46.80	+33 44 58.7	6897	44	10.39		KP93S KP94F KP94S KP95F
A0780-A	09 18 05.71	-12 05 43.9	16275	79	2.07		KP94S CT95S KP94S
A0834-A	09 41 32.94	+66 42 37.8	21307	50	7.34		KP95F
A0834-C	09 40 19.60	+66 38 41.9	17919	46	8.83		KP95F
A0838-A	09 37 09.76	-05 02 28.7	15068	42	8.51		CT95S
A0838-B	09 37 08.63	-05 02 30.1	15668	39	9.90		CT95S
A0841-A	09 38 36.01	-04 20 06.9	20838	34	8.29		CT94S
A0841-B	09 38 33.10	-04 19 35.4	21135	40	6.45		CT94S
A0842-A	09 37 34.04	-20 51 34.8	10426	22	11.29		CT94S
A0912-1	10 01 09.41	-00 04 46.5	13580	24	11.27		KP92S CT94F CT94S
A0912-G1	...	...	28355	56	3.38		KP92S
A0957-1	10 13 38.27	-00 55 31.3	13391	58	7.83		CT95S KP93S
A0970-D	10 18 17.98	-10 46 46.6	11927	20	13.89		CT94S
A0978-A	10 20 26.57	-06 31 37.1	16216	42	9.84		CT95S KP94S
A0979-A	10 20 19.30	-07 53 37.5	15907	39	10.24		CT95S
A0993-A	10 21 55.96	-04 53 25.8	16300	52	8.35		KP96S
A0994-A	10 22 37.82	+19 23 47.3	11826	43	10.04		KP96S
A0999-1	10 23 23.85	+12 50 05.8	9749	35	10.67		KP92S CT95S KP94S
A1003-A	10 25 01.67	+47 50 29.7	19153	40	11.77		KP96S
A1016-1	10 27 07.91	+11 00 36.9	9713	38	10.06		KP92S CT95S KP94S
A1020-A	10 27 49.60	+10 26 29.7	19612	40	10.99		KP94S KP96S
A1021-A	10 29 25.23	+37 37 47.1	30891	42	10.90		KP96S
A1021-D	10 29 16.99	+37 35 37.9	15116	78	3.61		KP96S
A1032-A	10 30 10.20	+04 00 24.3	19823	40	10.07		KP96S
A1060-1	10 36 42.56	-27 31 42.9	3862	41	7.82		CT94F CT94S KP93S
A1066-A	10 39 38.86	+05 10 30.5	21216	42	9.97		KP96S KP94S
A1100-1	10 48 45.73	+22 13 03.4	13981	35	8.82		KP92S

Table 6 — *Continued*

Galaxy ID	R.A. (J2000)	Dec. (J2000)	$v_{helio}$ km s <sup>-1</sup>	$v_{err}$ km s <sup>-1</sup>	Tonry R value	Emission Flag	Observing Run ID
A1139-1	10 58 11.02	+01 36 15.4	11515	29	11.06		KP92S CT94S
A1142-2	11 00 45.39	+10 33 11.6	10138	39	10.47		KP93S
A1149-A	11 02 57.62	+07 36 11.2	21247	35	11.83		KP94S
A1169-A	11 07 49.44	+43 54 59.6	17532	36	11.64		KP96S KP94S
A1171-E	11 07 29.99	+02 54 36.4	22666	38	9.31		KP96S
A1177-1	11 09 44.52	+21 45 31.5	9561	26	12.18		KP92S
A1179-B	11 10 19.87	+23 58 00.1	31861	35	12.73		KP96S
A1190-A	11 11 43.67	+40 49 13.9	23489	36	10.67		KP96S
A1203-A	11 13 48.25	+40 17 08.0	22655	38	10.04		KP96S
A1213-1	11 16 22.87	+29 15 08.1	13535	35	8.90		KP92S
A1257-2	11 25 31.10	+35 30 15.3	10175	39	9.73		KP93S
A1267-1	11 28 36.40	+26 54 19.4	9795	39	9.55		KP93S
A1270-A	11 28 42.09	+54 10 19.3	21151	37	10.65		KP96S
A1279-A	11 31 39.57	+67 14 29.1	16263	50	8.45		KP96S KP94S
A1308-1	11 33 05.09	-04 00 49.8	15535	41	9.41		KP92S CT95S
A1314-1	11 34 49.42	+49 04 38.3	10008	42	10.56		KP92S KP94S
A1317-A	11 35 13.06	-13 33 07.0	21632	40	10.60		KP96S
A1318-A	11 37 34.35	+54 51 10.3	17335	37	11.90		KP96S
A1318-B	11 36 03.63	+55 04 30.4	17155	33	12.58		KP96S
A1334-A	11 39 03.75	-04 19 03.6	16882	49	8.07		CT95S
A1344-A	11 40 53.03	-10 43 25.7	23213	46	8.78		KP94S KP96S
A1347-A	11 41 24.31	-25 23 31.6	29585	42	8.37		CT95S
A1365-D	11 44 30.57	+30 52 59.3	22904	41	9.41		KP96S
A1367-1	11 44 02.17	+19 56 58.7	6279	46	9.39		KP94S KP93S
A1367-X	...	...	6355	40	9.47		KP94S
A1371-A	11 45 18.97	+15 29 12.3	20348	45	8.77		KP96S
A1375-A	11 46 03.76	-08 16 15.8	22338	50	7.50		CT95S
A1375-B	11 46 03.96	-08 15 54.7	23751	52	7.20		CT95S
A1377-B	11 47 21.46	+55 43 46.8	15457	36	12.78		KP96S
A1404-A	11 52 12.44	-02 48 18.1	23182	46	7.86		CT95S
A1424-A	11 57 29.04	+05 05 20.0	23149	43	9.35		KP96S KP94S
A1424-C	11 57 34.38	+05 05 50.9	23937	43	8.14		KP96S
A1436-A	12 00 14.24	+56 15 00.5	19474	34	11.85		KP96S
A1436-I	11 59 26.47	+56 24 13.0	18889	36	12.56		KP96S
A1452-A	12 03 28.42	+51 42 55.0	18229	37	12.37		KP96S
A1461-A	12 04 24.84	+42 33 41.3	16185	39	11.09		KP96S KP94S
A1474-A	12 08 07.79	+15 03 21.2	25566	37	9.86		KP96S
A1520-A	12 19 35.05	-13 26 12.3	21260	30	9.52		CT94S
A1526-F	12 21 43.87	+13 45 14.5	24529	44	9.39		KP96S
A1534-A	12 24 42.93	+61 28 13.9	21009	41	10.00		KP96S KP94S
A1569-A	12 36 08.20	+16 38 27.8	23596	48	8.44		KP94S KP96S
A1625-A	12 51 33.90	-20 39 23.8	19000	38	8.49		CT95S
A1625-C	12 51 33.79	-20 39 33.9	18960	45	7.01		CT95S
A1630-A	12 51 53.50	+04 34 46.4	19355	47	9.53		KP96S
A1631-1	12 52 52.51	-15 24 47.5	4053	26	13.40		KP92S
A1631-A	12 53 18.20	-15 31 58.0	14278	30	10.55		KP92S CT94S
A1644-1	12 57 11.76	-17 24 35.0	14267	49	6.84		KP92S
A1648-A	12 58 51.73	-26 38 57.1	23462	53	7.42		CT95S
A1648-B	12 58 56.63	-26 37 35.1	22664	58	5.31		CT95S
A1656-1	13 00 08.04	+27 58 36.3	6499	50	9.39		KP96S KP93S KP94S
A1691-A	13 11 08.72	+39 13 36.0	21686	36	11.57		KP94S KP96S
A1709-A	13 18 30.39	-21 26 29.9	15429	45	8.92		CT95S
A1736-1	13 27 28.04	-27 19 27.6	13608	65	7.47		KP93S
A1741-A	13 24 26.42	+71 24 19.8	22650	42	8.56		KP96S
A1749-A	13 29 21.05	+37 37 21.6	16881	42	11.02		KP94S KP96S
A1773-A	13 42 09.70	+02 13 37.1	23232	49	8.81		KP96S KP94S
A1775-A	13 41 49.22	+26 22 24.9	22616	39	10.17		KP96S
A1780-A	13 44 32.63	+02 57 13.7	23259	42	9.06		KP96S
A1780-B	13 44 40.62	+02 51 41.7	23351	51	8.15		KP96S
A1783-B	13 42 47.69	+55 31 16.0	10584	28	12.76		KP96S
A1794-A	13 50 23.29	-26 22 24.6	37683	49	4.82		CT94S
A1794-B	13 50 23.59	-26 23 03.9	38352	56	4.25		CT94S
A1800-A	13 49 23.61	+28 06 25.3	22554	42	9.80		KP96S
A1802-B	13 51 20.21	-26 45 03.1	28562	47	5.74		CT94S
A1802-D	13 51 22.42	-26 45 14.5	29302	53	3.26		CT94S
A1827-A	13 58 06.14	+21 40 20.0	19917	39	11.20		KP96S
A1827-B	13 58 09.60	+21 41 51.2	19817	42	10.87		KP96S
A1831-A	13 59 15.15	+27 58 33.6	22777	41	10.22		KP96S
A1836-1	14 01 41.84	-11 36 22.7	11271	47	8.00		CT94S KP93S
A1837-A	14 01 36.43	-11 07 43.4	20713	42	9.27		CT94S KP94S
A1846-D	14 03 16.72	-25 28 27.8	6789	47	7.12		KP96S
A1846-E	14 03 19.25	-25 17 40.8	19325	48	7.48		KP96S
A1873-B	14 11 36.38	+28 12 56.7	21758	39	10.53		KP96S
A1873-D	14 11 30.51	+28 10 14.5	22983	44	9.31		KP96S
A1890-A	14 17 37.85	+08 10 45.2	17569	42	10.79		KP96S
A1890-B	14 17 31.33	+08 12 29.2	17079	37	10.76		KP96S

Table 6 — *Continued*

Galaxy ID	R.A. (J2000)	Dec. (J2000)	$v_{helio}$ km s <sup>-1</sup>	$v_{err}$ km s <sup>-1</sup>	Tony R value	Emission Flag	Observing Run ID
A1899-A	14 21 41.78	+17 45 07.3	16445	39	11.13		KP96S
A1913-A	14 27 17.15	+16 49 50.7	15452	39	11.47		KP96S
A1964-A	14 46 35.58	-08 46 06.7	21313	44	6.67		CT94S
A1964-Ax	...	...	21169	37	6.65		CT94S
A1983-1	14 52 43.25	+16 54 12.9	13829	39	10.32		KP93S
A1991-A	14 54 31.54	+18 38 31.3	17752	48	8.52		KP94S KP96S
A1996-A	14 57 31.52	-23 55 29.7	33895	58	7.78		CT95S
A1996-C	14 57 33.62	-23 55 12.2	34404	50	7.01		CT95S
A2004-E	14 58 26.61	+24 58 14.7	19290	24	...	E	KP96S
A2020-F	15 04 25.72	+07 49 28.5	14703	43	10.41		KP96S
A2025-A	15 06 44.54	+34 28 22.8	33424	62	9.99		KP96S
A2029-A	15 10 56.09	+05 44 40.0	23399	58	8.15		KP96S KP94S
A2040-1	15 12 47.74	+07 26 02.0	13734	47	9.30		KP93S
A2052-1	15 16 44.55	+07 01 16.8	10314	14	...	E	KP93S
A2055-B	15 19 13.18	+06 07 49.5	13566	35	10.76		KP96S
A2063-1	15 23 05.46	+08 36 33.2	10269	36	10.51		KP93S
A2065-A	15 22 24.12	+27 42 50.8	20740	41	10.49		KP94S KP96S
A2067-A	15 23 26.86	+31 03 57.3	22425	39	10.05		KP96S
A2079-A	15 27 45.20	+28 55 42.9	19619	40	10.76		KP94S KP96S
A2089-A	15 32 49.96	+28 02 21.3	22073	46	9.36		KP96S KP94S
A2107-1	15 39 39.05	+21 46 55.7	12611	60	7.39		KP93S
A2124-A	15 44 59.13	+36 06 33.5	19892	42	10.34		KP94S KP96S
A2143-A	15 57 34.95	+37 20 36.1	28179	38	11.02		KP96S
A2147-1	16 02 17.04	+15 58 27.6	10617	42	9.25		KP93S
A2151-1	16 04 35.76	+17 43 18.0	10551	41	9.79		KP94S KP93S
A2152-1	16 05 29.28	+16 26 11.0	13249	59	8.08		KP93S
A2162-1	16 12 35.73	+29 29 03.5	9581	44	9.92		KP96S KP93S
A2168-F	16 12 51.19	+54 08 00.2	18678	67	4.72		KP96S
A2169-A	16 13 58.20	+49 11 21.8	18012	30	14.90		KP96S
A2184-A	16 21 05.07	+50 13 20.2	16017	38	11.54		KP96S
A2197-1	16 29 45.04	+40 48 42.5	8826	43	9.58		KP96S KP93S KP94S
A2198-B	16 27 55.37	+43 56 52.8	17485	32	12.63		KP96S
A2199-1	16 28 38.45	+39 33 03.0	9318	85	4.44		KP96S KP93S KP94S
A2199-A	...	...	9232	134	2.30		KP96S
A2247-1	16 52 48.08	+81 37 57.9	11133	64	6.11		KP96S KP93S
A2250-A	17 10 56.33	+39 41 30.7	18666	34	12.96		KP96S
A2250-B	17 11 01.32	+39 41 25.0	19721	40	10.90		KP96S
A2256-A	17 03 35.66	+78 37 43.5	16699	55	8.48		KP96S
A2256-C	17 04 13.21	+78 37 41.0	16818	39	11.37		KP96S
A2271-A	17 18 16.71	+78 01 05.4	16962	45	9.94		KP96S
A2293-A	18 01 21.50	+57 39 02.0	21198	38	10.60		KP96S
A2293-B	18 02 17.08	+57 32 52.8	21151	35	10.70		KP96S
A2293-F	18 00 56.63	+57 38 09.5	19997	58	5.79		KP96S
A2293-H	18 01 10.57	+57 38 39.6	21756	73	2.76		KP96S
A2295-B	18 00 33.64	+69 13 18.0	24912	40	9.97		KP96S
A2295-F	18 00 36.25	+69 14 23.0	30529	44	9.52		KP96S
A2296-A	17 54 31.97	+77 42 20.9	12050	47	7.81		KP96S
A2308-A	18 34 08.60	+70 57 18.8	23970	39	9.48		KP96S
A2309-A	18 39 07.09	+77 50 22.2	15393	49	9.26		KP96S
A2319-A	19 21 10.20	+43 56 42.7	16379	54	7.80		KP95F
A2325-A	20 30 06.18	-24 59 01.2	24129	51	7.39		CT95F
A2325-B	20 30 04.98	-24 58 54.8	23947	50	6.42		CT95F
A2331-A	20 58 12.17	-07 45 35.6	23681	44	8.40		KP95F
A2360-A	21 37 07.67	-15 05 28.5	63030	57	6.93		KP95F
A2360-J	21 37 44.14	-15 06 01.3	26604	43	7.67		KP95F
A2361-A	21 39 12.45	-14 19 07.5	17924	40	11.26		KP95F
A2362-A	21 40 14.67	-14 13 53.4	18379	35	12.57		KP94F
A2366-A	21 42 48.75	-06 52 07.3	16130	31	14.00		KP94F
A2370-A	21 44 23.98	-19 26 27.5	17728	36	10.83		KP94F
A2372-A	21 45 15.54	-19 59 40.8	17623	39	10.82		KP95F
A2381-A	21 51 26.16	+02 26 50.2	8034	31	11.75		KP94F
A2382-A	21 51 55.67	-15 42 22.7	19704	40	9.73		KP94F
A2388-A	21 53 39.32	+08 15 08.8	18202	36	10.47		KP94F
A2399-C	21 57 01.74	-07 50 23.0	18630	35	12.31		KP94F
A2401-A	21 58 22.53	-20 06 16.4	17379	48	8.90		KP95F
A2405-A	21 59 42.25	-17 48 03.3	10961	41	8.76		KP95F
A2405-D	21 58 59.77	-17 52 46.5	28081	42	...	E	KP95F
A2405-I	21 59 45.93	-17 53 42.2	11499	48	...	E	KP95F
A2412-A	22 04 02.45	-21 26 53.7	21963	42	9.18		KP95F
A2415-A	22 05 26.19	-05 44 32.6	17007	31	14.48		KP94F
A2457-A	22 35 40.89	+01 29 04.2	17602	43	10.46		KP95F
A2459-D	22 36 45.69	-15 44 05.0	21822	42	9.51		KP95F
A2462-A	22 39 11.42	-17 20 28.8	22281	53	7.96		KP95F
A2469-A	22 40 34.75	+12 18 41.3	18918	40	9.67		KP95F
A2480-A	22 45 59.07	-17 37 32.8	20450	41	11.12		KP94F
A2492-A	22 50 30.45	-19 14 34.7	20728	39	10.47		KP95F

Table 6 — *Continued*

Galaxy ID	R.A. (J2000)	Dec. (J2000)	$v_{helio}$ km s <sup>-1</sup>	$v_{err}$ km s <sup>-1</sup>	Tonry R value	Emission Flag	Observing Run ID
A2495-A	22 50 19.77	+10 54 11.9	23895	45	8.03		KP95F
A2506-1	22 56 37.54	+13 18 46.7	38521	44	8.55		KP94F
A2511-B	22 58 51.10	-07 34 58.1	23078	51	6.91		KP95F
A2525-A	23 04 02.07	-10 45 06.9	23554	47	8.71		KP95F
A2525-E	23 03 53.28	-10 40 39.2	23501	44	8.22		KP95F
A2558-A	23 12 43.59	+10 21 42.7	19450	38	10.83		KP95F
A2559-A	23 13 02.77	-13 37 24.0	23770	44	8.95		KP95F
A2572-A	23 17 13.54	+18 42 28.2	12175	61	7.43		KP92F
A2589-1	23 23 57.55	+16 46 35.8	12442	57	7.45		KP92F
A2593-1	23 24 20.15	+14 38 50.4	12525	46	9.51		KP92F
A2596-A	23 25 08.22	-23 24 05.0	26829	38	10.12		KP95F
A2596-B	23 25 03.27	-23 23 35.4	26191	48	8.68		KP95F
A2618-A	23 34 05.60	+22 58 58.9	21036	36	12.66		KP94F
A2618-B	23 33 15.99	+22 56 27.3	20790	38	11.33		KP94F
A2622-A	23 35 01.51	+27 22 19.0	18417	38	11.70		KP94F
A2625-I	23 37 49.43	+20 48 32.7	17200	46	8.66		KP95F
A2626-A	23 36 30.63	+21 08 47.7	16559	38	10.51		KP94F
A2630-F	23 38 17.65	+15 40 08.0	19788	39	10.05		KP95F
A2634-1	23 38 29.44	+27 01 49.7	9105	44	10.36		KP94F
A2637-A	23 38 53.40	+21 27 51.8	21283	37	11.57		KP95F
A2637-B	23 38 42.26	+21 30 03.1	21471	43	9.69		KP95F
A2644-A	23 41 07.27	+00 05 41.5	20599	33	13.22		KP94F
A2656-A	23 44 43.33	-04 00 44.2	23034	41	9.51		KP95F
A2657-2	23 44 30.49	+09 15 51.6	12296	59	6.41		KP92F
A2660-A	23 45 15.98	-25 50 08.9	16398	59	7.09		KP95F
A2661-C	23 47 02.88	-10 25 05.9	57163	98	4.12		KP95F
A2665-A	23 50 50.61	+06 08 57.2	16840	57	7.14		KP95F
A2666-1	23 50 58.66	+27 08 47.6	8165	43	9.21		KP95F
A2670-A	23 54 13.68	-10 25 09.4	23290	51	7.56		CT95F
A2670-X1	...	...	21969	52	6.54		CT95F
A2670-X2	...	...	23115	70	4.21		CT95F
A2675-A	23 55 42.66	+11 20 34.5	22168	44	9.35		KP95F
A2676-C	23 55 50.62	+06 05 13.8	17061	51	6.93		KP95F
A2676-D	23 55 33.14	+06 07 26.8	12834	55	...	E	KP95F
A2678-A	23 56 00.34	+11 43 25.8	21475	41	9.23		KP95F
A2690-A	00 00 14.01	-25 11 12.2	25403	32	7.71		CT94F
A2690-B	00 00 13.40	-25 11 08.7	25318	31	7.53		CT94F
A2691-C	00 01 51.72	-03 05 08.2	24212	54	7.12		KP95F
A2716-A	00 03 01.10	-27 08 07.9	20134	78	6.50		KP95F
A2716-E	00 02 30.27	-27 17 47.2	8532	53	5.88		KP95F
A2717-1	00 03 12.77	-35 56 16.7	14853	34	7.80		CT92F
A2731-1	00 09 59.04	-57 01 17.7	9434	33	8.48		CT92F
A2734-A	00 11 21.74	-28 51 17.2	18456	39	7.34		CT94F
A2759-A	00 18 38.90	-30 33 34.1	31962	39	6.21		CT94F
A2759-B	00 18 39.05	-30 33 27.4	31496	40	6.63		CT94F
A2764-D	00 20 35.74	-49 12 47.7	21424	55	7.45		CT95F
A2765-A	00 22 07.23	-20 53 59.3	23078	38	6.91		CT94F
A2771-A	00 24 32.16	-40 07 31.2	20839	40	10.04		CT96F
A2782-A	00 30 16.33	-53 24 50.9	25850	40	5.34		CT94F
A2793-A	00 33 44.94	-82 36 08.6	17498	23	13.17		CT94F
A2793-B	00 33 29.03	-82 36 41.2	17976	65	3.01		CT94F
A2793-H	00 34 03.97	-82 35 38.5	17345	25	8.95		CT94F
A2799-A	00 37 27.62	-39 07 48.4	19015	23	12.85		CT94F
A2800-A	00 37 57.66	-25 04 26.8	18999	24	12.77		CT94F
A2806-1	00 40 12.92	-56 09 15.0	8218	34	7.80		CT92F
A2806-2	00 40 48.47	-56 12 53.4	8188	37	7.45		CT92F
A2810-A	00 41 29.77	-61 04 54.3	17138	26	11.13		CT94F
A2810-B	00 41 25.37	-61 04 49.5	17756	21	12.61		CT94F
A2814-A	00 42 53.75	-28 28 11.7	24468	36	6.97		CT94F
A2816-A	00 45 44.91	-18 14 57.4	17787	38	10.26		KP95F
A2819-B	00 46 05.08	-63 33 19.9	22369	49	7.79		CT95F
A2819-D	00 46 00.48	-63 33 52.4	22383	52	7.08		CT95F
A2824-A	00 48 30.05	-21 21 38.1	18382	39	10.34		KP95F
A2824-B	00 48 36.10	-21 21 55.3	18125	39	9.83		KP95F
A2836-B	00 53 41.81	-47 35 33.3	17312	57	2.96		CT95F
A2836-C	00 53 37.15	-47 36 19.0	22683	51	6.61		CT95F
A2841-A	00 55 04.58	-48 56 18.0	19342	28	10.29		CT94F
A2854-A	01 00 46.72	-50 32 06.0	18209	27	10.86		CT94F
A2854-B	01 00 48.05	-50 32 56.4	18777	33	7.47		CT94F
A2859-A	01 02 12.42	-67 34 52.8	19491	43	9.44		CT96F
A2864-A	01 04 08.32	-66 58 47.7	20948	47	7.93		CT96F
A2870-1	01 07 41.84	-46 54 31.2	6728	45	5.58		CT92F
A2877-1	01 09 54.82	-45 55 57.3	7226	57	6.46		CT92F CT95F
A2881-3	01 11 14.14	-17 04 14.5	13253	43	9.97		CT94F KP94F KP92F
A2889-A	01 14 29.96	-48 28 27.0	6978	34	6.30		CT94F
A2896-1	01 18 18.60	-37 06 17.0	9473	28	9.20		CT92F

Table 6 — *Continued*

Galaxy ID	R.A. (J2000)	Dec. (J2000)	$v_{helio}$ km s <sup>-1</sup>	$v_{err}$ km s <sup>-1</sup>	Tonry R value	Emission Flag	Observing Run ID
A2911-A	01 24 44.69	-38 07 42.3	5791	29	8.25		CT92F
A2911-B	01 25 12.19	-38 05 38.0	5931	28	8.44		CT92F
A2913-A	01 28 03.88	-34 06 58.2	40278	40	6.71		CT94F
A2923-A	01 32 21.45	-31 05 33.0	21376	37	10.45		CT96F
A2923-X	...	...	21188	50	6.85		CT96F
A2955-A	01 57 01.88	-17 01 23.8	28311	38	10.46		KP94F
A2992-A	02 14 51.01	-26 39 36.4	17389	21	13.50		CT94F
A3004-A	02 18 51.93	-47 59 58.1	19866	20	13.22		CT94F
A3009-A	02 22 07.32	-48 33 52.2	19754	26	11.50		CT94F
A3027-A	02 29 55.93	-33 10 40.4	23761	38	9.51		CT96F
A3045-A	02 43 41.29	-51 27 41.3	22623	41	6.85		CT94F
A3047-A	02 45 13.41	-46 27 20.1	28321	54	4.86		CT94F
A3052-A	02 47 00.16	-27 31 55.0	20155	17	14.68		CT94F
A3059-A	02 51 01.20	-46 18 57.2	26300	39	6.40		CT94F
A3074-B	02 58 11.34	-52 43 43.2	21790	44	8.70		CT96F
A3077-C	03 00 26.88	-51 22 58.1	25511	29	7.20		CT94F
A3078-A	03 00 25.55	-51 50 50.9	21771	28	9.74		CT94F
A3089-B	03 08 16.98	-36 42 31.7	19524	33	11.49		CT95F
A3089-X1	...	...	20470	76	4.35		CT95F
A3094-A	03 11 25.06	-26 55 53.5	20577	31	9.46		CT94F
A3095-A	03 12 26.62	-27 08 25.0	19468	41	9.54		CT95F
A3098-A	03 13 43.53	-38 18 13.4	25398	32	8.08		CT94F
A3098-B	03 13 42.76	-38 17 52.0	23895	33	7.84		CT94F
A3100-A	03 13 52.84	-47 47 34.7	18624	25	11.65		CT94F
A3104-A	03 14 21.84	-45 25 14.0	21791	35	8.58		CT94F
A3106-A	03 14 29.91	-58 05 48.5	19523	38	9.91		CT96F
A3106-C	03 14 33.17	-58 05 47.8	19595	45	7.32		CT96F
A3107-B	03 16 06.24	-42 45 12.3	19833	26	11.46		CT94F
A3107-X	...	...	19612	22	11.63		CT94F
A3109-A	03 16 39.42	-43 51 17.0	18608	32	9.23		CT94F
A3110-A	03 16 12.40	-50 57 12.1	22249	33	9.04		CT94F
A3111-A	03 17 45.17	-45 45 20.7	23044	47	5.86		CT94F
A3112-A	03 17 57.73	-44 14 17.5	22777	56	4.48		CT94F
A3112-XN	...	...	22406	33	6.45		CT94F
A3112-XS	...	...	22728	50	5.98		CT94F
A3120-A	03 21 56.48	-51 19 36.6	21413	44	8.46		CT96F
A3122-A	03 22 20.39	-41 21 46.2	19245	36	11.36		CT95F
A3122-B	03 22 18.23	-41 19 41.5	20130	45	9.30		CT95F
A3123-A	03 22 54.82	-52 01 49.2	18278	48	8.84		CT96F
A3125-B	03 27 54.79	-53 22 18.0	17444	37	10.18		CT96F
A3128-B	03 30 38.42	-52 37 12.2	17693	39	10.40		CT96F
A3133-A	03 32 06.05	-45 55 48.0	21377	67	4.69		CT95F
A3135-B	03 34 06.74	-38 59 34.7	18316	47	7.99		CT96F
A3142-A	03 36 37.47	-39 47 41.1	20068	30	12.59		CT96F
A3142-B	03 36 44.30	-39 48 04.9	30996	76	5.43		CT96F
A3142-X	...	...	20314	37	8.67		CT96F
A3144-1	03 37 04.88	-55 01 20.8	13205	28	9.86		CT92F
A3151-A	03 40 27.04	-28 40 37.8	20274	52	7.99		KP95F
A3151-B	03 40 25.31	-28 40 39.2	20403	39	10.34		KP95F
A3152-A	03 40 24.82	-32 34 48.4	28540	37	7.05		CT94F
A3152-X	03 40 24.11	-32 34 08.2	28528	36	5.66		CT94F
A3153-A	03 41 03.76	-34 15 17.2	36887	41	6.42		CT94F
A3153-D	03 41 01.78	-34 15 20.2	36722	48	4.72		CT94F
A3154-A	03 41 56.83	-32 03 30.7	29042	38	9.48		CT96F
A3154-B	03 42 27.05	-32 01 42.5	12127	34	9.53		CT96F
A3158-C	03 43 29.93	-53 41 32.6	18766	40	10.60		CT96F
A3161-A	03 44 44.48	-35 41 03.1	1622	69	4.03		CT96F
A3164-A	03 45 46.96	-57 02 08.8	17823	47	9.06		CT96F
A3173-B	03 49 20.98	-33 46 30.3	35284	35	6.30		CT94F
A3183-G	03 54 08.76	-31 57 31.3	21881	30	8.26		CT94F
A3188-K	03 57 23.66	-27 07 16.8	19316	22	11.90		CT94F
A3193-1	03 58 13.54	-52 19 44.4	10103	31	8.84		CT92F
A3195-A	03 58 54.92	-35 18 09.3	22525	32	8.34		CT94F
A3202-2	03 59 29.13	-53 38 22.6	21097	38	9.84		CT96F
A3223-A	04 08 32.63	-30 49 20.3	17923	29	11.93		CT94F
A3223-D	04 08 33.33	-30 48 38.1	18685	36	7.91		CT94F
A3225-A	04 09 05.96	-59 37 21.9	15386	38	10.06		CT96F
A3225-B	04 09 37.10	-59 35 30.7	16994	33	11.27		CT96F
A3229-A	04 11 13.93	-62 42 54.1	5075	29	8.92		CT94F
A3229-B	04 10 39.15	-62 43 34.1	4955	20	11.72		CT94F
A3231-A	04 11 59.58	-64 36 25.2	46480	46	8.98		CT96F
A3231-B	04 11 15.70	-64 32 08.1	23152	39	8.88		CT96F
A3234-C	04 13 23.43	-45 48 43.8	37054	54	4.70		CT94F
A3241-A	04 15 59.66	-64 46 48.4	19600	26	11.02		CT94F
A3242-A	04 17 51.99	-63 40 31.7	5236	29	10.19		CT94F
A3242-B	04 15 59.41	-63 37 14.1	14377	20	12.56		CT94F

Table 6 — *Continued*

Galaxy ID	R.A. (J2000)	Dec. (J2000)	$v_{helio}$ km s <sup>-1</sup>	$v_{err}$ km s <sup>-1</sup>	Tony R value	Emission Flag	Observing Run ID
A3256-A	04 27 50.55	-36 04 11.9	14253	22	12.19		CT94F
A3266-A	04 31 13.58	-61 27 13.1	18042	21	13.80		CT94F
A3266-B	04 31 16.96	-61 30 07.2	15833	23	13.11		CT94F
A3269-B	04 32 28.99	-32 26 51.9	15995	20	12.53		CT94F
A3301-A	05 00 49.30	-38 40 28.2	16297	23	12.93		CT94F
A3323-A	05 11 22.73	-28 59 32.6	19226	49	8.24		KP95F
A3332-A	05 16 35.08	-42 12 10.6	23954	45	6.45		CT94F
A3336-A	05 21 30.77	-40 49 02.2	23900	34	7.80		CT94F
A3341-A	05 25 35.27	-31 36 07.2	11024	30	9.69		CT94F
A3351-B	05 32 03.63	-38 27 31.5	28263	39	9.51		CT96F
A3351-X	...	...	28303	44	7.44		CT96F
A3358-C	05 38 13.98	-20 37 50.5	27452	56	8.07		KP95F
A3367-1	05 49 41.71	-24 32 43.7	13456	52	7.43		KP95F KP92F
A3370-A	05 54 51.38	-32 19 35.4	27991	39	6.63		CT94F
A3372-A	05 55 22.96	-34 51 34.3	24656	52	7.49		CT96F
A3372-B	05 55 36.67	-34 55 41.8	24382	46	5.36		CT96F
A3374-1	05 56 42.97	-21 15 12.4	14237	62	5.66		KP92F
A3374-1E	...	...	64	41	7.56		KP95F
A3374-1F	...	...	78	29	11.16		KP95F
A3376-1	06 00 41.01	-40 02 46.6	13829	30	9.07		CT92F
A3379-C	06 06 07.94	-42 17 15.9	24548	39	5.74		CT94S
A3380-A	06 06 58.19	-49 29 36.4	15692	34	11.84		CT96F
A3380-C	06 06 52.72	-49 29 43.9	15611	39	9.70		CT96F
A3381-1	06 09 53.76	-33 35 34.1	11494	27	9.17		CT92F
A3385-A	06 17 50.69	-52 01 14.7	37434	71	3.66		CT94S
A3385-B	06 17 41.04	-52 01 06.8	36225	53	5.60		CT94S
A3385-X	...	...	36990	54	4.50		CT94S
A3389-1	06 22 21.30	-64 56 04.6	8248	33	7.83		CT92F
A3389-2	06 21 26.41	-64 59 37.1	8021	36	7.59		CT92F
A3390-A	06 24 39.81	-37 20 09.4	9283	43	8.65		CT96F
A3391-A	06 26 20.40	-53 41 36.1	16522	43	10.01		CT96F
A3391-B	06 26 18.56	-53 41 33.6	16034	43	10.11		CT96F
A3392-A	06 27 06.67	-35 29 16.6	16379	33	8.74		CT94F
A3395-1	06 27 36.42	-54 27 01.7	14605	30	9.78		CT94F CT92F CT94S
A3397-A	06 29 40.23	-52 14 18.5	22704	34	8.05		CT94F
A3403-A	06 41 49.63	-50 00 15.4	36700	47	5.88		CT94F
A3404-A	06 45 29.60	-54 13 38.0	48837	52	8.08		CT96F
A3407-A	07 04 59.29	-49 05 00.5	11780	48	6.30		CT94F
A3408-A	07 08 29.66	-49 12 49.2	12483	44	8.76		CT96F
A3408-B	07 08 11.40	-49 09 53.5	12610	40	8.88		CT96F
A3420-A	09 32 06.97	-24 49 04.3	18973	21	15.08		CT94S
A3428-A	09 52 50.72	-33 44 32.0	2601	23	...	E	KP96S
A3429-A	09 59 24.61	-24 58 15.9	14044	42	8.69		CT95S
A3432-A	10 01 25.16	-33 01 27.5	20598	30	9.10		CT94S
A3432-F	10 01 29.52	-33 02 38.6	20468	37	5.09		CT94S
A3436-A	10 04 38.39	-31 41 07.6	2994	9	...	E	CT94S CT95S
A3455-A	10 52 23.35	-34 12 16.4	28958	53	4.67		CT94S
A3474-A	11 16 27.14	-43 25 03.1	27065	47	5.34		CT94S
A3474-B	11 15 51.06	-43 19 10.7	28112	47	5.84		CT94S
A3488-A	11 40 39.78	-27 45 32.6	25512	44	6.18		CT94S
A3489-A	11 40 55.25	-31 13 40.8	30722	72	6.21		KP96S
A3490-A	11 45 20.16	-34 26 01.8	20417	36	8.66		CT94S
A3494-A	11 57 09.87	-32 09 07.3	20690	39	5.33		CT94S
A3494-F	11 57 04.27	-32 08 54.4	44565	71	3.41		CT94S
A3497-A	12 00 06.16	-31 23 17.3	20489	49	7.91		CT95S
A3500-A	12 02 55.64	-30 07 39.1	13249	20	14.01		CT94S
A3500-D	12 02 15.36	-30 13 23.3	19837	36	4.80		CT95S
A3500-H	12 02 53.68	-30 07 42.5	13037	6	...	E	CT94S
A3501-A	12 03 27.19	-28 37 00.1	2022	98	3.32		CT95S
A3505-A	12 08 42.91	-34 26 36.9	17322	27	10.78		CT94S
A3505-B	12 08 45.97	-34 25 38.3	17546	25	11.83		CT94S
A3507-A	12 12 56.13	-26 03 56.5	24670	46	8.40		CT95S
A3507-D	12 12 54.85	-26 03 20.5	24755	56	6.65		CT95S
A3507-F	12 12 53.28	-26 02 37.1	24047	51	6.38		CT95S
A3509-A	12 16 20.17	-33 16 14.1	17230	23	12.13		CT94S
A3509-B	12 16 18.77	-33 21 57.3	25379	37	6.10		CT94S
A3509-D	12 16 52.75	-33 15 37.8	31658	43	...	E	CT94S
A3515-H	12 23 00.62	-44 35 12.6	32337	67	3.61		CT94S
A3524-A	12 40 03.75	-34 13 31.0	21792	39	7.08		CT94S
A3526-1	12 48 48.94	-41 18 42.0	2904	40	6.44		CT93S
A3528-1	12 54 22.31	-29 00 45.9	16323	82	6.75		KP93S
A3530-1	12 55 36.10	-30 20 49.3	16274	81	6.28		KP93S
A3531-D	12 56 54.13	-33 00 14.0	15055	43	9.19		CT95S
A3532-1	12 57 22.15	-30 21 47.5	16256	34	7.47		CT93S
A3535-A	12 58 04.34	-28 29 52.5	19885	49	7.00		CT95S
A3537-1	13 01 00.71	-32 26 28.9	5073	38	7.69		CT94S CT93S



Table 6 — *Continued*

Galaxy ID	R.A. (J2000)	Dec. (J2000)	$v_{helio}$ km s <sup>-1</sup>	$v_{err}$ km s <sup>-1</sup>	Tonry R value	Emission Flag	Observing Run ID
A3542-1	13 08 41.52	-34 34 31.3	10372	34	7.75		CT93S
A3546-A	13 13 05.98	-29 58 44.1	32075	52	8.07		KP96S
A3548-A	13 13 28.98	-44 04 24.5	16359	58	6.66		CT95S
A3548-B	13 14 00.45	-44 10 41.6	15618	42	9.19		CT95S
A3549-A	13 14 06.20	-29 25 29.7	22408	33	6.09		CT94S
A3552-A	13 18 55.20	-31 49 04.4	15573	25	11.47		CT94S
A3552-F	13 18 53.06	-31 49 15.3	16358	57	3.64		CT94S
A3552-X	...	...	15954	73	3.33		CT94S
A3553-1	13 19 15.08	-37 10 46.5	14551	29	8.88		CT93S
A3554-1	13 19 31.53	-33 29 19.7	14199	34	7.87		CT93S
A3556-1	13 24 06.76	-31 40 15.0	14424	38	7.88		CT93S
A3558-1	13 27 56.53	-31 29 46.8	14036	44	8.71		CT94S KP93S
A3559-1	13 29 51.02	-29 30 53.1	14118	56	8.03		CT95S KP93S
A3559-X	...	...	13806	48	7.05		CT95S
A3560-1	13 31 53.33	-33 14 04.4	3702	38	7.93		CT95S CT93S
A3561-A	13 33 15.81	-42 50 18.1	15457	38	7.18		CT94S
A3562-1	13 33 34.74	-31 40 20.3	14677	38	10.52		CT95S
A3563-B	13 33 48.86	-42 32 34.7	21202	31	9.07		CT94S
A3563-D	13 33 48.09	-42 33 34.7	21203	53	6.18		CT94S
A3563-G	13 33 32.91	-42 26 51.1	19133	33	7.37		CT94S
A3564-1	13 34 55.37	-35 05 57.8	14468	44	8.77		CT95S
A3565-1	13 36 39.06	-33 57 56.7	3754	50	5.29		CT93S
A3567-A	13 39 45.50	-36 26 40.2	36638	67	5.17		CT94S
A3567-D	13 39 37.22	-36 27 13.0	36145	50	4.52		CT94S
A3569-A	13 42 43.71	-35 45 12.7	30191	54	7.15		CT95S
A3569-B	13 42 42.79	-35 46 01.1	29730	56	6.40		CT95S
A3570-2	13 46 24.00	-37 58 15.5	11280	29	9.75		CT93S CT94S
A3571-1	13 47 28.42	-32 51 51.8	11563	44	6.54		CT93S
A3572-1	13 48 14.26	-33 22 57.8	12189	27	11.20		CT93S CT94S
A3574-1	13 49 05.29	-30 17 44.9	4538	40	6.74		CT93S
A3575-1	13 52 38.36	-32 53 17.3	11127	43	7.49		CT95S CT93S
A3577-A	13 54 14.76	-27 50 53.2	14776	49	8.65		CT95S
A3577-B	13 54 17.84	-27 51 12.1	14082	39	8.81		CT95S
A3578-B	13 57 33.09	-24 52 29.8	11651	55	6.41		KP96S
A3581-1	14 07 29.51	-27 01 07.0	6506	66	3.26		CT94S KP93S
A3583-B	14 10 11.05	-22 18 34.6	32105	40	7.13		CT94S
A3584-B	14 10 41.25	-19 59 30.0	42866	53	4.79		CT94S
A3584-H	14 11 26.17	-19 57 12.7	12374	26	9.24		CT94S
A3597-A	14 26 44.29	-19 07 44.2	31283	48	2.10		CT94S CT95S
A3597-B	14 26 42.54	-19 07 49.5	32389	47	5.72		CT95S CT94S
A3599-A	14 27 48.56	-23 32 31.5	7697	44	8.24		CT95S
A3603-A	14 33 38.45	-31 51 16.0	17660	47	7.65		CT95S
A3603-C	14 33 27.54	-31 41 41.1	17327	47	7.46		CT95S
A3603-E	14 33 27.77	-31 42 16.2	18577	48	3.72		CT95S
A3605-A	14 35 04.38	-28 25 31.9	20633	33	8.21		CT94S
A3605-Ax	...	...	20684	34	8.06		CT94S
A3608-A	14 42 26.28	-31 00 13.7	31618	49	9.04		CT95S
A3608-E	14 42 22.46	-31 00 55.7	32474	46	8.37		CT95S
A3612-A	14 55 03.42	-28 03 22.6	28503	39	6.25		CT94S
A3613-D	14 54 54.51	-30 43 02.3	28127	56	6.79		KP96S
A3614-C	14 58 06.40	-30 06 13.4	19674	51	7.21		CT95S
A3615-A	15 02 54.90	-80 33 44.2	20356	47	6.06		CT94S
A3623-D	15 37 40.48	-23 56 12.7	9281	60	...	E	KP96S
A3624-A	16 01 23.98	-83 21 27.7	24381	55	3.71		CT94S
A3624-F	15 57 03.28	-83 29 12.8	24764	61	3.90		CT94S
A3624-G	15 56 52.59	-83 28 52.6	26151	47	5.55		CT94S
A3624-K	15 52 16.65	-83 30 03.3	23244	33	7.47		CT94S
A3626-A	16 21 32.60	-83 47 22.3	20016	39	6.59		CT94S
A3627-1	16 15 03.68	-60 54 27.5	5385	43	6.41		CT93S
A3628-A	16 31 29.74	-75 06 53.0	31642	36	7.03		CT94S
A3630-F	16 40 05.73	-75 59 41.2	31860	48	5.56		CT94S
A3631-A	18 35 57.35	-78 43 59.4	21717	57	5.74		CT95S
A3631-B	18 30 42.83	-78 50 33.6	21766	52	7.22		CT95S
A3631-X	...	...	21312	71	4.83		CT95S
A3644-B	19 46 06.51	-80 02 10.3	38577	66	5.72		CT95F
A3651-A	19 52 08.62	-55 03 46.1	17923	28	11.10		CT94S
A3656-1	20 00 49.97	-38 34 35.9	5975	36	9.07		CT92F CT94S CT94F CT96F
A3667-A	20 12 27.34	-56 49 37.4	16621	51	8.66		CT95S
A3676-A	20 24 24.50	-40 21 59.5	12130	36	8.01		CT92F CT95S
A3677-1	20 26 23.56	-33 21 03.5	13888	41	7.73		CT92F CT95S
A3681-A	20 28 27.73	-33 25 40.9	36022	75	4.65		CT96F CT95S
A3681-C	20 28 30.02	-33 24 42.3	36043	60	5.01		CT95S
A3684-B	20 35 44.36	-78 05 06.7	23344	95	2.23		CT95F
A3684-E	20 35 22.28	-78 05 38.0	23036	62	6.02		CT95F
A3684-X1	...	...	51996	82	3.45		CT95F
A3685-A	20 32 16.19	-56 25 39.9	18632	13	...	E	CT95F

Table 6 — *Continued*

Galaxy ID	R.A. (J2000)	Dec. (J2000)	$v_{helio}$ km s <sup>-1</sup>	$v_{err}$ km s <sup>-1</sup>	Tonry R value	Emission Flag	Observing Run ID
A3687-A	20 33 00.06	-63 01 45.2	22898	47	7.58		CT95F
A3690-A	20 33 45.46	-35 12 59.8	26996	37	9.27		CT96F
A3698-1	20 35 56.21	-25 16 45.3	5845	54	5.96		CT92F KP95F
A3703-A	20 40 01.74	-61 20 01.6	21551	44	8.38		CT96F
A3716-1	20 51 56.82	-52 37 47.9	14046	34	7.67		CT92F
A3728-A	21 05 03.75	-82 43 38.8	29287	54	6.64		CT95F
A3728-B	21 04 57.03	-82 43 52.3	28919	70	5.80		CT95F
A3728-X	...	...	28545	58	6.23		CT95F
A3731-A	21 01 41.95	-38 29 53.8	13860	45	8.72		CT96F
A3733-1	21 01 59.07	-28 03 34.5	11005	45	7.66		CT92F KP95F
A3733-2	21 01 37.58	-28 01 56.2	11794	35	7.30		CT93S CT93S
A3734-C	21 01 50.31	-27 19 52.1	39478	67	5.24		KP95F
A3736-A	21 05 04.49	-43 25 09.2	14577	33	8.55		CT92F
A3741-A	21 11 02.64	-82 08 54.8	23114	54	6.48		CT96F CT95F
A3741-F	21 10 39.70	-82 09 45.7	22869	43	7.03		CT95F
A3742-A	21 07 52.28	-47 10 43.4	4811	38	6.98		CT92F
A3744-1	21 07 16.19	-25 28 08.4	10994	49	7.27		CT95F CT92F
A3744-2	21 07 20.93	-25 29 15.3	12765	41	7.16		CT95F
A3747-1	21 08 38.93	-43 29 11.1	9318	38	7.90		CT92F CT95F
A3747-2	21 08 28.99	-43 29 24.5	5098	29	7.30		CT93S CT92F
A3751-A	21 14 17.42	-42 52 30.1	9271	49	3.52		CT95F
A3751-B	21 14 16.94	-42 53 44.8	28124	98	3.14		CT95F
A3752-A	21 14 13.64	-27 07 47.9	28298	47	8.15		KP95F
A3752-B	21 14 29.80	-27 06 36.8	29202	49	7.50		KP95F
A3753-D	21 14 31.97	-26 46 13.1	21840	57	5.33		KP95F
A3755-A	21 15 29.98	-43 22 17.4	17727	42	8.35		CT95F
A3755-F	21 15 22.16	-43 22 44.2	17875	11	...	E	CT95F
A3756-A	21 16 04.66	-42 42 22.2	16308	40	10.58		CT96F
A3764-A	21 26 17.91	-34 47 06.4	23965	39	8.27		CT96F
A3764-B	21 25 45.53	-34 43 53.7	22166	47	7.77		CT96F
A3771-A	21 29 42.70	-50 49 26.3	22646	45	8.21		CT96F
A3771-B	21 29 46.48	-50 42 20.8	22086	39	8.99		CT96F
A3771-X	...	...	21939	36	10.10		CT96F
A3775-D	21 31 22.54	-43 13 36.2	31661	41	10.42		CT96F
A3782-A	21 35 11.70	-62 04 44.3	16879	36	11.06		CT96F
A3785-A	21 34 17.78	-53 38 13.0	22876	60	7.02		CT96F
A3796-A	21 39 30.10	-51 23 44.6	22693	58	5.83		CT96F
A3799-A	21 43 02.43	-72 39 36.2	13714	54	6.64		CT95F
A3799-E	21 43 25.18	-72 39 50.8	13368	70	4.31		CT95F
A3806-A	21 46 22.79	-57 17 14.6	22356	38	5.97		CT96F
A3806-B	21 47 41.05	-57 18 39.7	22840	52	6.86		CT96F
A3806-Xa	...	...	22488	44	6.85		CT96F
A3806-Xb	...	...	22578	41	8.60		CT96F
A3809-A	21 46 59.16	-43 53 57.2	18642	33	11.76		CT96F
A3809-B	21 47 50.36	-43 53 11.4	19166	45	7.07		CT96F
A3816-A	21 51 30.10	-55 20 14.9	11417	46	7.69		CT96F
A3822-A	21 54 04.33	-57 52 04.0	22615	59	6.16		CT96F
A3822-C	21 55 00.24	-57 39 28.3	23315	51	8.00		CT96F
A3825-A	21 58 26.38	-60 25 34.0	22528	46	7.56		CT96F
A3825-C	21 59 03.44	-60 24 40.5	10663	37	9.12		CT96F
A3826-A	22 00 24.30	-56 10 42.9	22654	48	7.56		CT96F
A3836-A	22 09 21.58	-51 48 27.0	32755	39	7.33		CT94F
A3844-A	22 13 17.70	-34 40 00.6	21897	31	8.67		CT94F
A3849-A	22 15 59.17	-51 34 07.5	31948	53	4.65		CT94F
A3851-A	22 17 00.18	-52 31 38.6	16148	21	13.13		CT94F
A3867-B	22 21 42.67	-57 39 10.5	25100	38	9.35		CT96F
A3869-A	22 20 31.05	-55 07 29.9	11865	43	7.72		CT95F CT92F
A3878-A	22 26 51.53	-31 57 45.0	35642	76	3.39		CT94F
A3878-X	...	...	34837	80	2.77		CT94F
A3879-A	22 27 49.33	-69 01 24.9	19860	26	11.36		CT94F
A3880-A	22 27 54.49	-30 34 34.5	17254	29	9.04		CT94F
A3886-A	22 32 04.08	-54 54 31.3	22012	31	9.34		CT94F
A3891-A	22 37 03.53	-59 53 56.4	25299	37	7.08		CT94F
A3895-A	22 38 31.60	-36 47 14.1	17517	38	9.92		CT96F
A3895-B	22 38 45.76	-36 44 39.7	18018	43	9.56		CT96F
A3897-A	22 39 11.47	-17 20 29.7	22269	53	7.84		KP95F
A3898-A	22 40 10.44	-62 24 54.6	22061	28	8.73		CT94F
A3912-A	22 46 09.88	-36 00 04.5	20168	33	8.97		CT94F
A3915-A	22 48 19.17	-52 03 12.1	29191	52	4.80		CT94F
A3925-B	22 52 30.93	-46 41 46.1	15194	26	9.71		CT96F
A3959-A	23 02 51.94	-33 23 23.1	19691	21	11.92		CT94F
A3969-A	23 05 58.23	-44 10 59.7	37820	42	7.01		CT94F
A3985-A	23 16 15.11	-23 23 36.1	31801	41	10.08		KP95F
A3985-B	23 15 58.31	-23 20 17.2	34218	47	8.11		KP95F
A3987-A	23 16 30.93	-48 12 02.7	36394	44	9.19		CT96F
A3992-A	23 20 28.05	-73 17 17.4	27040	42	8.32		CT96F

**Table 6** — *Continued*

Galaxy ID	R.A. (J2000)	Dec. (J2000)	$v_{helio}$ km s <sup>-1</sup>	$v_{err}$ km s <sup>-1</sup>	Tonry R value	Emission Flag	Observing Run ID
A4008-A	23 30 30.12	-39 16 52.6	16415	22	13.97		CT94F
A4016-A	23 34 34.81	-69 14 28.0	24115	36	8.72		CT96F
A4026-B	23 41 51.37	-37 29 31.9	30647	42	6.32		CT94F
A4029-A	23 43 47.74	-38 14 05.1	30614	45	5.45		CT94F
A4038-1	23 47 44.96	-28 08 31.4	8605	30	8.26		CT93S
A4038-2	23 47 28.30	-28 06 34.6	8212	39	8.44		CT92F CT95F
A4049-1	23 51 36.65	-28 21 55.7	8227	34	7.71		CT92F
A4053-A	23 54 36.09	-27 34 05.1	15005	23	13.60		CT94F
A4059-1	23 57 00.37	-34 45 32.4	14740	39	6.90		CT92F

**Table 7**  
BCG Parameters

Abell	$\alpha$	$M_m$	$M_m(2r_m)$	$M_m(4r_m)$	$\sigma$ km s <sup>-1</sup>	$r_x$ kpc	Ref
0014	0.983	-22.872	-23.564	-24.069	219 ± 15	73	R
0027	0.289	-22.298	...	...	...	...	...
0071	0.397	-22.517	-22.740	...	262 ± 14	...	...
0074	0.447	-22.927	-23.223	-23.461	315 ± 6	...	...
0075	0.455	-22.728	...	...	295 ± 12	...	...
0076	0.552	-22.932	-23.329	...	287 ± 2	467	R
0077	0.789	-23.049	-23.589	-23.982	278 ± 13	...	...
0085	1.039	-23.233	-23.848	-24.193	329 ± 17	1	C
0086	0.676	-23.209	-23.648	-23.944	274 ± 15	215	R
0102	0.539	-23.051	-23.435	-23.717	271 ± 11	...	...
0114	0.520	-23.076	-23.427	-23.702	299 ± 13	...	...
0116	0.470	-22.948	-23.236	-23.447	327 ± 11	76	R
0117	0.670	-23.224	-23.659	-23.963	323 ± 11	177	R
0119	0.767	-23.046	-23.578	-23.909	283 ± 13	23	C
0133	0.775	-22.987	-23.507	-23.888	273 ± 13	5	C
0134	0.357	-22.486	-22.708	...	188 ± 24	1023	R
0147	0.425	-22.819	-23.087	...	289 ± 3	450	R
0150	0.678	-22.921	-23.385	-23.743	258 ± 18	34	R
0151	0.712	-23.138	-23.624	-24.035	308 ± 12	49	R
0152	0.796	-22.719	-23.266	-23.659	239 ± 15	...	...
0154	0.601	-23.225	-23.644	-24.018	314 ± 12	95	R
0158	0.656	-22.705	-23.115	...	262 ± 16	...	...
0161	0.622	-22.596	-23.034	-23.463	228 ± 17	...	...
0168	0.571	-22.848	-23.226	...	253 ± 1	286	R
0171	0.561	-23.192	-23.569	-23.874	337 ± 10	...	...
0174	0.596	-22.622	-23.022	...	290 ± 15	...	...
0179	0.420	-22.420	-22.694	...	269 ± 14	...	...
0189	0.322	-22.109	...	...	212 ± 10	...	...
0193	0.690	-22.944	-23.448	...	462 ± 39	1	C
0194	0.587	-22.611	-22.981	...	262 ± 6	57	R
0195	0.410	-22.706	-22.985	...	275 ± 3	...	...
0208	0.625	-22.989	-23.439	-23.811	319 ± 9	...	...
0225	0.708	-22.965	-23.439	-23.796	271 ± 12	...	...
0240	0.805	-22.788	-23.306	...	240 ± 20	...	...
0245	0.427	-22.401	-22.628	...	202 ± 28	...	...
0246	0.525	-22.556	-22.900	...	316 ± 16	37	R
0257	0.571	-22.816	-23.164	...	257 ± 18	...	...
0260	0.574	-22.973	-23.388	...	298 ± 10	...	...
0261	0.564	-22.897	-23.283	...	246 ± 17	...	...
0262	0.734	-22.383	-22.856	...	232 ± 7	2	C
0267	0.732	-22.326	-22.827	...	206 ± 22	576	C
0268	0.424	-22.087	-22.365	...	192 ± 26	...	...
0279	0.718	-23.162	-23.662	-24.080	268 ± 12	206	R
0292	0.802	-23.074	-23.589	-23.971	289 ± 16	...	...
0295	0.539	-22.789	-23.185	...	258 ± 12	...	...
0311	0.742	-23.213	-23.726	-24.149	248 ± 19	...	...
0326	0.353	-22.183	-22.465	...	336 ± 0	...	...
0347	0.577	-22.524	-22.935	...	269 ± 16	...	...
0357	0.291	-22.060	...	...	225 ± 19	...	...
0358	0.669	-22.894	-23.317	-23.636	260 ± 14	96	R
0376	0.682	-22.861	-23.326	-23.686	265 ± 22	75	R
0386	0.335	-22.555	-22.738	...	276 ± 9	...	...
0397	0.552	-22.882	-23.286	-23.572	314 ± 3	...	...
0399	0.962	-23.236	-23.863	-24.378	242 ± 24	26	C
0400	0.677	-22.335	-22.899	...	...	5	C
0401	0.929	-23.344	-23.985	-24.490	336 ± 18	62	C
0404	0.539	-22.845	-23.192	...	264 ± 14	...	...
0407	0.778	-22.819	-23.406	-23.898	...	...	...
0415	0.851	-22.952	-23.562	-24.040	253 ± 21	62	R
0423	0.609	-22.792	-23.203	-23.511	294 ± 11	...	...
0428	0.286	-22.325	-22.481	...	230 ± 17	...	...
0436	0.622	-22.958	-23.388	-23.714	326 ± 15	...	...
0450	0.405	-22.638	-22.899	...	301 ± 11	...	...
0496	0.766	-23.198	-23.730	-24.152	290 ± 4	3	C
0498	0.620	-23.300	-23.724	-24.019	278 ± 23	...	...
0500	0.610	-23.114	-23.556	-23.957	365 ± 10	36	R
0505	0.735	-23.609	-24.108	...	383 ± 14	...	...
0514	0.517	-23.137	-23.461	-23.671	358 ± 10	1060	R
0533	0.487	-22.855	-23.177	-23.590	282 ± 6	...	...
0539	0.457	-22.800	-23.153	...	282 ± 8	281	C
0548	0.474	-22.936	-23.256	-23.630	222 ± 18	542	R
0564	0.338	-22.709	...	...	182 ± 16	...	...
0568	0.557	-23.200	-23.613	...	299 ± 35	...	...
0569	0.473	-22.708	-23.003	...	245 ± 3	...	...
0576	0.298	-22.477	-22.619	...	278 ± 17	387	C

Table 7 — *Continued*

Abell	$\alpha$	$M_m$	$M_m(2r_m)$	$M_m(4r_m)$	$\sigma$ km s <sup>-1</sup>	$r_x$ kpc	Ref
0582	0.484	-22.819	-23.163	...	288 ± 15	...	...
0592	0.461	-22.948	-23.231	...	342 ± 10	...	...
0595	0.402	-22.789	-23.032	...	258 ± 20	816	R
0600	0.648	-22.725	-23.126	-23.497	191 ± 24	...	...
0602	0.282	-22.385	-22.548	...	...	1134	R
0634	0.485	-22.603	-22.928	...	251 ± 9	...	...
0644	0.796	-22.954	-23.549	-24.012	262 ± 15	11	C
0671	0.710	-23.306	-23.821	-24.232	...	111	R
0690	0.633	-23.427	-23.882	-24.260	...	...	...
0695	0.596	-23.048	-23.412	...	363 ± 14	...	...
0744	0.662	-23.034	-23.473	-23.813	...	2	C
0754	0.748	-23.358	-23.879	...	...	750	C
0757	0.428	-22.423	-22.727	...	250 ± 9	...	...
0779	0.593	-23.255	-23.685	...	327 ± 8	26	R
0780	0.794	-23.026	-23.532	-23.881	266 ± 7	20	R
0819	0.586	-23.146	-23.543	-23.791	...	...	...
0834	0.696	-22.768	-23.239	...	254 ± 24	...	...
0838	0.596	-22.638	-23.059	...	226 ± 6	...	...
0841	0.606	-23.114	-23.548	-23.897	273 ± 10	...	...
0912	0.440	-22.390	-22.663	-23.006	207 ± 15	...	...
0957	0.759	-23.297	-23.840	-24.287	332 ± 0	169	R
0970	0.559	-22.388	-22.830	...	...	120	R
0978	0.615	-23.135	-23.594	-23.965	248 ± 4	23	R
0979	0.605	-22.869	-23.271	-23.561	284 ± 5	...	...
0993	0.552	-23.221	-23.570	-23.800	294 ± 15	25	R
0999	0.441	-22.689	-23.017	...	241 ± 31	...	...
1003	0.644	-22.748	-23.169	...	324 ± 10	...	...
1016	0.433	-22.497	-22.799	...	255 ± 2	...	...
1020	0.448	-22.924	-23.231	...	302 ± 7	481	R
1032	0.391	-22.768	-23.007	...	269 ± 16	543	R
1035	0.600	-23.154	-23.542	-23.824	...	128	R
1060	0.846	-22.764	-23.346	...	208 ± 12	0	C
1066	0.568	-22.823	-23.244	-23.563	308 ± 6	...	...
1069	0.757	-23.130	-23.696	-24.050	...	110	R
1090	0.518	-22.706	-23.078	...	...	...	...
1100	0.562	-22.803	-23.184	...	246 ± 32	...	...
1139	0.583	-22.744	-23.162	...	263 ± 20	197	R
1142	0.543	-22.768	-23.189	...	297 ± 7	52	R
1145	0.364	-22.254	-22.478	...	...	...	...
1149	0.609	-22.961	-23.346	...	283 ± 12	...	...
1155	0.504	-22.664	-23.016	...	...	...	...
1169	0.407	-22.437	-22.717	...	269 ± 23	143	R
1171	0.307	-22.636	-22.814	...	258 ± 15	578	R
1177	0.726	-22.888	-23.391	-23.826	231 ± 13	...	...
1185	0.621	-22.882	-23.270	...	...	161	R
1186	0.522	-22.306	-22.672	...	...	...	...
1187	0.599	-23.077	-23.479	-23.764	...	428	R
1190	0.802	-22.935	-23.488	-23.875	230 ± 23	...	...
1203	0.582	-23.078	-23.485	-23.800	280 ± 15	...	...
1213	0.516	-22.884	-23.185	...	281 ± 19	...	...
1216	0.452	-22.633	-22.921	...	...	...	...
1228	0.428	-22.490	-22.784	...	...	183	R
1238	0.703	-22.819	-23.332	-23.799	...	130	R
1257	0.248	-22.233	...	...	260 ± 8	...	...
1267	0.334	-22.546	-22.747	...	257 ± 7	...	...
1279	0.542	-22.636	-22.997	...	236 ± 3	...	...
1291	0.378	-22.549	-22.752	...	...	298	R
1308	0.550	-23.207	-23.613	-23.918	282 ± 12	...	...
1314	0.544	-22.888	-23.315	-23.718	291 ± 23	71	R
1317	0.645	-23.036	-23.547	-24.050	313 ± 13	87	R
1318	0.477	-22.860	-23.169	...	293 ± 12	1458	R
1334	0.419	-22.701	-22.980	...	265 ± 4	...	...
1344	0.672	-23.190	-23.645	-24.041	302 ± 0	...	...
1365	0.443	-22.812	-23.107	...	283 ± 11	91	R
1367	0.547	-23.036	-23.384	...	308 ± 3	354	R
1371	0.611	-22.827	-23.250	-23.663	260 ± 16	198	R
1375	0.517	-23.344	-23.666	-23.850	296 ± 5	...	...
1377	0.466	-22.759	-23.083	-23.339	294 ± 11	140	R
1383	0.377	-22.560	-22.785	...	...	947	R
1400	0.715	-22.536	-22.981	...	...	190	R
1404	0.463	-22.721	-23.015	-23.267	232 ± 5	...	...
1424	0.565	-23.259	-23.631	...	313 ± 4	168	R
1436	0.329	-22.638	-22.837	...	302 ± 12	968	R
1452	0.501	-22.901	-23.232	...	327 ± 12	...	...
1461	0.470	-22.580	-22.869	...	250 ± 22	...	...
1474	0.530	-22.347	-22.675	...	...	...	...

Table 7 — *Continued*

Abell	$\alpha$	$M_m$	$M_m(2r_m)$	$M_m(4r_m)$	$\sigma$ km s <sup>-1</sup>	$r_x$ kpc	Ref
1507	0.640	-22.887	-23.305	...	...	139	R
1520	0.704	-23.405	-23.899	-24.332	290 ± 13	...	...
1534	0.569	-23.095	-23.489	-23.801	299 ± 7	157	R
1569	0.719	-23.318	-23.776	-24.088	314 ± 12	5	C
1589	0.660	-23.430	-23.888	-24.293	...	...	...
1610	0.476	-23.242	-23.574	-23.807	...	...	...
1630	0.617	-23.058	-23.469	-23.799	316 ± 11	157	R
1631	0.665	-23.083	-23.519	-23.884	254 ± 23	...	...
1644	1.003	-23.184	-23.847	-24.336	212 ± 34	2	C
1648	0.483	-23.004	-23.402	-23.713	296 ± 8	...	...
1656	0.597	-23.417	-23.823	...	386 ± 2	256	R
1691	0.799	-23.236	-23.752	-24.132	257 ± 3	45	R
1709	0.536	-23.032	-23.364	-23.683	283 ± 5	...	...
1736	0.591	-23.503	-23.897	-24.248	303 ± 11	687	C
1741	0.417	-22.784	-23.066	...	265 ± 14	...	...
1749	0.557	-23.168	-23.569	-23.894	302 ± 7	28	R
1767	0.790	-23.216	-23.768	-24.149	...	25	R
1773	0.585	-22.972	-23.391	-23.834	383 ± 21	72	R
1775	0.715	-23.208	-23.706	-24.080	285 ± 20	48	R
1780	0.469	-22.913	-23.210	-23.257	259 ± 12	461	R
1795	0.783	-22.984	-23.556	-24.030	...	12	C
1800	0.940	-23.315	-23.924	-24.350	324 ± 17	83	R
1809	0.610	-23.432	-23.864	-24.265	...	47	R
1825	0.565	-22.848	-23.238	-23.530	...	...	...
1827	0.463	-22.917	-23.205	...	300 ± 11	...	...
1828	0.342	-22.628	-22.845	...	...	...	...
1831	0.792	-23.337	-23.886	-24.318	331 ± 12	51	R
1836	0.603	-23.160	-23.539	-23.811	286 ± 16	...	...
1873	0.451	-22.287	-22.599	...	317 ± 13	79	R
1890	0.674	-23.382	-23.838	-24.164	335 ± 4	236	R
1898	0.623	-22.820	-23.245	-23.564	...	1155	R
1899	0.481	-22.698	-22.986	-23.168	262 ± 13	...	...
1904	0.682	-23.262	-23.729	-24.069	...	289	R
1913	0.459	-22.928	-23.223	...	248 ± 15	896	R
1964	0.560	-22.788	-23.225	-23.647	313 ± 12	...	...
1982	0.644	-22.823	-23.249	-23.541	...	...	...
1983	0.367	-22.736	-22.953	...	304 ± 6	653	R
1991	0.822	-22.967	-23.537	-23.937	269 ± 5	11	C
2022	0.644	-23.035	-23.504	-23.934	...	61	R
2028	0.655	-23.221	-23.663	-24.028	...	...	...
2029	0.935	-23.731	-24.385	-24.924	386 ± 2	1	C
2040	0.678	-22.542	-23.113	-23.556	246 ± 15	39	R
2052	0.855	-22.946	-23.534	-23.991	203 ± 20	0	C
2061	0.554	-23.383	-23.775	-24.147	...	176	R
2063	0.776	-22.753	-23.248	-23.576	198 ± 19	11	C
2065	0.623	-22.737	-23.149	...	265 ± 1	105	C
2067	0.759	-22.552	-23.059	...	...	40	R
2079	0.775	-23.247	-23.807	-24.410	289 ± 6	158	R
2089	0.582	-23.173	-23.584	-23.943	330 ± 7	...	...
2092	0.631	-22.380	-22.833	...	...	132	R
2107	0.741	-23.231	-23.736	-24.117	308 ± 12	1	C
2147	0.694	-22.850	-23.303	-23.734	280 ± 10	0	C
2151	0.750	-22.813	-23.318	-23.634	299 ± 5	1	C
2152	0.412	-22.786	-23.037	-23.154	282 ± 10	63	R
2162	0.493	-22.996	-23.349	...	303 ± 17	49	R
2184	0.353	-22.253	-22.457	...	247 ± 8	...	...
2197	0.574	-23.356	-23.742	-24.034	276 ± 2	886	R
2198	0.292	-22.002	-22.136	...	209 ± 20	...	...
2199	0.760	-23.135	-23.646	-24.053	297 ± 5	1	C
2241	0.574	-22.495	-22.838	...	...	...	...
2247	0.367	-22.590	-22.819	...	257 ± 14	...	...
2248	0.469	-22.747	-23.054	...	...	424	R
2250	0.544	-22.699	-23.121	-23.560	297 ± 15	...	...
2256	0.737	-23.205	-23.675	-24.000	...	143	C
2271	0.783	-23.042	-23.576	-23.942	289 ± 14	17	R
2293	0.510	-22.722	-23.070	...	222 ± 17	...	...
2308	0.657	-22.962	-23.390	-23.693	269 ± 15	...	...
2309	0.571	-22.817	-23.203	...	298 ± 13	...	...
2325	0.517	-22.760	-23.055	...	253 ± 10	...	...
2331	0.810	-22.803	-23.349	-23.798	253 ± 16	246	R
2361	0.368	-22.836	-23.088	...	...	...	...
2362	0.480	-23.090	-23.416	...	307 ± 12	...	...
2366	0.554	-23.095	-23.501	...	279 ± 10	175	R
2370	0.257	-21.729	...	...	240 ± 22	...	...
2372	0.497	-22.920	-23.245	-23.508	267 ± 13	...	...
2382	0.794	-22.854	-23.402	...	243 ± 13	93	R

Table 7 — *Continued*

Abell	$\alpha$	$M_m$	$M_m(2r_m)$	$M_m(4r_m)$	$\sigma$ km s <sup>-1</sup>	$r_x$ kpc	Ref
2383	0.271	-22.081	-22.257	...	...	...	...
2388	0.581	-22.515	-22.910	...	215 ± 27	...	...
2399	0.516	-22.832	-23.154	...	276 ± 19	193	R
2401	0.574	-23.079	-23.457	...	304 ± 12	58	R
2405	0.330	-22.416	-22.645	...	254 ± 11	...	...
2412	0.422	-22.730	-23.111	...	269 ± 13	314	R
2415	0.543	-22.934	-23.277	-23.578	283 ± 9	600	R
2457	0.617	-23.226	-23.641	-23.977	327 ± 14	21	R
2459	0.397	-22.817	-23.051	...	276 ± 13	...	...
2462	0.567	-23.133	-23.556	-23.932	349 ± 9	1	C
2469	0.428	-22.436	-22.669	...	221 ± 20	...	...
2480	0.472	-23.176	-23.488	-23.752	305 ± 13	...	...
2492	0.569	-22.891	-23.267	...	287 ± 11	125	R
2495	0.920	-22.833	-23.510	-24.054	258 ± 15	...	...
2511	0.377	-22.499	-22.723	...	258 ± 19	...	...
2524	0.595	-23.103	-23.489	-23.823	...	...	...
2525	0.535	-22.579	-22.945	...	301 ± 11	...	...
2558	0.546	-22.554	-22.942	...	270 ± 14	...	...
2559	0.801	-23.070	-23.603	-23.984	276 ± 16	...	...
2572	0.540	-22.785	-23.238	...	323 ± 8	57	R
2589	0.755	-22.886	-23.403	-23.828	289 ± 9	3	C
2593	0.795	-22.828	-23.315	...	248 ± 7	10	R
2618	0.648	-23.330	-23.772	-24.137	304 ± 11	...	...
2622	0.640	-22.956	-23.369	-23.624	295 ± 16	55	R
2625	0.452	-22.963	-23.263	...	269 ± 15	2065	R
2626	0.856	-22.971	-23.501	-23.784	278 ± 18	2	C
2630	0.489	-22.965	-23.260	...	273 ± 20	...	...
2634	0.627	-23.097	-23.553	-23.869	366 ± 8	24	R
2637	0.494	-23.199	-23.512	-23.768	285 ± 15	177	R
2644	0.500	-22.756	-23.070	-23.283	303 ± 12	78	R
2656	0.772	-22.861	-23.344	-23.627	286 ± 12	...	...
2657	0.336	-22.408	-22.605	...	206 ± 16	376	C
2660	0.553	-22.649	-23.021	...	225 ± 17	154	R
2665	0.804	-23.137	-23.669	-24.100	285 ± 24	...	...
2666	0.547	-23.054	-23.389	-23.726	292 ± 8	65	R
2670	0.686	-23.342	-23.848	-24.250	299 ± 7	68	R
2675	0.572	-22.889	-23.263	-23.555	256 ± 22	176	R
2678	0.487	-22.682	-22.982	...	285 ± 18	...	...
2716	0.323	-22.786	-22.995	-23.158	451 ± 10	...	...
2717	0.908	-22.667	-23.344	-23.886	235 ± 10	16	C
2731	0.510	-22.790	-23.151	...	291 ± 6	...	...
2734	0.864	-22.893	-23.454	-23.884	236 ± 15	44	R
2764	0.528	-23.223	-23.558	-23.779	357 ± 6	...	...
2771	0.563	-22.862	-23.261	-23.652	263 ± 5	...	...
2793	0.304	-22.210	...	...	301 ± 10	...	...
2799	0.533	-22.619	-22.930	-23.060	271 ± 13	...	...
2800	0.503	-22.954	...	...	271 ± 10	...	...
2806	0.351	-22.664	-22.885	...	285 ± 9	...	...
2810	0.451	-22.553	-22.845	-22.998	265 ± 12	...	...
2819	0.297	-22.930	-23.142	...	274 ± 7	...	...
2824	0.437	-22.638	-22.895	...	250 ± 13	...	...
2836	0.325	-22.409	-22.596	...	...	...	...
2841	0.554	-22.952	-23.333	...	265 ± 10	...	...
2854	0.659	-22.402	-22.879	...	256 ± 10	...	...
2859	0.486	-22.657	...	...	283 ± 6	...	...
2864	0.488	-22.325	-22.645	-22.920	240 ± 6	...	...
2870	0.590	-22.736	-23.129	-23.396	292 ± 16	...	...
2877	0.594	-23.518	-23.939	...	360 ± 46	69	R
2881	0.390	-22.292	-22.530	...	223 ± 3	...	...
2896	0.353	-22.548	...	...	238 ± 7	...	...
2923	0.533	-23.048	-23.352	-23.542	274 ± 5	...	...
2954	0.163	-21.906	-22.030	...	...	...	...
2992	0.340	-22.569	-22.799	-23.046	257 ± 7	...	...
3004	0.521	-22.728	-23.073	...	223 ± 8	...	...
3009	0.712	-23.151	-23.608	-23.892	249 ± 13	...	...
3027	0.622	-22.752	-23.191	-23.561	237 ± 6	...	...
3045	0.463	-22.807	-23.132	...	258 ± 9	...	...
3074	0.732	-23.134	-23.612	...	275 ± 6	...	...
3078	0.697	-23.015	-23.460	-23.756	251 ± 13	...	...
3089	0.524	-22.563	-22.843	...	227 ± 7	...	...
3094	0.571	-22.914	-23.258	-23.452	266 ± 11	...	...
3095	0.405	-22.900	-23.139	...	303 ± 6	...	...
3098	0.704	-22.837	-23.314	-23.692	249 ± 17	...	...
3100	0.533	-22.485	-22.833	-23.093	208 ± 13	...	...
3104	0.692	-22.887	-23.420	-23.807	305 ± 10	18	R
3106	0.778	-22.780	-23.364	-23.859	242 ± 5	...	...

Table 7 — *Continued*

Abell	$\alpha$	$M_m$	$M_m(2r_m)$	$M_m(4r_m)$	$\sigma$ km s <sup>-1</sup>	$r_x$ kpc	Ref
3107	0.498	-22.232	-22.619	...	240 ± 14	...	...
3109	0.601	-23.083	-23.472	-23.709	263 ± 10	...	...
3110	0.537	-23.424	-23.761	-23.960	324 ± 9	...	...
3111	0.717	-23.063	-23.562	-23.948	311 ± 13	...	...
3112	0.798	-23.161	-23.718	-24.157	299 ± 12	0	C
3120	0.744	-22.797	-23.312	-23.704	270 ± 7	...	...
3122	0.553	-23.024	-23.396	-23.720	298 ± 5	...	...
3123	0.443	-22.800	-23.092	...	345 ± 5	...	...
3125	0.433	-22.651	-22.905	-23.085	221 ± 4	...	...
3128	0.578	-23.121	-23.507	-23.766	269 ± 5	404	R
3133	0.478	-21.887	-22.186	-22.446	210 ± 13	...	...
3135	0.449	-22.822	-23.092	-23.244	283 ± 5	...	...
3142	0.576	-22.821	-23.234	...	241 ± 6	...	...
3144	0.433	-22.496	-22.806	-23.070	263 ± 8	...	...
3151	0.709	-22.425	-22.897	...	288 ± 18	...	...
3158	0.622	-23.096	-23.512	-23.849	301 ± 5	458	C
3164	0.513	-23.108	-23.452	-23.726	306 ± 5	448	R
3188	0.257	-21.462	...	...	217 ± 8	...	...
3193	0.467	-22.698	-23.009	...	278 ± 9	...	...
3195	0.585	-22.833	-23.167	...	261 ± 14	...	...
3202	0.352	-22.151	...	...	246 ± 5	...	...
3223	0.478	-23.143	-23.474	-23.714	333 ± 11	...	...
3225	0.617	-22.518	-22.948	-23.361	218 ± 5	...	...
3231	0.452	-22.166	-22.427	...	188 ± 6	...	...
3266	0.845	-23.329	-23.957	-24.504	257 ± 11	2	C
3301	0.706	-23.271	-23.748	-24.180	270 ± 10	...	...
3323	0.845	-22.435	-23.057	-23.471	244 ± 8	...	...
3332	0.476	-22.971	-23.295	-23.584	334 ± 12	...	...
3336	0.711	-22.975	-23.480	-23.894	261 ± 13	...	...
3341	0.657	-22.585	-23.042	-23.395	258 ± 10	12	R
3354	0.440	-22.746	-23.036	-23.258	...	...	...
3367	0.375	-22.393	-22.654	...	222 ± 12	...	...
3374	0.272	-22.593	-22.655	...	240 ± 35	...	...
3376	0.622	-23.037	-23.466	-23.871	319 ± 9	995	C
3380	0.526	-22.781	-23.167	-23.563	244 ± 5	...	...
3381	0.584	-22.399	-22.817	...	240 ± 7	...	...
3389	0.520	-23.084	-23.428	...	270 ± 10	81	R
3390	0.581	-22.530	-22.931	-23.266	264 ± 3	42	R
3391	0.690	-23.424	-23.879	...	320 ± 6	13	C
3392	0.494	-23.215	-23.564	-23.845	264 ± 13	...	...
3395	0.781	-22.946	-23.467	-23.806	287 ± 23	37	C
3407	0.696	-23.223	-23.687	-24.041	270 ± 9	...	...
3408	0.592	-23.363	-23.780	-24.138	297 ± 4	97	R
3420	0.392	-22.730	-22.999	...	260 ± 12	...	...
3429	0.632	-23.033	-23.423	-23.770	260 ± 4	...	...
3432	0.472	-22.869	-23.194	...	260 ± 11	...	...
3490	0.669	-23.267	-23.721	-24.070	307 ± 9	84	R
3492	0.421	-22.765	-23.042	...	...	...	...
3494	0.848	-22.267	-22.821	-23.299	185 ± 26	...	...
3497	0.648	-22.673	-23.107	-23.567	230 ± 9	352	R
3500	0.311	-22.389	-22.582	...	225 ± 11	...	...
3505	0.529	-22.992	-23.381	...	247 ± 13	...	...
3526	0.759	-23.332	-23.814	...	288 ± 11	21	R
3528	0.669	-23.334	-23.818	-24.249	364 ± 10	7	R
3530	0.765	-23.270	-23.849	-24.355	292 ± 14	72	R
3531	0.845	-22.593	-23.144	...	...	...	...
3532	0.724	-23.086	-23.635	-24.184	280 ± 15	128	R
3537	0.527	-23.057	-23.410	-23.769	321 ± 11	...	...
3542	0.279	-22.450	-22.637	...	303 ± 9	...	...
3548	0.385	-22.690	-22.938	...	283 ± 7	...	...
3549	0.491	-22.152	...	...	117 ± 50	...	...
3552	0.571	-22.731	-23.119	...	238 ± 11	...	...
3553	0.444	-22.452	-22.731	...	245 ± 9	...	...
3554	0.725	-22.858	-23.340	-23.732	263 ± 11	...	...
3556	0.598	-23.383	-23.788	...	347 ± 12	624	R
3557	0.529	-22.891	-23.248	-23.556	...	...	...
3558	0.906	-23.451	-24.061	-24.561	282 ± 14	4	C
3559	0.627	-23.327	-23.775	-24.118	313 ± 7	...	...
3560	0.331	-22.488	...	...	234 ± 7	159	R
3562	0.703	-22.995	-23.511	-24.012	263 ± 6	38	C
3563	0.362	-22.527	-22.759	...	248 ± 13	...	...
3564	0.457	-22.826	-23.096	-23.197	276 ± 5	...	...
3565	0.551	-23.224	-23.613	...	883 ± 29	...	...
3570	0.330	-22.678	-22.873	...	284 ± 20	...	...
3571	1.125	-23.280	-24.003	-24.496	313 ± 11	0	C
3572	0.353	-22.712	-22.932	...	239 ± 2	...	...



Table 7 — *Continued*

Abell	$\alpha$	$M_m$	$M_m(2r_m)$	$M_m(4r_m)$	$\sigma$ km s <sup>-1</sup>	$r_x$ kpc	Ref
3574	0.743	-23.064	-23.588	...	239 ± 11	...	...
3575	0.280	-21.949	-22.168	...	283 ± 14	...	...
3577	0.542	-22.552	...	...	297 ± 5	...	...
3581	0.638	-22.642	-23.073	-23.588	283 ± 3	1	C
3599	0.160	-21.329	...	...	223 ± 5	...	...
3603	0.494	-22.996	-23.326	...	...	...	...
3605	0.675	-22.933	-23.390	-23.795	276 ± 12	...	...
3615	0.579	-23.236	-23.647	...	279 ± 20	...	...
3651	0.730	-23.302	-23.757	-24.049	284 ± 15	...	...
3656	0.574	-23.001	-23.444	-23.948	296 ± 3	...	...
3667	0.768	-23.320	-23.843	-24.261	327 ± 13	137	C
3676	0.468	-22.872	-23.164	...	218 ± 29	...	...
3677	0.421	-22.135	-22.462	...	223 ± 16	...	...
3684	0.496	-22.483	-22.819	...	294 ± 13	...	...
3685	0.068	-21.200	...	...	96 ± 25	...	...
3687	0.672	-22.959	-23.403	-23.727	251 ± 9	...	...
3698	0.366	-22.298	...	...	285 ± 4	...	...
3703	0.610	-22.942	-23.396	-23.771	234 ± 7	...	...
3716	0.719	-22.988	-23.483	-23.842	275 ± 10	271	R
3731	0.497	-22.950	-23.296	...	276 ± 5	...	...
3733	0.632	-22.561	-23.017	...	314 ± 12	182	R
3736	0.679	-23.301	-23.752	-24.081	282 ± 9	...	...
3741	0.670	-22.857	-23.322	-23.723	229 ± 5	...	...
3742	0.415	-22.376	-22.642	...	287 ± 8	...	...
3744	0.442	-22.901	-23.190	...	287 ± 8	...	...
3747	0.436	-22.631	-22.916	...	254 ± 12	...	...
3753	0.169	-21.916	...	...	141 ± 37	...	...
3764	0.463	-22.861	-23.197	...	215 ± 6	...	...
3771	0.612	-22.853	-23.240	-23.573	237 ± 5	...	...
3781	0.501	-21.893	-22.182	...	...	...	...
3782	0.619	-23.088	-23.506	-23.854	259 ± 5	...	...
3785	0.541	-23.335	-23.704	-23.994	366 ± 6	...	...
3796	0.610	-22.770	-23.214	-23.613	230 ± 7	...	...
3799	0.471	-22.211	-22.553	-22.855	268 ± 6	...	...
3806	0.772	-23.346	-23.848	-24.260	277 ± 0	51	R
3809	0.720	-22.822	-23.319	-23.721	246 ± 6	116	R
3816	0.544	-22.622	-23.009	-23.353	258 ± 5	...	...
3822	0.628	-23.052	-23.455	-23.777	328 ± 6	...	...
3825	0.448	-22.916	-23.216	-23.477	...	1064	R
3826	0.712	-23.313	-23.758	-24.093	272 ± 6	...	...
3844	0.366	-21.851	-22.157	...	215 ± 17	...	...
3851	0.508	-22.815	-23.163	-23.471	239 ± 10	...	...
3869	0.379	-22.736	-22.981	...	284 ± 13	...	...
3879	0.484	-22.624	-22.931	-23.169	228 ± 14	...	...
3880	0.751	-22.936	-23.403	-23.716	251 ± 13	31	R
3895	0.393	-22.798	-23.024	...	295 ± 4	...	...
3897	0.567	-23.127	-23.555	-23.924	341 ± 13	...	...
3898	0.410	-22.011	...	...	212 ± 14	...	...
3912	0.678	-22.807	-23.217	-23.513	245 ± 19	...	...
3925	0.554	-23.144	-23.560	-23.914	...	...	...
4008	0.591	-22.993	-23.366	-23.694	270 ± 11	...	...
4038	0.449	-22.706	-22.993	...	274 ± 8	137	C
4049	0.512	-22.848	-23.239	...	272 ± 9	...	...
4059	0.891	-23.246	-23.841	-24.287	289 ± 8	8	C

**Note.** — Columns: (1) Abell cluster number, (2)  $\alpha$  at the metric radius, (3) absolute metric luminosity, (4) absolute metric luminosity within  $2r_m$ , (5) absolute metric luminosity within  $4r_m$ , (6) galaxy stellar velocity dispersion, (7) radial offset of the BCG from the X-ray cluster center, (8) X-ray reference, R=ROSAT,C=Chandra. The CMB frame has been adopted for the calculation of metric luminosities.

**Table 8**  
M2 Parameters

Abell	$\alpha$	$M_m$	$\sigma$ km s <sup>-1</sup>	$r_x$ kpc
0027	0.542	-22.229	224 ± 20	...
0071	0.323	-22.340	223 ± 21	...
0074	0.408	-22.669	...	...
0075	0.528	-22.316	...	...
0076	0.397	-22.601	...	313
0086	0.469	-22.864	260 ± 16	235
0102	0.549	-22.580	...	...
0116	0.473	-22.513	...	429
0119	0.479	-22.993	...	139
0134	0.476	-21.550	...	1307
0147	0.570	-22.426	...	44
0154	0.677	-23.026	...	141
0161	0.168	-22.143	...	...
0171	0.410	-22.722	...	...
0174	0.403	-22.497	...	...
0179	0.584	-22.403	...	...
0240	0.338	-22.547	...	...
0246	0.351	-22.306	...	116
0399	0.417	-23.109	...	398
0400	0.181	-22.102	...	4
0428	0.405	-22.251	200 ± 24	...
0436	0.495	-22.331	202 ± 45	...
0500	0.550	-23.049	...	971
0533	0.521	-22.724	...	...
0539	0.791	-22.523	...	2
0568	0.340	-22.488	...	...
0576	0.548	-22.334	...	43
0582	0.324	-22.600	...	...
0592	0.314	-22.829	267 ± 9	...
0595	0.489	-22.647	281 ± 17	360
0602	0.810	-22.300	...	58
0819	0.469	-22.414	...	...
0838	0.409	-22.366	164 ± 10	...
0841	0.570	-22.742	237 ± 11	...
0970	0.307	-22.227	...	81
0978	0.321	-22.307	...	257
0979	0.417	-22.375	...	...
1032	0.356	-22.528	...	645
1066	0.531	-22.695	...	...
1069	0.412	-22.033	...	563
1142	0.664	-22.618	...	139
1145	0.272	-22.110	...	...
1149	0.376	-22.633	...	...
1169	0.320	-22.180	...	163
1171	0.523	-22.448	...	260
1187	0.414	-22.554	...	641
1190	0.551	-22.929	...	...
1203	0.337	-22.283	...	...
1228	0.533	-22.281	...	277
1238	0.404	-22.412	...	...
1317	0.429	-22.424	...	603
1318	0.653	-22.763	235 ± 14	922
1371	0.591	-22.734	...	291
1375	0.642	-23.118	298 ± 6	...
1377	0.565	-22.691	...	738
1383	0.487	-22.450	...	458
1436	0.506	-22.583	238 ± 12	303
1452	0.562	-22.857	...	...
1630	0.491	-22.944	...	718
1644	0.566	-22.802	...	726
1648	0.460	-22.331	256 ± 12	...
1656	0.859	-22.984	...	103
1709	0.571	-22.420	...	...
1736	0.636	-22.850	...	66
1767	0.330	-22.799	...	445
1773	0.298	-22.496	...	536
1775	0.439	-23.089	...	61
1780	0.661	-22.808	313 ± 17	113
1809	0.702	-22.772	...	340
1825	0.504	-22.850	...	...
1827	0.550	-22.310	273 ± 21	...
1890	0.534	-22.598	240 ± 20	306
1898	0.367	-22.730	...	215
1982	0.302	-21.777	...	...
1983	0.786	-22.250	...	64

Table 8 — *Continued*

Abell	$\alpha$	$M_m$	$\sigma$ km s <sup>-1</sup>	$r_x$ kpc
2022	0.298	-21.818	...	254
2028	0.394	-22.359	...	...
2061	0.493	-22.989	...	623
2065	0.803	-22.420	...	8
2079	0.241	-22.557	...	233
2147	0.571	-22.632	...	183
2152	0.382	-22.369	...	109
2197	0.696	-22.791	...	27
2198	0.038	-20.905	...	...
2241	0.362	-22.341	...	...
2247	0.641	-22.460	...	...
2248	0.485	-22.643	...	1493
2250	0.344	-22.694	275 ± 16	...
2256	0.404	-23.143	311 ± 9	2446
2293	0.600	-22.621	282 ± 15	...
2325	0.379	-22.452	206 ± 11	...
2331	0.429	-22.405	...	552
2361	0.435	-22.759	301 ± 12	...
2370	0.167	-21.716	...	...
2372	0.377	-22.320	...	...
2382	0.444	-22.781	...	376
2399	0.408	-22.712	...	309
2412	0.277	-21.764	...	710
2459	0.423	-22.786	...	...
2462	0.281	-21.958	...	149
2492	0.404	-22.112	...	302
2511	0.586	-22.353	...	...
2524	0.594	-22.980	...	...
2525	0.354	-22.515	...	...
2572	0.671	-22.434	...	32
2618	0.659	-23.255	332 ± 11	...
2625	0.525	-22.827	...	1125
2637	0.342	-22.615	312 ± 11	467
2656	0.200	-21.633	...	...
2657	0.890	-22.354	...	1
2678	0.363	-22.641	...	...
2764	0.400	-22.436	...	...
2771	0.353	-22.154	...	...
2793	0.267	-22.059	196 ± 69	...
2799	0.423	-21.934	...	...
2800	0.478	-22.773	...	...
2806	0.627	-22.404	207 ± 12	...
2810	0.422	-22.133	234 ± 13	...
2819	0.430	-22.868	269 ± 8	...
2824	0.371	-22.198	231 ± 20	...
2836	0.439	-22.307	229 ± 13	...
2854	0.361	-22.307	221 ± 20	...
2859	0.355	-22.255	...	...
2864	0.402	-22.129	...	...
2881	0.405	-22.262	...	...
2923	0.307	-22.295	...	...
2954	0.339	-21.274	...	...
3004	0.284	-22.370	...	...
3027	0.543	-22.733	...	...
3074	0.360	-22.575	...	...
3078	0.256	-22.071	...	...
3089	0.531	-22.416	...	...
3094	0.749	-22.423	...	...
3098	0.575	-22.576	235 ± 10	...
3104	0.274	-21.848	...	376
3106	0.509	-22.626	...	...
3107	0.369	-22.054	...	...
3109	0.290	-21.348	...	...
3110	0.468	-22.752	...	...
3120	0.305	-21.472	...	...
3122	0.611	-22.761	274 ± 11	...
3123	0.249	-22.009	...	...
3128	0.541	-22.898	...	1057
3133	0.181	-21.340	...	...
3135	0.510	-22.778	...	...
3151	0.610	-22.304	229 ± 25	...
3158	0.723	-22.987	...	56
3164	0.397	-22.947	...	1109
3223	0.311	-22.561	233 ± 9	...
3341	0.222	-22.352	...	130
3354	0.418	-22.455	...	...

**Table 8** — *Continued*

Abell	$\alpha$	$M_m$	$\sigma$ km s <sup>-1</sup>	$r_x$ kpc
3374	0.376	-22.397	...	...
3389	0.506	-22.909	293 ± 9	814
3391	0.656	-22.818	268 ± 6	80
3408	0.666	-22.849	245 ± 5	222
3420	0.295	-22.167	...	...
3492	0.323	-21.861	...	...
3497	0.296	-22.449	...	400
3505	0.357	-22.767	296 ± 11	...
3531	0.553	-22.645	...	...
3548	0.500	-22.607	...	...
3570	0.633	-22.211	...	...
3577	0.422	-22.417	199 ± 5	...
3603	0.544	-22.162	106 ± 3	...
3605	0.368	-22.711	...	...
3651	0.336	-22.580	...	...
3733	0.506	-22.553	279 ± 20	110
3764	0.340	-22.741	238 ± 6	...
3771	0.373	-22.818	...	...
3785	0.540	-23.281	...	...
3799	0.305	-21.702	161 ± 8	...
3822	0.682	-23.005	286 ± 8	...
3825	0.535	-22.792	249 ± 6	385
3844	0.287	-21.409	...	...
3880	0.247	-22.063	...	63
3895	0.676	-22.578	190 ± 8	...
3912	0.379	-22.325	...	...
3925	0.394	-22.401	...	...
4038	0.719	-22.499	249 ± 9	17

**Note.** — Columns: (1) Abell cluster number, (2)  $\alpha$  at the metric radius, (3) absolute metric luminosity, (4) galaxy stellar velocity dispersion, (5) radial offset of the BCG from the X-ray cluster center. The CMB frame has been adopted for the calculation of metric luminosities.